89

Intramolecular Dynamics of Acetylene

by

Stephani Ann Brandt Solina

B.S., Chemistry (1989)

University of California, Berkeley

Submitted to the Department of Chemistry in Partial Fulfillment of the Requirements for the Degree of

DOCTOR OF PHILOSOPHY

at the

MASSACHUSETTS INSTITUTE OF TECHNOLOGY

June 1996

Signature of Author _____
Department of Chemistry
May 24, 1996

Certified by _____
Robert W. Field
Professor of Chemistry
Thesis Supervisor

Accepted by _____
Dietmar Seyferth
Chairman, Department Committee on Graduate Students

This doctoral thesis has been examined by a Committee of the Department of Chemistry as follows:

Professor Moungi G. Bawendi _____
Chairperson

Professor Robert W. Field _____
Thesis Supervisor

Professor Irwin Oppenheim _____

Intramolecular Dynamics of Acetylene

by

Stephani Ann Brandt Solina

Submitted to the Department of Chemistry on May 24, 1996 in
Partial Fulfillment of the Requirements for the Degree of Doctor
of Philosophy in Chemistry

ABSTRACT

Dispersed Fluorescence spectra of acetylene have been recorded and unzipped, through a fortuitous coincidence of FC active modes and active anharmonic resonances, thereby pictorially revealing the key factors controlling the vibrational dynamics on the acetylene S_0 surface. When energy is placed into very high excitation of the *trans*-bend and moderate excitation of the CC stretch, three approximately conserved quantities survive, *i.e.*, no trace of the expected total breakdown of vibrational constants of motion due to energetic access to the vinylidene isomer is observed for vibrational energies up to at least 16,400 cm^{-1}. Unzipping the DF spectrum reveals the FC intensity profiles for the acetylene $\tilde{A} \rightarrow \tilde{X}$ system with two FC active modes. Also, the unzipped DF spectrum clearly demonstrates that IVR increases within a polyad by increasing *trans*-bend, v_4, and by decreasing CC stretch, v_2. Increasing IVR with increasing v_4 or decreasing v_2, are both cases where the first few resonance tiers play the dominant role in controlling IVR for the initial states prepared in these experiments, very high excitation in the *trans*-bend and moderate excitation in the CC stretch.

Thesis Supervisor:Robert W. Field
Title: Professor of Chemistry

Acknowledgements

I should have written these acknowledgments first, before anything else, when my thoughts were a bit clearer. So I apologize deeply to any whom I have forgotten to mention at this moment. How do I describe my life these past seven years? It was filled with people. People who have become friends, acquaintances and people I will never forget.

Foremost I would like to thank my advisor, Bob Field. I don't have to attest to the caliber of scientist that Bob is, but I do think it is important to mention the qualities that aren't written down on paper already. Bob is a phenomenal speaker, an enthusiastic and gifted teacher (anyone who could get organic chemists to *like* quantum mechanics is got to be special!) and a scientist/advisor who is not only willing to allow his graduate students to pursue subjects not in his field of expertise, but helps them make the contacts that they would need to work in that area. Bob likes dynamics, but it is not his love. The fact that we acetylene "groupies" are successful in our scientific endeavor is a great credit to Bob's approach to advising. By letting me run with my ideas, I learned to think. By introducing me to people I learned to network and build collaborations. By opening opportunities we have taken acetylene in a whole new direction. Many Thanks, Bob.

There are two very special people that I was fortunate to be able to work with.

As for Jon O'Brien — you couldn't ask for a better partner, both experimentally and theoretically it was a true joy to work *with* Jon. You are very lucky if once in your life you find someone with the same passion for the project, the same understanding of the problem and the same level of excellence to strive for, *i.e.* someone you can *trust.* Between "tornado" meals at Hope College and driving to Columbus in RONIN, Jon also became a great friend. I wish you the best of luck, although you will succeed in anything you go into, Jon!

As for Dave Jonas — you couldn't ask for a better teacher. Dave is one of the few people in science that *really* knows what he is doing. I couldn't have found a better mentor: he taught me about science, the way it should be and how to really *understand* concepts; and about acetylene, how to break with tradition and think beyond customary boundaries. I hope one day you get the credit you deserve, Dave!

I was also fortunate to work with George Adamson — thai orchids and much more, buddy.

To Jody Klaassen — thanks for all the Friday afternoon beers, dinners and fun times. I can't wait to come and visit you in Minnesota.

To Jim Lundberg — thanks for the all those discussions about dynamics and acetylene. Just like you said, "Dynamics RULES! To bad no one wants to fund it."

To Steve Coy — thanks for being there at critical moments and for being a presence in group meetings that understood dynamics.

To Kevin Cunningham — thanks for the hugs and an open ear.

To Joe Bentley — thanks for working on the time dependent acetylene stuff with me, buddy. I think we started something very interesting.

The hardest thing about leaving academia was the leaving people in the field of IVR. Special thanks to Mike Davis — for having me out at Argonne, for discovering a really useful technique for spectra and for the many long and enjoyable discussions about dynamics. I hope we continue those in the future. Also thanks to Rick Heller, besides the fun discussions about dynamics, I'm glad we found something that we could work on. To Kazuo Harai — thanks and I wish you well in your future endeavors. Many thanks to Mike Kellman, I've always enjoyed our discussions. I would also like to thank the "Telluride folks": Mike Davis, Mike Kellman, Ned Sibert, Anne McCoy, Fleming Crim, Kevin Lehmann, Bob Wyatt, Joel Bowman, Randy Shirts, Tucker Carrington, Mark Child and Howie Taylor. They really fostered an environment where we could all talk about the subject we loved, and it didn't matter if you were a young graduate student or a full professor.

To Robert Littlejohn — It was so nice to see you again last summer. You're still as amazing as ever. Thanks for the great start in non-linear dynamics as a UROP at Cal.

To Rich Saykally — It's always great to run into you again. Thanks for the excellent class in spectroscopy and for opening doors when I needed them. I'll take you up on the coffee offer next time I'm back home in Berkeley.

To Brad, Curt, John, Rich, Dennis and Dale — Thanks for making Boston a home.

To Gavin, Tom, Steve[3], Scott, Chris, Carlos, Ron, John, Bill, Barbara, Elaine, Anuj, Rich, Bob and Henk — The first thing I say about Stone & Webster, ASDS, Inc., is I like the people. Thanks for making me feel welcome from the very beginning.

And finally, loving thanks to my parents who fostered a perfect environment for a very curious and inquisitive child — thanks for answering all those questions about math, science and medicine.

I dedicate this thesis to the "guys" in my life without whose love, support and presence when I needed them, I would not have finished this Ph.D.: my shhhweetie Patrick Piccione; my cats Fafhrd, Misha and Mouser; and my '84 Vette Ronin.

Contents

Part I

Spectroscopy of Acetylene

Chapter 1

High Resolution Fluorescence Excitation Studies of Acetylene

While performing stimulated emission pumping (SEP) studies [1, 2] or dispersed fluorescence (DF) studies [3,4], several vibrational bands of the $\widetilde{A}$ state were studied at a higher resolution than was previously reported in the literature [5]. The results of the high resolution fluorescence excitation scan will be tabulated and published in a future paper. Presented here is a representative spectroscopic fit of one of the bands studied.

1.1 Experimental Details

A Lambda Physik LPX210icc excimer pumped a Lambda Physik 2002EC (with extracavity etalon removed) dye laser with an intra-cavity etalon, resolution=0.05 cm^{-1}. The output of the dye laser was frequency doubled in β-BBO (CSK crystals) producing tunable UV radiation. The dye laser was pressure scanned with $0 - 1$ atm of SF_6 to produce frequency scans of roughly 30 cm^{-1} length in the UV region. The fundamental and second harmonic laser beams were separated by 60° S1UV fused silica prisms, and a second 60° prism compensated for the first prism in such a way that the second harmonic emerged travelling parallel to its initial direction. This arrangement minimizes beam walk as the laser frequencies were tuned. A small portion of the fundamental was passed through a Te_2 absorption cell for calibration purposes [6]. The doubled laser beam of 90 μJ/pulse entered a static gas cell containing 100 mTorr of acetylene (Matheson purified grade, further purified by several liquid nitrogen freeze, evacuate, and thaw cycles and sublimed into the cell at thermal equilibrium with a pentane slush). As the dye laser was scanned $\widetilde{A} \rightarrow \widetilde{X}$ side fluorescence was imaged by S1UV f/1.9 collection optics onto a photomultiplier (Hamamatsu R166 "solar blind" or Hamamatsu R331). SCHOTT BG1, BG3, BG25, UG1 or UG5 filters were used to eliminate scattered light from the doubled laser beam. The outputs of the photomultiplier was amplified by a LeCroy VV100BTB amplifier, and fed into a Intersil 733 differential video amplifier and an OEI 9911 high current linear voltage follower (50Ω line driver). The output of the line driver was connected to a SRS 250 boxcar which was connected to a National Instruments DT2801 A/D converter in an IBM PC.

1.2 Least Squares Fitting of the V^2K^1 $\widetilde{A}$ State Vibrational Level

Fourteen overlapping pressure scans of the $V_0^2K_0^1$ vibrational band were recorded to measure the rotational levels used in the spectroscopic fits and presented in Table 1.1.

The term values were generated using the known rotational constants of the zero-point level of the $\widetilde{X}$ state [7]. A polynomial least-squares fit [8] was performed separately for the e and f rotational levels, see Table 1.2, producing a phenomenalogical fit to a zero-order term, a vibronic energy (T_0), a first-order term, a rotational energy ($B_vJ(J+1)$), and a second-order term, a centrifugal energy ($-D_vJ(J+1)^2$). A

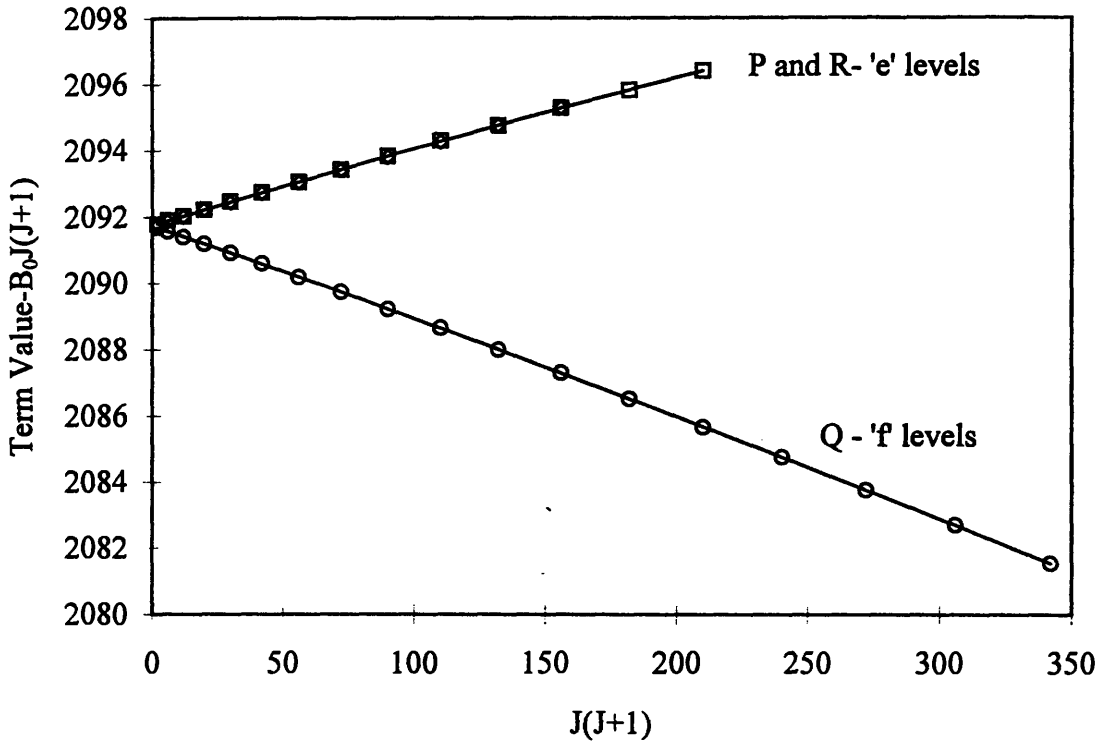

Figure 1.1: A reduced term value plot of the observed levels and the fitted rotational parameters. The f levels are reached through Q branch transitions, while the e levels are reached through both P and R transitions.

	Q Transitions - f levels		P and R Transitions - e levels	
J'	Observed	O-C	Observed	O-C
1	44291.411	0.002	44291.508	-0.007
			44291.511	0.004
2	44295.602	-0.006	44295.913	-0.007
			44295.931	0.011
3	44301.896	-0.010	44302.517	-0.009
			44302.531	0.005
4	44310.306	0.003	44311.335	0.001
			44311.337	0.003
5	44320.802	0.004	44322.341	-0.001
			44322.360	0.018
6	44333.405	0.014	44335.552	0.003
			44335.559	0.009
7	44348.073	-0.006	44350.940	-0.016
			44350.951	-0.005
8	44364.863	0.001	44368.554	-0.004
			44368.564	0.006
9	44383.739	-0.001	44388.336	-0.020
			44388.357	0.001
10	44404.715	0.006	44410.340	-0.007
			44410.361	0.014
11	44427.762	-0.006	44434.537	0.006
			44434.528	-0.002
12	44452.925	0.009	44460.904	0.001
			44460.913	0.010
13	44480.146	-0.005	44489.454	-0.009
14	44509.466	-0.003	44520.206	0.000
15	44540.869	0.000		
16	44574.346	-0.003		
17	44609.905	-0.001		
18	44647.539	0.004		

Table 1.1: Observed term values and the observed minus calculated values for the V^2K^1 rovibrational levels.

	T_0	B_v	D_v
e levels	44289.31(2)	1.1012(4)	$8(2)\text{x}10^{-6}$
f levels	44289.31(2)	1.0499(3)	$7(1)\text{x}10^{-6}$

Table 1.2: Results of polynomial least-squares fit to observed term values for the V^2K^1 rovibrational levels.

phenomenalogical fit is useful for deriving an analytical form of the term values for use when an accurate value of the term energy is needed.

In the future paper phenomenalogical, as well as, effective Hamiltonian fits will be presented for several V and K levels. Effective Hamiltonian fits are to spectroscopic terms that try to shed some light on the form of the potential surface of the $\widetilde{A}$ state. These fits might be useful in further calculations of the $\widetilde{A}$ state potential. Further refinement of the $\widetilde{A}$ state potential will be useful in the future with regards to real calculations of $\widetilde{A} \rightarrow \widetilde{X}$ transition intensities.

References

[1] D. M. Jonas, S. A. B. Solina, B. Rajaram, R. J. Silbey, R. W. Field, K. Yamanouchi, S. Tsuchiya. *J.Chem.Phys.* **97**(4), 2813 (1992).

[2] D. M. Jonas, S. A. B. Solina, B. Rajaram, R. J. Silbey, R. W. Field, K. Yamanouchi, S. Tsuchiya. *J.Chem.Phys.* **99**(10), 7350 (1993).

[3] S. A. B. Solina, J. P. O'Brien, R. W. Field, W. F. Polik. *Ber.Bunsenges.Phys.Chem.* **99**(3), 555 (1995).

[4] S. A. B. Solina, J. P. O'Brien, R. W. Field, W. F. Polik. *J.Phys.Chem.* **100**(19), XXX (1996).

[5] J. K. G. Watson, M. Herman, J. C. Van Craen, R. Colin. *J.Mol.Spectros.* **95**(1), 101 (1982).

[6] J. Cariou, P. Luc. *Atlas du Spectre d'Absorption de la Molecule de Tellure.* Editions du C.N.R.S., Orsay (1979).

[7] J. J. Hillman, D. E. Jennings, G. W. Halsey, S. Nadler, W. E. Blass. *J.Mol.Spectros.* **146**, 389 (1993).

[8] W. H. Press, B. P. Flannery, S. A. Teukolsky, W. T. Vetterling. *Numerical Recipes: The Art of Scientific Computing.* Cambridge University Press, New York, NY (1988).

Chapter 2

Forbidden Transitions in the SEP Spectrum of Acetylene

The *trans*-bent $\widetilde{A}$ state of acetylene has ^1A_u electronic symmetry, and the linear $\widetilde{X}$ state of acetylene has $^1\Sigma_g^+$ electronic symmetry. Thus the transition moment for the $\widetilde{A} \leftrightarrow \widetilde{X}$ electric dipole transition is perpendicular to the plane of the *trans*-bent $\widetilde{A}$ state. This transition moment direction would imply a $\Delta K = K' - \ell = \pm 1$ rotational selection rule if the molecule were a rigid symmetric top with the same principal axis in both electronic states. In addition to the allowed $\Delta K = \pm 1$ transitions, $\Delta K = 0, \pm 2$ and ± 3 transitions have been observed in the stimulated emission pumping (SEP) spectrum of acetylene [1].

For the basis sets used here, a product of anharmonic oscillators for the vibrational part of the wavefunction and rigid rotors for the rotational part of the wavefunctions, $\Delta K \neq \pm 1$ transitions can only occur via asymmetry induced K-mixing, axis-switching transitions or Coriolis perturbations in either or both electronic states.

It will be shown that the asymmetry effects do not contribute significantly at the low-J values probed in the SEP experiments, while the axis-switching mechanism is responsible for the $\Delta K = 0, \pm 2$ transitions, and a second-order Coriolis effect is responsible for the $\Delta K = \pm 3$ transitions.

2.1 Experimental Details

Stimulated Emission Pumping (SEP) is a folded variant of Optical-Optical Double Resonance, See Figure 2.1 The first laser, named the PUMP, populates a single rovibronic level of an excited electronic state. If a second laser, the DUMP, is tuned through resonance with a transition between the level populated by the PUMP and a thermally unpopulated vibrational level of the ground electronic state; the DUMP stimulates emission to that vibrational level, partially depopulating the excited electronic state. This excited state depopulation is detected as a decrease in the total intensity of undispersed side fluorescence. Since surprisingly weak SEP transitions are detected, the experiment is described in detail.

2.1.1 Apparatus

A single Lambda Physik LPX210icc excimer laser pumps two tunable dye lasers. Both the PUMP dye laser, a Lambda Physik 2002EC with extracavity etalon removed, and the DUMP dye laser, a Lambda Physik 3002E, are frequency doubled in β-BBO (CSK crystals) to produce tunable UV radiation. For each dye laser the fundamental and second harmonic are separated by 60° S1UV fused silica prisms, and a second 60° prism compensates for the first prism in such a way that the second harmonic beam emerges travelling parallel to its initial direction. This arrangement minimizes beam walk as the PUMP and/or DUMP laser frequencies are tuned. All beam paths were kept in a single plane to maintain the relative parallelism

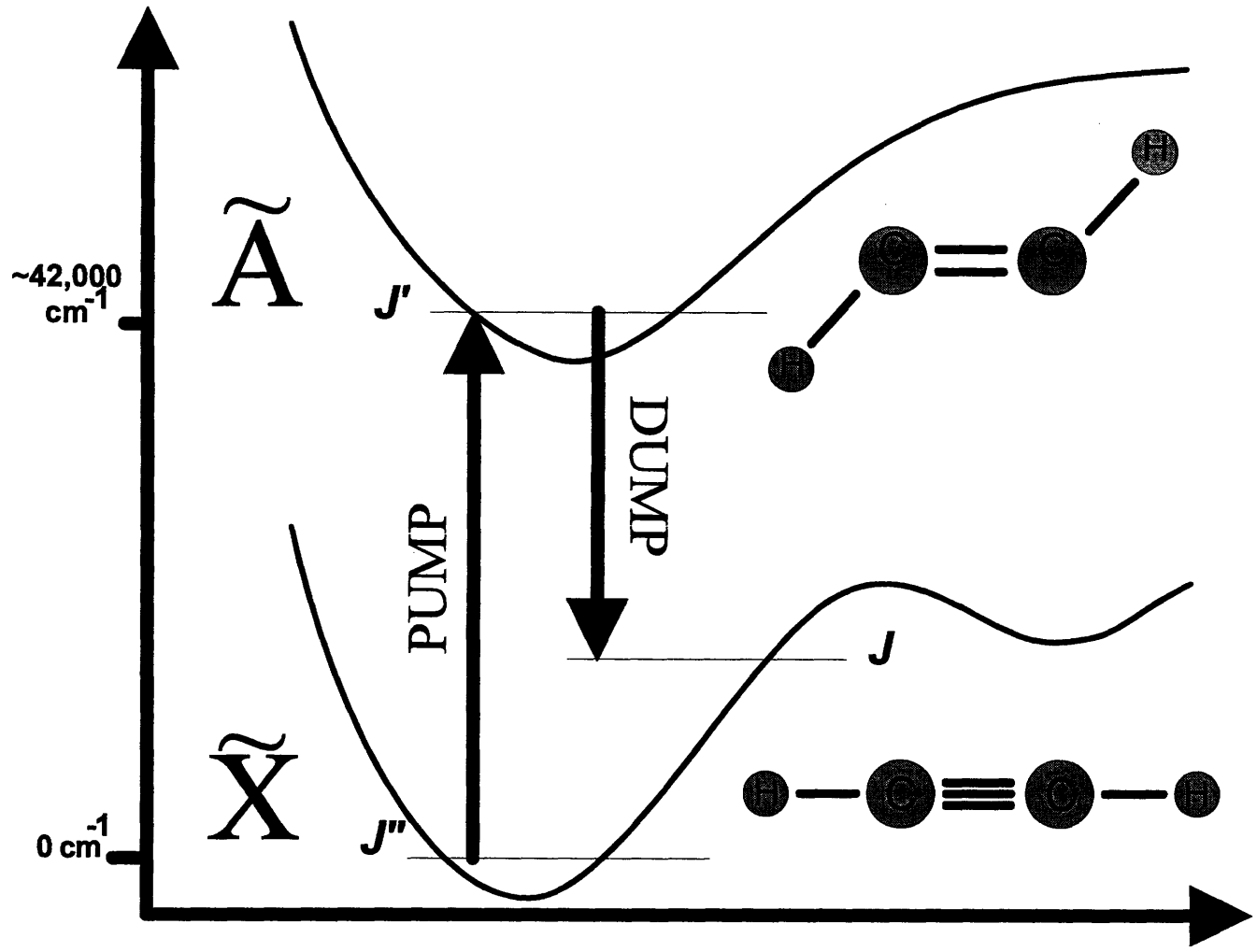

Figure 2.1: Stimulated emission pumping (SEP) is a folded variant of optical-optical double resonance. Molecules are first "pumped" up to an excited electronic state with one laser, then stimulated or "dumped" back down to the ground electronic state via a second laser. The quantum numbers for the initial, intermediate and final states will be denoted with primes, J'', J' and J, respectively, as shown in this figure.

of the linear PUMP and DUMP polarizations. The doubled PUMP laser beam is split by a 222nm 50% beamsplitter, so that about 90 μJ of light enters each identical signal and reference cells containing 200 mTorr of acetylene (Matheson purified grade, further purified by several liquid nitrogen freeze, evacuate, and thaw cycles and sublimed into the cell at thermal equilibrium with a pentane slush). The doubled PUMP laser (0.06 cm^{-1} resolution) is locked onto the peak of a single rotational line of the acetylene $\widetilde{A} \leftarrow \widetilde{X}$ transition via a fluorescence excitation scan.

$\widetilde{A} \rightarrow \widetilde{X}$ side fluorescence was imaged by S1UV f/1.9 collection optics onto matched photomultipliers (Hamamatsu R166 "solar blind" or Hamamatsu R331) in both the signal and reference cells. SCHOTT BG1, BG3, BG25, UG1 or UG5 filters were used to eliminate scattered light from the PUMP and DUMP laser beams. The outputs of the two photomultipliers are amplified by LeCroy VV100BTB amplifiers, and fed into a home built differential amplifier consisting of an Intersil 733 differential video amplifier and an OEI 9911 high current linear voltage follower (50Ω line driver). The output of the differential amplifier is detected by an SRS 250 boxcar. About 20 ns after the PUMP pulse has passed the photomultipliers, a DUMP pulse of 10 to 50 μJ counterpropagates along the PUMP beam path in the signal cell only. To maintain spatial overlap despite spatial fluctuations in the PUMP and DUMP beams, the DUMP beam is focused to a diameter of about 1mm and the PUMP beam to a diameter of 0.25mm at the photomultipliers, so that the entire volume of PUMPed molecules always interacts with the DUMP beam. To ensure good spatial overlap, particular attention is paid to the spatial beam quality (red color centers which develop in some fused silica optics can degrade the beam quality).

The boxcar gate was opened for 80 ns immediately after the termination of the DUMP pulse. The boxcar output was nulled in the absence of downward transitions by adjusting the differential amplifier. The boxcar sensitivity setting for SEP scans was typically 50mV with a 30 shot average. In this manner the difference in fluorescence signals between the signal (PUMP + DUMP) and reference (PUMP only) cells was recorded as a function of DUMP frequency.

2.1.2 Calibration

The β−BBO phase matching angle is continuously optimized by an autotracker as the DUMP laser is pressure scanned with SF_6. Approximately 4000 data points were recorded in a typical pressure scan, which covers about 10 cm^{-1}. The signal, a depletion of the side fluorescence in the signal cell as the doubled DUMP laser is scanned across a downward transition, is recorded simultaneously with the molecular iodine absorption spectrum of the DUMP fundamental by a PC with a National Instruments DT2801 A/D converter. Absolute term values of energy levels are calculated by subtracting the wavenumber of the SEP transition (obtained by calibrating versus the iodine lines) from the known term value of the $\widetilde{A} \leftarrow \widetilde{X}$ intermediate, see Chapter 1. This calibration method has a precision of about 0.010 cm^{-1} dictated by the absolute accuracy of the iodine atlas [2]. SEP term value coincidences indicated [3] a somewhat lower absolute accuracy of $2\bar{\sigma} = 0.020$ cm^{-1}; the slight decrease in absolute accuracy is mainly due to errors in locking the pump laser wavelength.

2.1.3 Saturation

Weak SEP transitions had a full width at half maximum (FWHM) of about 0.1 cm^{-1} comparable to the linewidth expected from convolution of the laser linewidth with the Doppler width for the DUMP transition. Early on in the course of the SEP experiments, the R branch DUMP transition in Q(3) PUMPed SEP (the lowest J possible) was detected. This is a surprise because the minimum detectable fluorescence dip at that time was about 0.5%, compared to a 14% dip for the Q branch DUMP transition, while the calculated intensity of the R branch transition in Q(3) PUMPed SEP spectrum was about 200 times less than that for the Q branch DUMP transitions. In addition the Q branch DUMP transitions had a FWHM of about 0.2 cm^{-1}, indicating a possible saturation of strongly allowed lines.

Of the PUMP and DUMP transitions, it would be difficult to saturate the weak PUMP transition, $f \approx 3.6\text{x}10^{-7}$ [4]. In addition, the observation of the correct expected rotational intensity pattern for both the fluorescence excitation spectrum ("PUMP only" spectra) and the weak SEP transitions indicates that

the PUMP transition is not saturated. Therefore, saturation of the PUMP transition cannot explain the observed incorrect Q branch SEP intensity ratios. The strongest DUMP transitions have FWHM roughly twice the FWHM of apparently unsaturated DUMP transitions. Furthermore, nominally forbidden Q branch DUMP transitions were detected that appear through well understood rotational-ℓ-resonance perturbations are calculated to be as weak relative to the strong Q branch DUMP transitions as the R-branch transitions mentioned above.

2.1.4 Linearity of the Fluorescence Detection

To check the possibility that the apparent nonlinear dependence of SEP intensities on calculated rotational linestrength might have been an experimental artifact due to a nonlinearity in the SEP detection scheme itself, a simple experiment was performed in which the fluorescence integrated by the boxcar was recorded by the PC from the signal and reference channels separately as a function of acetylene pressure measured by a capacitance manometer (MKS Baratron). The amplifiers, boxcar settings, PMT voltages, scattered light filters, maximum acetylene pressure, *etc.*, were identical to those used in the SEP experiments.

The integrated fluorescence was accurately predicted by the known Stern-Volmer fluorescence quenching constants for acetylene [5] and a fit of the observed vs. calculated fluorescence agreed to within 2% if the total fluorescence. This is somewhat better than the linearity expected from the specifications of the individual components in the SEP detection apparatus listed above. This measured non-linearity of the system response represents an upper bound for the combined non-linearity of all components involved in the detection of an SEP signal, and the non-linearity is actually even smaller over the range of detected fluorescence dips. The observed nonlinear dependence of the SEP signal on the transition probability for the DUMP transition is not an experimental artifact.

2.2 Spectroscopic Notation and Choice of Basis Set

Quantum mechanics allows eigenstates, zero-order states prepared in a specific experiment, transitions, *etc.*, to be described mathematically in any basis set as long as the basis set is complete, *i.e.* the basis set spans the full vector space of the problem. The *choice* of a basis set is not a "right" or "wrong" decision. On the contrary the choice is generally a matter of convenience, *e.g.* to simplify a calculation or to describe easily a transition. Quantum mechanics places a special significance on the eigenbasis since that is what one is "allowed" to measure (although technically no one ever measures eigenstates, only near-eigenstates since the measurement time is never $t = 0 - \infty$). Since an eigenlevel may be equivalently mathematically described by a single eigenstate OR a linear combination in any other basis, the complete description of the system in a generic basis set requires the specification of the "couplings" in that basis set (whence one calculates the particular expansion for that basis to describe the eigenstates). In this sense, the eigenbasis is *special* since there are no couplings. On the other hand, an experimentalist may consider the basis set which describes "cleanly" the states prepared by the laser to be the preferred basis set.

One final consideration in the selection of a basis set is to choose a basis set that describes the problem in an intuitive and predictive manner. Chemists tend to be highly visual and intuitive thinkers. Capturing the problem in a basis set that allows one to understand intuitively the dynamics is a hallmark of the models that are used throughout chemistry, simplified MO pictures, Lewis dot structures, *etc.*. One must remember that the strength of a model should reside in its predictive ability and ease of use; not on any "ultimate truths" which are unprovable and ultimately the realm of philosophy, not science.

The basis set used for acetylene in this thesis is the common one used in most spectroscopic applications. The rovibrational states are described in a product basis set made up of anharmonic oscillators for the "vibrational" part of the problem and rigid rotors (prolate top) for the "rotational" part of the problem. For the acetylene $\widetilde{A} \leftrightarrow \widetilde{X}$ transitions this basis set also happens to be the preferred basis set in regard to the ease with which the states prepared by the laser can be described.

The quantum numbers of the initial, intermediate and final levels in the SEP experiments are annotated with primes as shown in Figure 2.1, *e.g.* J'' or v_2'' denote the initial state, K' or v_1' denote the $\widetilde{A}$ state

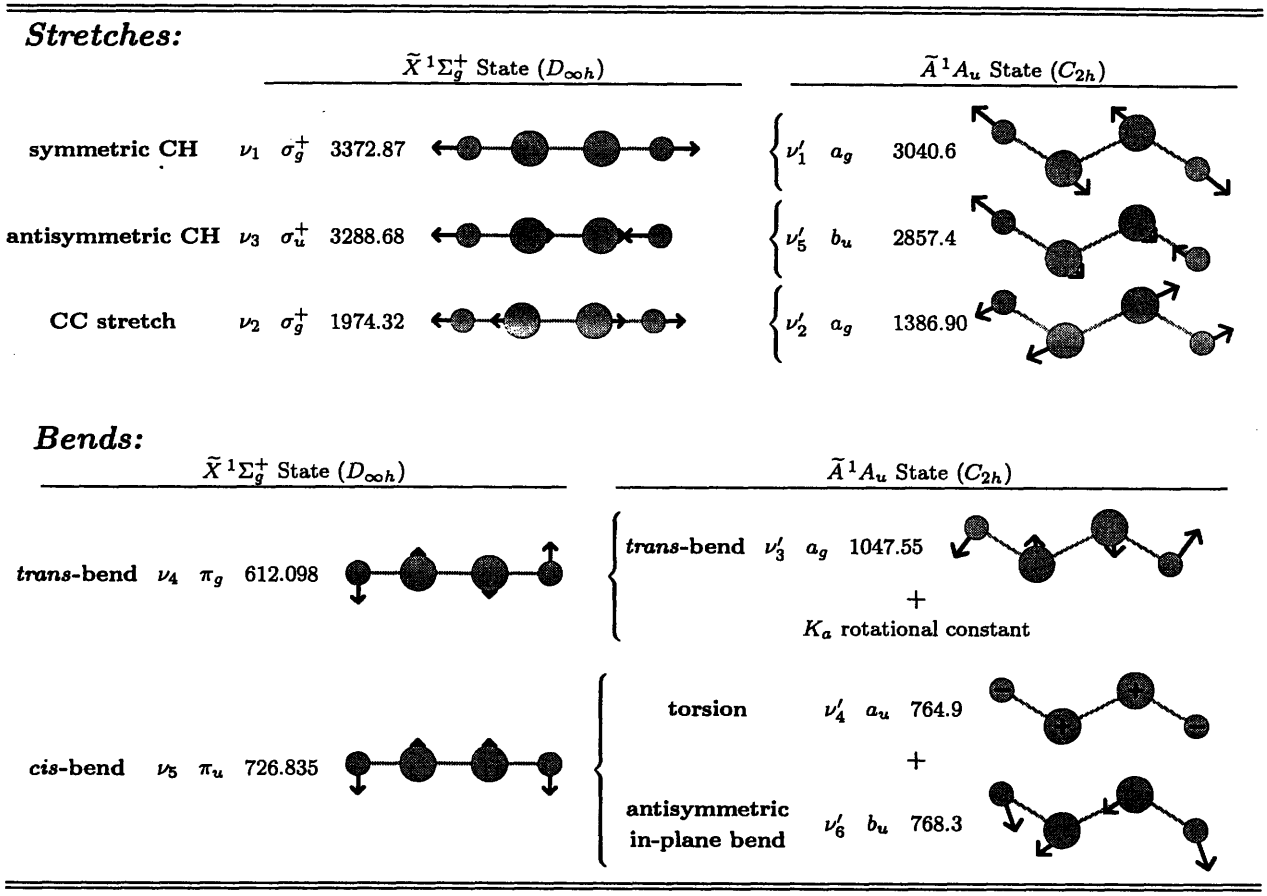

Table 2.1: The normal modes (seven vibrational degrees of freedom) for the $\widetilde{X}$ state of acetylene and their correlations to the modes (six vibrational degrees of freedom + one rotational degree of freedom) for the $\widetilde{A}$ state, including mode numbering, symmetries, frequencies in cm^{-1} ($\nu_i = \omega_i^0 + x_{ii}^0$) and vibrational motions [3,6–8].

intermediate , and J or ℓ the final state.

2.2.1 Vibrational Notation

The numbering of acetylene vibrational normal modes follows Herzberg's books [6, 7]. It is important to note that the reduction in symmetry of the $\widetilde{A}$ state compared to the $\widetilde{X}$ state results in a renumbering of the related normal modes, see Table 2.1. In particular, the *trans*-bend in the $\widetilde{X}$ state is ν_4, while the *trans*-bend in the $\widetilde{A}$ state is ν_3'. Also, to simplify the rotational selection rules for a bent to linear transition, Hougen and Watson's isomorphic Hamiltonian [9] description is used for the $\widetilde{X}$ state of acetylene allowing prolate top wavefunctions to be used for the rotational part of the wavefunction, with the constraint that $K = \ell$.

Since there is a large change in geometry between the linear and CC triple bonded ground state, $\widetilde{X}$ state, and the trans-bent and CC double bonded excited state, $\widetilde{A}$ state, acetylene $\widetilde{A} \rightarrow \widetilde{X}$ emission is dominated by long vibrational progressions in the *trans*-bend, ν_4 and the CC stretch, ν_2. Due to the previously mentioned *trans*-bend numbering changes between the $\widetilde{X}$ state and the $\widetilde{A}$ state, throughout this chapter a compact spectroscopic notation introduced by Watson [10] will be used to describe the PUMP vibronic, $V_{v_4''}^{v_3'} K_{\ell''}^{K_a'}$, and DUMP vibronic, $2_{v_2}^{v_2'} V_{v_4}^{v_3'} K_{\ell}^{K_a'}$, transitions. For instance, the PUMP transition from the zero-point level

of the $\widetilde{X}$ state (necessarily $K = \ell = 0$) to the vibrational level with two quanta in the $\widetilde{A}$ state *trans*-bend, $2\nu_3'$, would be represented as the $V_0^2 K_0^1$.

2.2.2 Rotational Notation

Since light and molecules both have definite parity, it is often advantageous to choose a basis set which takes advantage of this symmetry. For molecules it is often convenient to describe matrix elements in a *signed-K* basis set which is not an eigenrepresentation of parity. In practice, molecules are described initially in a signed-K basis set, then an orthogonal (unitary) transformation is done to transform to a parity basis where selection rules for transitions can be easily described.

Since the total parity for a level relies on the individual parity of the separate electronic, vibrational, rotational, *etc.*, wavefunctions AND the rotational parity in the Condon & Shortley phase convention is defined in the signed-K basis as:

$$\Pi_r |J, K\rangle = (-1)^{J-K} |J, -K\rangle \tag{2.1}$$

producing linear combinations

$$\text{Parity rotational states} \equiv \frac{1}{\sqrt{2}} \left(|J, K\rangle \pm |J, -K\rangle \right) \tag{2.2}$$

of signed-K rotational states that have definite parity, but whose parity alternates with J; it is often advantageous to define a parity label that defines the total parity of the state without the J dependence. These are the e/f symmetry labels. The e/f labels simplify the Hamiltonian since all e blocks have the same form for both even and odd J, and all f blocks have the same form for even and odd J. The 'e' parity label is defined as *even* total parity for *even* J and *odd* total parity for *odd* J; while, the 'f' parity label is defined as *even* total parity for *odd* J and *odd* total parity for *even* J. This labelling scheme also has the advantage of simplifying the transition selection rules as follows:

$$\begin{array}{rlll} Q \text{ branch transitions:} & \Delta J = 0; & e \leftrightarrow f & \\ P \text{ and } R \text{ branch transitions:} & \Delta J = \mp 1; & e \leftrightarrow e \text{ and } f \leftrightarrow f. & \end{array} \tag{2.3}$$

Since an allowed $\widetilde{A} \leftrightarrow \widetilde{X}$ transition in acetylene always entails a change in K, and since the forbidden transitions described in this chapter are deviations from the normal K dependence, a compact extension to the normal rotational transition notation, i.e. $Q(5)$, is in order. In a similar vein to the R(J) notation (where J denotes the J of the lower energy state in a transition and R denotes that $\Delta J = +1$, i.e. the upper state has a $J' = J + 1$), the K and ΔK are denoted as ${}^{\Delta K}\Delta J_{Ke/f}(J)$. For instance, an SEP DUMP transition from an $\widetilde{A}$ state level with $|J', K', e/f\rangle = |5', 1', f\rangle$ to an $\widetilde{X}$ state level with $|J, K, e/f\rangle = |4, 2, f\rangle$ would be denoted ${}^{P}R_{2f}(4)$.

2.3 Mechanisms for Forbidden Transitions

In the anharmonic oscillator/rigid rotor basis set the only rovibrationally forbidden transitions that can occur can be catalogued by the following mechanisms. Again each "mechanism" is merely an intuitive way to describe the particular form of the coupling matrix element or expansion coefficients needed to calculate the spectrum observed in the experiments.

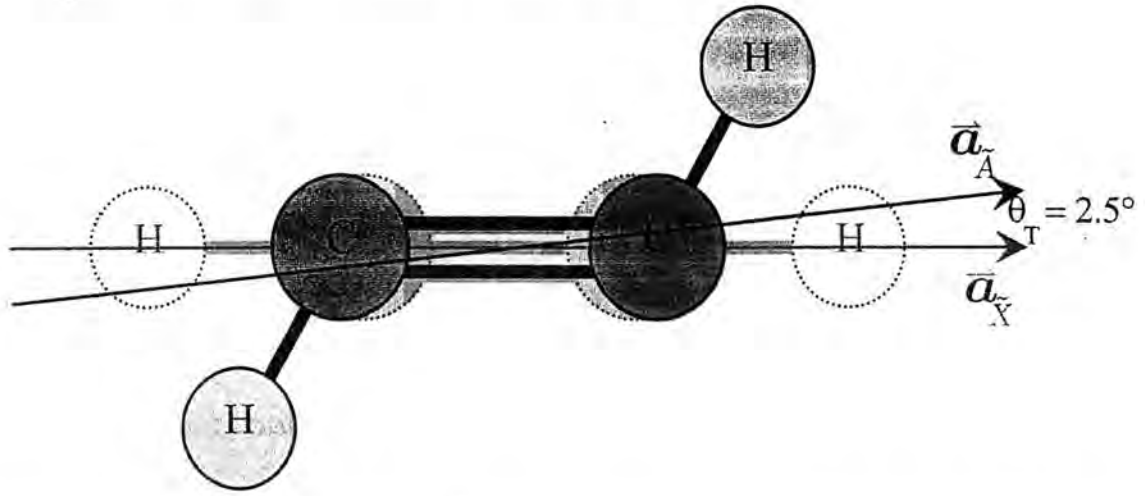

Figure 2.2: The $\vec{a}$ principal axis of the $\widetilde{A}$ state of acetylene is tilted by 2.5° with respect to that of the $\widetilde{X}$ state.

2.3.1 Asymmetry Induced Transitions

The $\widetilde{A}$ state is a near prolate top($A \gg B > C$), and therefore its rotational wavefunctions are linear combinations of prolate top ($A \gg B = C$) wavefunctions. By inspection of the rotational Hamiltonian, *i.e.* the $\hat{J}_x^2$ and $\hat{J}_y^2$ terms, the only K states that are mixed differ by $\Delta K = \pm 2$ (This is also obvious from the even/oddness of the rotational wavefunction nodes). This K-mixing results in $\Delta K = \pm 3, \pm 5 \ldots$ transition selection rules. The fraction of admixed K character can be approximated from second-order perturbation theory as $(H_{ij})^2/\Delta E^2$. Since [11]

$$\hat{\mathbf{H}}_{K,K\pm 2} = \frac{1}{4}(B-C)\sqrt{(J(J+1)-K(K\pm 1))(J(J+1)-(K\pm 1)(K\pm 2))} \tag{2.4}$$

and

$$\Delta E = (A - \frac{1}{2}(B+C))(K^2 - (K \pm 2)^2) \tag{2.5}$$

with $A \cong 13$, $B \cong 1.12$, and $C \cong 1.03$, the asymmetry induced transitions are approximately 10^{-5} weaker than the allowed $\Delta K = \pm 1$ transitions for the typical J's and K's in this experiment, and, therefore, are too weak to be observed.

2.3.2 Axis-Switching Transitions

The use of separate rotational and vibrational wavefunctions allows the calculation of transition intensities to be a simple product of the rotational line strengths, Hönl-London factors, and the squared vibrational overlap integral, the Franck-Condon factors. To the extent that rotation and vibration mean the same thing in the two electronic states, *axis-switching* transitions can occur if the Eckart frame of one state is not one to one mappable to the Eckart frame of the other. For instance, the $\widetilde{A}$ state is *trans*-bent and the $\widetilde{X}$ state is linear. This causes the $\vec{a}$ principal rotational axis to be tilted in one state relative to the other (See Figure 2.2). Therefore in evaluating the rotational transition intensity, the rotational integral

$$I = \left| \int \Psi^{\tilde{A}*} \Psi^{\tilde{X}} d\tau \right|^2 \approx \left| \int \cdots \int \Psi^{\tilde{A}*}_{rotational} \Psi^{\tilde{X}}_{rotational} \int \cdots d\tau \right|^2 \tag{2.6}$$

needs to have the $\widetilde{X}$ and $\widetilde{A}$ state rotational wavefunctions expressed in the same coordinate system. Either the $\widetilde{A}$ state must be expanded in $\widetilde{X}$ state rotational wavefunctions or *vice versa.* Hougen and Watson [12] showed that this expansion leads to selection rules that permit nominally forbidden $\Delta K = 0, \pm 1, \pm 2 \ldots$ transitions, since

$$|J,K\rangle_{\widetilde{A}} = \sum_{\ell} \mathcal{D}^{J}_{K,\ell}(0,\Theta_T,0)|J,\ell\rangle_{\widetilde{X}} \tag{2.7}$$

where Θ_T is the axis-switching angle, and $\mathcal{D}^{J}_{K,\ell}$ is Wigner's $\mathcal{D}$ matrix. Since the coefficient $\mathcal{D}^{J}_{K,\ell}(0,\Theta_T,0)$ can be approximated roughly as $\rho^n J^n$, where $\rho = \tan(\Theta_T/2)$ and $n = |K-\ell|$, axis-switching transitions become more intense relative to the allowed transitions roughly as J^2 [12].

In this manner, the $\widetilde{A}$ state rotational wavefunctions become mixtures of even AND odd K. In the $\widetilde{A} \leftarrow \widetilde{X}$ acetylene absorption spectrum this causes forbidden $\Delta K = 0$ and 2 rotational sub-bands to appear in allowed vibrational transitions [13]. Since, in the isomorphic Hamiltonian representation [9], $\widetilde{X}$ state vibrational wavefunctions are linked with either ℓ =even OR ℓ =odd rotational wavefunctions, *in bent→linear transitions, such as the $\widetilde{A} \rightarrow \widetilde{X}$ emission spectrum of acetylene, axis-switching causes the appearance of entirely new vibrational bands.*

This phenomenon follows from two facts: bent↔linear transitions are Franck-Condon active in the bending mode, and the even/oddness of vibrational quanta in the bend mode determines the even/oddness of ℓ. The values that the quantum number ℓ can assume are $\ell = -v_{bend}, -v_{bend}+2, \ldots, v_{bend}$, therefore emission from the $V_0^2 K_0^1$ $\widetilde{A}$ state level would allow transitions, $\Delta K = \pm 1$, to $\ell = 0$ or 2, which occur only for $\widetilde{X}$ state vibrational levels with even quanta of *trans*-bend. No odd quanta in the *trans*-bend would appear in the spectrum. With axis-switching the same $\widetilde{A}$ state level could now access odd ℓ levels which belong to odd *trans*-bend vibrational levels.

Just as for allowed transitions the intensity of an axis switching transition is given by the product of a rotational line strength factor and a vibrational Franck-Condon factor. Since these two factors are independent, a nominally forbidden axis-switching transition with a large Franck-Condon factor may be unexpectedly intense compared to an allowed transition with a small Franck-Condon factor.

Axis-switching is *not* a perturbation, *i.e.* there is no coupling of levels within a single electronic state, no level repulsion, no mixing of character. Axis-switching comes from the transition itself, the projection of the $\widetilde{A}$ state principal axis system onto the $\widetilde{X}$ state.

2.3.3 Forbidden Transitions Occurring via Coriolis Perturbations

In contrast to axis-switching, Coriolis coupling involves a mixing of zero-order vibrational character. The mechanism of Coriolis coupling can be understood by examining the classical mechanical derivation of the Coriolis force. Coriolis effects derive from the fact that the molecule fixed frame within which the vibrational coordinates are described, is not an inertial frame, *i.e.* it is a rotating, therefore accelerated, frame. In classical mechanics a generic force, $\vec{\mathbb{F}}^{external}$, that is describable in an inertial frame, and therefore governed by Newton's laws,

$$\left.\frac{md^2\vec{r}_0}{dt^2}\right|_{inertial} = \vec{\mathbb{F}}^{external}, \tag{2.8}$$

where $\vec{r}_0$ are the coordinates in the inertial frame, can be transformed to the rotating reference frame or body frame [14], where $\vec{r}$ are the object coordinates in the body frame, $\vec{a}$ are the coordinates of the origin of the rotating reference frame, and $\vec{\omega}$ is the angular velocity. In doing so, the forces "seen" by the objects in the body frame are the original force, $\vec{\mathbb{F}}^{external}$,

$$\left.\frac{md^2\vec{r}}{dt^2}\right|_{body} = \vec{\mathbb{F}}^{external} \underbrace{-\frac{md^2\vec{a}}{dt^2}}_{\text{translational}} \underbrace{-2m\vec{\omega}\times\left.\frac{d\vec{r}}{dt}\right|_{body}}_{\text{Coriolis}} \underbrace{-m\vec{\omega}\times(\vec{\omega}\times\vec{r})}_{\text{centrifugal}} \underbrace{-m\frac{d\vec{\omega}}{dt}\times\vec{r}}_{\text{azimuthal}} \tag{2.9}$$

with the addition of four "fictitious" forces: the translational force, the Coriolis force, the centrifugal force, and the azimuthal force. For isolated molecules the translational and azimuthal forces are zero, because there is no acceleration of the rotating frame origin and no change in the angular velocity. Coriolis forces in molecules come about from the simple fact that the atoms are moving (vibrating) which causes the atoms to feel a force perpendicular to the path of their vibrational motions. For instance, atoms in a linear molecule while undergoing a stretching motion along the central axis will feel a perpendicular pull off the central axis. This off-axis motion corresponds to a bending vibrational motion, hence, the Coriolis effects are said to mix vibrations in a molecule that differ by a rotation. Using point group symmetry the possible Coriolis mixings can be found, requiring only the inspection of the vibrational motions to conclude positively if the vibrations in question are actually Coriolis coupled. The beauty of the Coriolis force arises from the fact that since the transformation to the Eckart axis is completely known, the form of the Coriolis coupling is explicitly calculable once the body frame is chosen. In addition the Eckart axes are defined by requiring that Coriolis forces are minimized.

For the specific symmetry of linear molecules, such as the $\widetilde{X}$ state, Coriolis coupling occurs between states that differ by one quantum in the stretch and one quantum in the bend. Therefore, states are coupled that differ in ℓ by one quantum, $\Delta\ell = \pm 1$, causing mixing of the ℓ character as well as the vibrational character. In the $\widetilde{A}$ state, two of the three forms of Coriolis coupling can also mix the K character, $\Delta K' = \pm 1$. These non-rigidity effects will then produce nominally forbidden $\Delta K = 0$, and 2 transitions. In both the $\widetilde{X}$ and $\widetilde{A}$ states multiple Coriolis steps can mix several K's and ℓ's producing transitions involving larger effective $\Delta K = \pm 2, \pm 3$, *etc.*

Although the Coriolis and axis-switching mechanisms allow the same ΔK selection rules, the Coriolis mechanism is an actual perturbation and should be detectable as such allowing the discrimination of the two mechanisms.

2.3.4 Forbidden Transitions Occurring via Rotational-ℓ-Resonance

Rotational-ℓ-resonance in linear molecules, such as the $\widetilde{X}$ state of acetylene, is a special case of a two-step Coriolis interaction. In rotational-ℓ-resonance, an $\widetilde{X}$ state vibrational level, $(v_{bend}, v_{stretch})^{\ell}$, might be Coriolis coupled to another level, $(v_{bend} \pm 1, v_{stretch} \mp 1)^{\ell+1}$, which could then also Coriolis coupled back to $(v_{bend}, v_{stretch})^{\ell+2}$. Since the energy difference between the $(v_{bend} \pm 1, v_{stretch} \mp 1)$ and $(v_{bend}, v_{stretch})$ levels is at least $\nu_2 - \nu_4 \cong 1300\text{cm}^{-1}$, and the difference between the ℓ and $\ell+2$ levels is roughly $4(g_{44} - B_v)(\ell+1) \cong 2\ \text{cm}^{-1}$ at $\ell = 0$, a Van Vleck transformation may be done to produce an effective coupling matrix element between the ℓ and $\ell + 2$ levels belonging to the same $(v_{bend}, v_{stretch})$. For the $\widetilde{X}$ state acetylene levels discussed here the rotational-ℓ-resonance interaction has the following coupling term:

$$\langle v_4; J, \ell | \mathcal{H} | v_4; J, \ell \pm 2| = \frac{1}{4} q_4 \sqrt{(v_4 \mp \ell)(v_4 \pm \ell + 2)} \sqrt{(J(J+1) - \ell(\ell \pm 1))(J(J+1) - (\ell \pm 1)(\ell \pm 2))}. \quad (2.10)$$

As can be seen the rotational-ℓ-resonance mechanism would be expected to exhibit a roughly J^4 dependence on the intensities, which does indeed dramatically affect the relative ℓ intensities as well accounts for the appearance of $\Delta K = 3$ transitions in the SEP spectrum.

2.3.5 Intensity Interference Effects

The $\widetilde{A}$ state $K' = 1$ levels reached by the Q branch PUMP transitions from the ground vibrational state have the same parity as $K' = 0$ levels, therefore they can acquire both $K' = 0$ and $K' = 2$ character when they are transformed to the Eckart axes of the $\widetilde{X}$ state. If the expansion coefficients for $K' = 0$ and $K' = 2$ character have opposite signs, as in axis-switching, then it can be easily shown from the direction cosine matrix elements [15] that the signs of the c-dipole transition moments are such that the $K' = 0$ and $K' = 2$ characters interfere constructively in Q branch DUMP transitions and destructively in P or R branch

DUMP transitions. The $\widetilde{A}$ state $K' = 1$ levels reached by R or P branch PUMP transitions from the ground vibrational state do not have the same parity as the $K' = 0$ levels and thus can acquire only $K' = 2$ and not $K' = 0$ character. The $K' = 1 \rightarrow \ell = 1$ transitions in R branch PUMPed SEP are therefore weaker than the $K' = 1 \rightarrow \ell = 1$ Q PUMP/Q DUMP transitions.

Another intensity effect comes about from the relative polarizations of the PUMP and DUMP lasers. In this experiment the PUMP and DUMP lasers were linearly polarized and parallel to each other. In this configuration if the PUMP laser transition is not saturated then the M_J-sublevel population in the prepared $\widetilde{A}$ state is preferentially biased differently for Q PUMP versus P and R PUMP transitions. As can be seen from the direction cosine matrix elements the Q PUMP transition populates preferentially higher $|M_J|$ levels, and conversely P and R PUMP transitions preferentially populate low $|M_J|$ levels. When these biased populations are followed by an additional P, Q or R DUMP transition that is also linearly polarized and parallel to the PUMP linear polarization, it is easy to see that a Q PUMP followed by a Q DUMP would have a constructive effect versus a Q PUMP followed by a P or R DUMP transition and *vice versa.*

Taking the relative laser polarization and the interference effect into account, a calculation of the SEP DUMP transition rotational intensities from a Q PUMP level ($J' > 3$) shows that the "allowed" ${}^pR_{2f}$ SEP DUMP transition is expected to be *weaker* than the strongest "forbidden" ${}^qQ_{1e}$ axis-switching SEP DUMP transition. *Since the "allowed" ${}^pR_{2f}$ SEP DUMP transitions are easily observed detection of the nominally forbidden axis-switching transitions should be expected.*

2.4 Spectroscopic Assignments of the Observed Forbidden Transitions

2.4.1 Rotational Assignments

The rotational assignments for a double resonance experiment are confirmed by term value coincidences. Since J', K'_a and parity are known for the intermediate state, and rigorous selection rules for transitions limit $\Delta J = 0, \pm 1$ and parity $+ \leftrightarrow -$, the final state after a SEP DUMP transition is easily identified by the appearance of the same $J_{\ell,\text{parity}}$ level at coinciding term values in at least two separate spectra from different PUMP transitions. In other words, the same final $J_{\ell,\text{parity}}$ $\widetilde{X}$ state level may be accessed from multiple PUMP preparations. For example, the $J_{\ell,\text{parity}} = 6_{2f}$ level can be accessed from a $V_0^2K_0^1$ vibrational intermediate via a ${}^pP_{2f}(6)$ DUMP transition following a ${}^rQ_{0e}(5'')$ PUMP, a ${}^pR_{2f}(6)$ DUMP transition following a ${}^rQ_{0e}(7'')$ PUMP, or a ${}^pQ_{2f}(6)$ DUMP transition following a ${}^rR_{0e}(5'')$ PUMP. For strong transitions, the value of ℓ can be determined from: the disappearance of the strong transition at $\ell < J$; for $\ell > 0$, the convergence at low ℓ of the e and f pair of opposite parity states for the same value of ℓ; for $\ell = 0$, a single parity state; and other clues in coincidence with the vibrational assignment. All of the "allowed" transitions in the 7,000 cm^{-1} SEP study [3] were assigned in this manner.

The forbidden, $\Delta K \neq \pm 1$, transitions found in the same $V_0^2K_0^1$ SEP study and discussed in a preliminary fashion in Ref. [1], are listed in Table 2.2.

For $J' \geq 5$ the allowed ${}^rQ_{0e}$ and ${}^pQ_{2e}$ DUMP transitions were accompanied by a transition separated by nearly constant energy. From the values of the rotational-ℓ-resonance constants, a calculation of the position of the $\ell = 4$ levels is consistent with these observed levels. In addition, since the intensity of the rotational-ℓ-resonance levels grows roughly as J^4, the increase in intensity of these transitions with J as well as the Hamiltonian fits described in the next section, further support these assignments.

In addition to the $\ell = 4$ levels, $\ell = 1$ levels were observed and their J and ℓ assignments confirmed by SEP experiments using the $V_1^2K_1^0$ $\widetilde{A}$ state intermediate where they become the allowed transitions. The relative positions of the $\ell = 3$ levels, which are detectable due to rotational-ℓ-resonance, were confirmed in the same manner as the $\ell = 4$ levels above.

	Vibrational Character	Rotational Character	Term Value/cm^{-1}
$\Delta K = \pm 3$	(0 , 1 , 0 , 8 , 0)	$5_{4,e}$	6988.11
	(0 , 1 , 0 , 8 , 0)	$6_{4,e}$	7002.24
	(0 , 1 , 0 , 8 , 0)	$7_{4,e}$	7018.76
	(0 , 1 , 0 , 8 , 0)	$8_{4,e}$	7037.61
	(0 , 1 , 0 , 8 , 0)	$9_{4,e}$	7058.79
	(0 , 1 , 0 , 8 , 0)	$11_{4,e}$	7108.17
	(0 , 1 , 0 , 8 , 0)	$9_{4,f}$	7058.83
	(0 , 1 , 0 , 8 , 0)	$10_{4,f}$	7082.34
$\Delta K = 0$	(0 , 2 , 0 , 5 , 0)	$3_{1,e}$	6958.20
	(0 , 2 , 0 , 5 , 0)	$4_{1,e}$	6967.44
	(0 , 2 , 0 , 5 , 0)	$5_{1,e}$	6979.09
	(0 , 2 , 0 , 5 , 0)	$6_{1,e}$	6993.03
	(0 , 2 , 0 , 5 , 0)	$7_{1,e}$	7009.30
	(0 , 2 , 0 , 5 , 0)	$8_{1,e}$	7027.91
	(0 , 2 , 0 , 5 , 0)	$9_{1,e}$	7048.83
$\Delta K = \pm 2$	(0 , 2 , 0 , 5 , 0)	$5_{3,e}$	6974.98
	(0 , 2 , 0 , 5 , 0)	$6_{3,e}$	6988.99
	(0 , 2 , 0 , 5 , 0)	$7_{3,e}$	7005.35
	(0 , 2 , 0 , 5 , 0)	$8_{3,e}$	7024.04
	(0 , 2 , 0 , 5 , 0)	$9_{3,e}$	7045.02

Table 2.2: Forbidden transitions observed in the $V_0^2 K_0^1$ SEP spectrum of acetylene

2.4.2 Vibrational Assignments

Since the CC and CH stretch vibrational character in acetylene has a dramatic and opposite effect to the bending character with respect to rotational constants, the effective $B_v = B_0 - \sum \alpha_i v_i$ values has been a good indication of the dominant vibrational character of levels in these SEP experiments. The fitted B_v values agree very well with the vibrational assignments.

2.5 Least Squares Fitting

The observed $(0,1,0,8,0)$ and $(0,2,0,5,0)$ levels from the $V_0^2K_0^1$, $V_1^2K_1^0$, $V_0^0K_0^1$ and $V_1^0K_1^0$ $\tilde{A}$ state intermediate levels are tabulated in Table 2.3.

These $(0,1,0,8,0)$ and $(0,2,0,5,0)$ levels were each fit to four parameter effective Hamiltonians which contained the effects of rotational-ℓ-resonance and doubling. The non-linear least squares fits used the Levenberg-Marquardt algorithm [16] with derivatives calculated using the Hellmann-Feynman theorem [17]. The $(0,1,0,8,0)$ and $(0,2,0,5,0)$ levels were fit together in each e and f parity block to facilitate the investigation of Coriolis coupling *between* the $(0,1,0,8,0)$ and $(0,2,0,5,0)$ levels. Since the ℓ levels for $(0,1,0,8,0)$ and $(0,2,0,5,0)$ are interleaved, see Fig. 2.3, a simple ordering of the eigenvalues is insufficient to map the eigenvalues of the Hamiltonian matrix to the observed data. The eigenvalues were first separated based on the eigenvector's maximum $(0,1,0,8,0)$ or $(0,2,0,5,0)$ zero-order state character, then sorted by energy to map to the corresponding ℓ state. The Hamiltonian for the e parity block had the form shown in Table 2.4.

The Hamiltonian for the f parity block had the form shown in Table 2.5.

2.5.1 Fits with No Coriolis Interaction Between $(0,1,0,8,0)$ and $(0,2,0,5,0)$

Three separate fits were performed: a "low ℓ" fit, a "weighted J" fit and an "all ℓ" fit. The fitted parameters are collected in Table 2.6 and a reduced term value plot of all levels is shown in Figure 2.3.

To examine the effect of excluding the high ℓ levels, the "low ℓ" fit included only the ℓ=0–3 levels in the observed data and in the Hamiltonian. Since the effect of rotational-ℓ-resonance grows as roughly J^2 and therefore the effect of the high ℓ levels was expected to become more important, a "weighted J" fit was performed by preferentially decreasing the weighting of the high J values, but still only considering the ℓ=0–3 levels.

Compared to the previous two fits, the inclusion of the full ℓ Hamiltonian is an obvious improvement, see in particular Figures 2.4.

The effective rotational constants agree closely with the predicted zero order rotational constants. The effective rotational-ℓ-resonance and doubling constants 4.88(8) and 5.42(10) are evidently different. Both vibrational term values are about 10 cm^{-1} higher than predicted by the anharmonic expansion, see Chapter 5. The effective g_44 constants differ substantially because CC stretching has a large effect on g_44 [3].

2.5.2 Fits with a Coriolis Interaction Between $(0,1,0,8,0)$ and $(0,2,0,5,0)$

Since the possibility existed that the $(0,2,0,5,0)$ levels were able to be seen in the $V_0^{0,2}K_0^1$ SEP spectrum and the $(0,1,0,8,0)$ levels were able to be seen in the $V_1^{0,2}K_1^0$ SEP spectrum via an $\tilde{X}$ state Coriolis interaction between the $(0,1,0,8,0)$ and $(0,2,0,5,0)$ levels, several pathways (and therefore matrix element forms) for the possible interactions were tested. The complete derivation and effective corrections to other constants, such as the B values will be investigated in a future paper. Suffice it to say, since the interaction would be a third-order Coriolis effect, the Coriolis matrix elements would be roughly proportional to $(\sqrt{J(J+1)})^3$. All fits to any form of the Coriolis matrix element forced the fitted prefactor to zero with a $2\sigma < 10^{-4}$. The future paper will explore this avenue in more detail placing hard upper bounds on the possible size of this type of an element and its maximum intensity contribution to the observed levels.

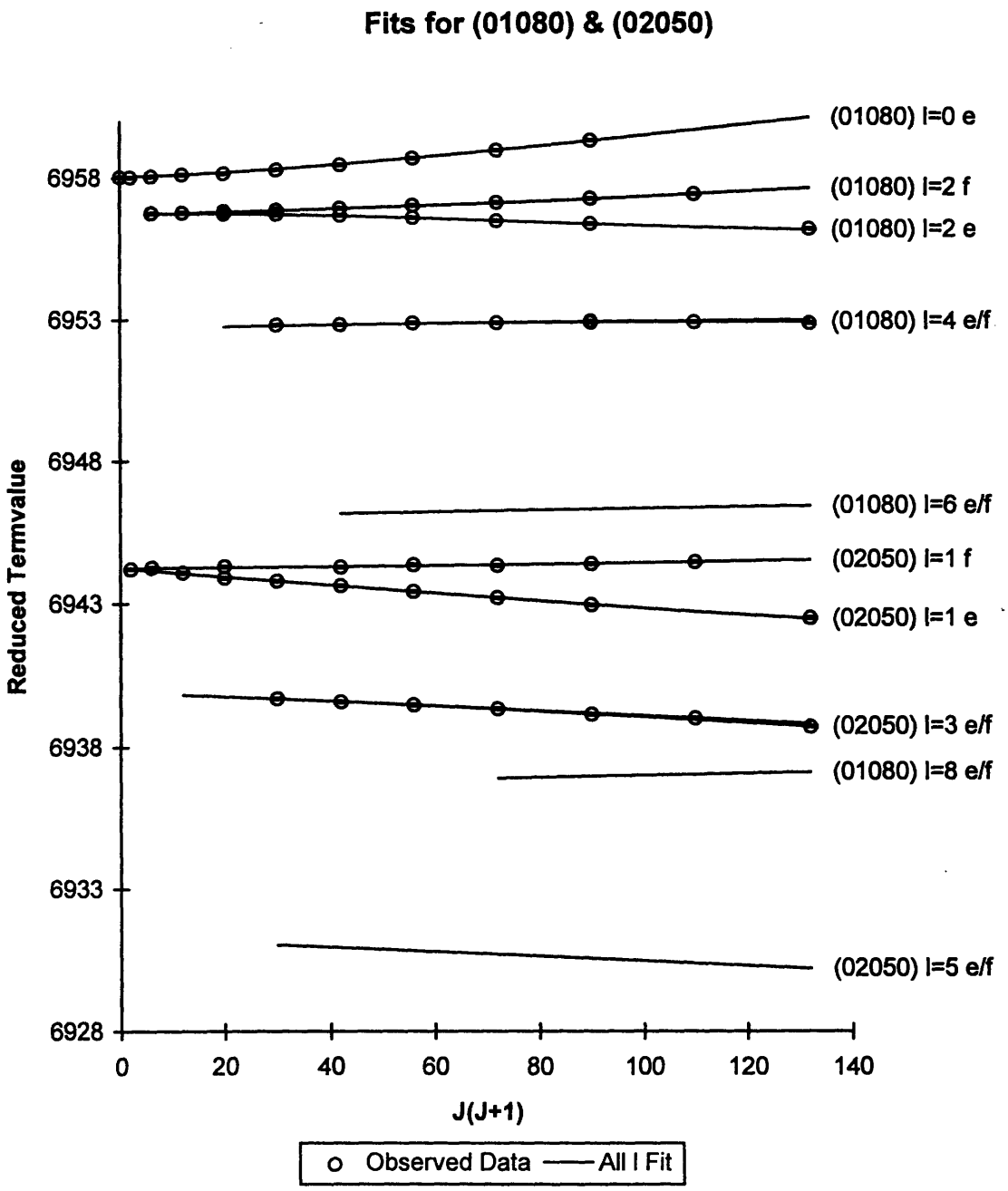

Figure 2.3: A reduced term value plot showing all of the vibrational levels and the observed data.

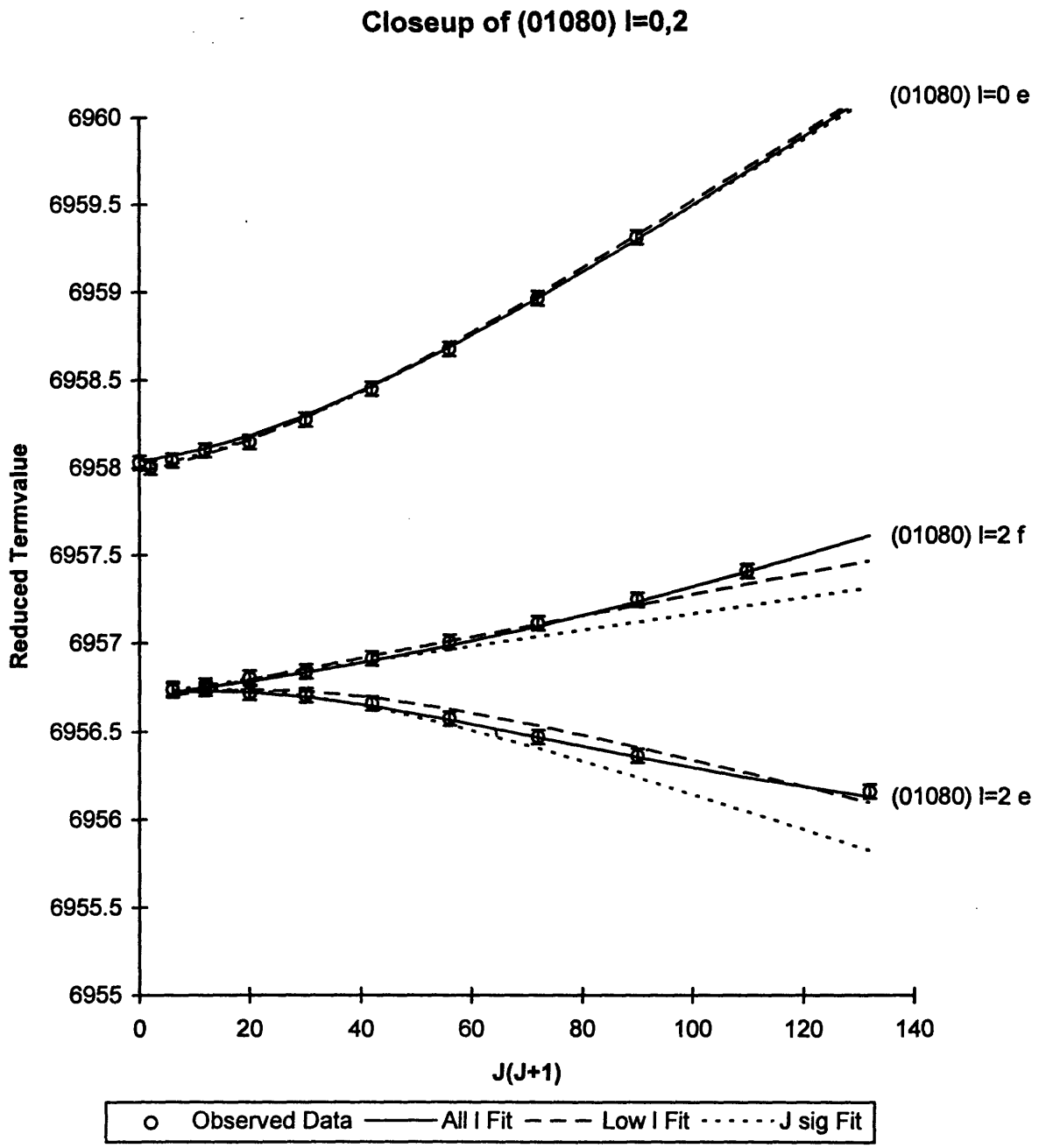

Figure 2.4: A reduced term value plot for the $(0,1,0,8,0)$ vibrational levels for ℓ=0 and 2.

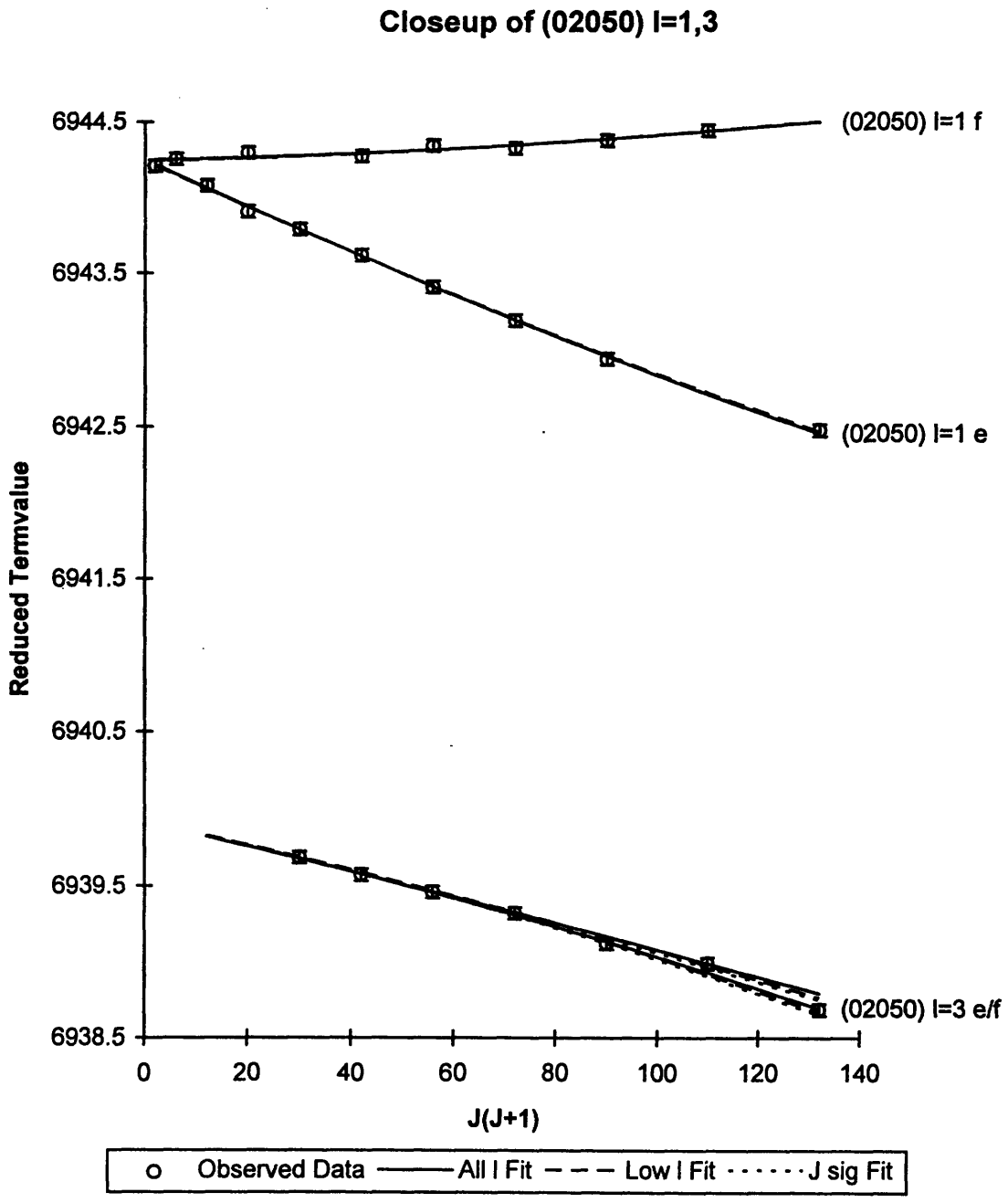

Figure 2.5: A reduced term value plot for the $(0,2,0,5,0)$ vibrational levels for ℓ=1 and 3.

Vibrational Character	J	Term Value (cm^{-1})	Vibrational Character	J	Term Value (cm^{-1})
(0,1,0,8,0) $\ell = 0e$	0	6958.029	(0,1,0,8,0) $\ell = 2f$	2	6963.801
	1	6960.356		3	6970.878
	2	6965.102		4	6980.336
	3	6972.219		5	6992.137
	4	6981.680		6	7006.330
	5	6993.572		7	7022.895
	6	7007.868		8	7041.828
	7	7024.566		9	7063.140
	8	7043.679		10	7086.834
	9	7065.203	(0,1,0,8,0) $\ell = 4f$	9	7058.830
(0,1,0,8,0) $\ell = 2e$	2	6963.793		10	7082.341
	3	6970.861	(0,2,0,5,0) $\ell = 1f$	2	6951.313
	4	6980.251		4	6967.825
	5	6992.003		6	6993.689
	6	7006.077		7	7010.230
	7	7022.465		8	7029.040
	8	7041.187		9	7050.271
	9	7062.259		10	7073.867
	11	7111.474	(0,2,0,5,0) $\ell = 3f$	10	7068.422
(0,1,0,8,0) $\ell = 4e$	5	6988.109			
	6	7002.243			
	7	7018.763			
	8	7037.606			
	9	7058.790			
	11	7108.170			
(0,2,0,5,0) $\ell = 1e$	1	6946.561			
	3	6958.196			
	4	6967.437			
	5	6979.086			
	6	6993.034			
	7	7009.299			
	8	7027.906			
	9	7048.835			
	11	7097.788			
(0,2,0,5,0) $\ell = 3e$	5	6974.984			
	6	6988.991			
	7	7005.351			
	8	7024.039			
	9	7045.021			
	11	7094.005			

Table 2.3: The observed $(0,1,0,8,0)$ and $(0,2,0,5,0)$ levels from the $V_0^2K_0^1$, $V_1^2K_1^0$, $V_0^0K_0^1$ and $V_1^0K_1^0$ $\tilde{A}$ state intermediate SEP experiments.

$$
\begin{array}{ccccccccc}
 & & (0,1,0,8,0)\ e \text{ parity states} & & & & (0,2,0,5,0)\ e \text{ parity states} & & \\
\ell=0 & \ell=2 & \ell=4 & \ell=6 & \ell=8 & & \ell=1 & \ell=3 & \ell=5 \\
\begin{pmatrix}
T_8(J,\ell) & Q_8^*(J,\ell) & 0 & 0 & 0 & & & & \\
Q_8^*(J,\ell) & T_8(J,\ell) & Q_8(J,\ell) & 0 & 0 & & & & \\
0 & Q_8(J,\ell) & T_8(J,\ell) & Q_8(J,\ell) & 0 & & & & \\
0 & 0 & Q_8(J,\ell) & T_8(J,\ell) & Q_8(J,\ell) & & & & \\
0 & 0 & 0 & Q_8(J,\ell) & T_8(J,\ell) & & & & \\
 & & & & & & T_5^\dagger(J,\ell) & Q_5(J,\ell) & 0 \\
 & & & & & & Q_5(J,\ell) & T_5(J,\ell) & Q_5(J,\ell) \\
 & & & & & & 0 & Q_5(J,\ell) & T_5(J,\ell)
\end{pmatrix}
\end{array}
$$

$$M = J(J+1)$$

$$
\text{for } (0,1,0,8,0) \begin{cases}
T_8 = G_8 + \Delta_8 \ell^2 + B_8 M \\
Q_8 = \langle v_4, \ell | \mathcal{H} | v_4, \ell \pm 2 \rangle \\
\quad = \dfrac{1}{4} q_8 \sqrt{(v_4 \mp \ell)(v_4 \pm \ell + 2)} \sqrt{(M - \ell(\ell \pm 1))(M - (\ell \pm 1)(\ell \pm 2))} \\
Q_8^* = \sqrt{2} Q_8
\end{cases}
$$

$$
\text{for } (0,2,0,5,0) \begin{cases}
T_5 = G_5 + \Delta_5 \ell^2 + B_5 M \\
T_5^\dagger = T_5 - \frac{1}{4} q_5 M \\
Q_5 = \langle v_4, \ell | \mathcal{H} | v_4, \ell \pm 2 \rangle \\
\quad = \dfrac{1}{4} q_5 \sqrt{(v_4 \mp \ell)(v_4 \pm \ell + 2)} \sqrt{(M - \ell(\ell \pm 1))(M - (\ell \pm 1)(\ell \pm 2))}
\end{cases}
$$

Table 2.4: The fit Hamiltonian for the e parity block.

$$
\begin{array}{cccc|ccc}
\multicolumn{4}{c|}{(0,1,0,8,0)\ f \text{ parity states}} & \multicolumn{3}{c}{(0,2,0,5,0)\ f \text{ parity states}} \\
\ell=2 & \ell=4 & \ell=6 & \ell=8 & \ell=1 & \ell=3 & \ell=5 \\
\left(\begin{array}{cccc} T_8(J,\ell) & Q_8(J,\ell) & 0 & 0 \\ Q_8(J,\ell) & T_8(J,\ell) & Q_8(J,\ell) & 0 \\ 0 & Q_8(J,\ell) & T_8(J,\ell) & Q_8(J,\ell) \\ 0 & 0 & Q_8(J,\ell) & T_8(J,\ell) \end{array}\right. & & & & \left.\begin{array}{ccc} T_5^{\ddagger}(J,\ell) & Q_5(J,\ell) & 0 \\ Q_5(J,\ell) & T_5(J,\ell) & Q_5(J,\ell) \\ 0 & Q_5(J,\ell) & T_5(J,\ell) \end{array}\right)
\end{array}
$$

$$M = J(J+1)$$

$$\text{for } (0,1,0,8,0)\begin{cases} T_8 = G_8 + \Delta_8\ell^2 + B_8M \\ Q_8 = \langle v_4,\ell|\mathcal{H}|v_4,\ell\pm 2\rangle \\ \quad = \dfrac{1}{4}q_8\sqrt{(v_4\mp\ell)(v_4\pm\ell+2)}\sqrt{(M-\ell(\ell\pm1))(M-(\ell\pm1)(\ell\pm2))} \end{cases}$$

$$\text{for } (0,2,0,5,0)\begin{cases} T_5 = G_5 + \Delta_5\ell^2 + B_5M \\ T_5^{\ddagger} = T_5 + \frac{1}{4}q_5M \\ Q_5 = \langle v_4,\ell|\mathcal{H}|v_4,\ell\pm 2\rangle \\ \quad = \dfrac{1}{4}q_5\sqrt{(v_4\mp\ell)(v_4\pm\ell+2)}\sqrt{(M-\ell(\ell\pm1))(M-(\ell\pm1)(\ell\pm2))} \end{cases}$$

Table 2.5: The fit Hamiltonian for the f parity block.

Fit	G_8	Δ_8	B_8	Q_8
all ℓ	6958.04(1)	-0.335(1)	1.1806(2)	0.00122(2)
low ℓ	6957.98(2)	-0.327(5)	1.1826(2)	0.00115(2)
weighted J	6958.01(2)	-0.325(6)	1.1812(9)	0.00122(8)

Fit	G_5	Δ_5	B_5	Q_5
all ℓ	6944.79(2)	-0.542(3)	1.1691(2)	0.00135(3)
low ℓ	6944.78(2)	-0.540(3)	1.1692(2)	0.00135(3)
weighted J	6944.79(2)	-0.541(3)	1.1691(3)	0.00135(3)

Table 2.6: The fitted constants.

2.6 SEP From the Zero-Point Level

SEP experiments were also carried out using the $V_0^0K_0^1$ and $V_1^0K_1^0$ $\widetilde{A}$ state intermediates. Since the closest $\widetilde{A}$ state vibrational level to which the zero-point level could be connected via Coriolis is 764 cm^{-1} away, the largest Coriolis mixed character in these zero-point levels would be on the order of 10^{-4}. Since the (0,1,0,8,0) level was observed as a forbidden level from the $V_1^0K_1^0$ $\widetilde{A}$ state intermediate, the predominant mechanism for the intensity must be axis-switching since it could not be $\widetilde{A}$ state Coriolis for these levels or $\widetilde{X}$ state Coriolis from the fits of the previous section.

The SEP data from the four $\widetilde{A}$ state intermediates give us an excellent opportunity to calculate intensity and compare them to the SEP data as well as the Franck-Condon data available from the DF analysis presented later in this thesis. The intensity calculations will be presented in the forthcoming paper.

References

[1] D. M. Jonas, S. A. B. Solina, B. Rajaram, R. J. Silbey, R. W. Field, K. Yamanouchi, S. Tsuchiya. *J.Chem.Phys.* **97**(4), 2813 (1992).

[2] S. Gerstenkorn, P. Luc. *Atlas du Spectre de la Moléculair de l'Iode entre 14,800-20,000 cm^{-1}*. Editions du C.N.R.S., Paris (1979).

[3] D. M. Jonas, S. A. B. Solina, B. Rajaram, R. J. Silbey, R. W. Field, K. Yamanouchi, S. Tsuchiya. *J.Chem.Phys.* **99**(10), 7350 (1993).

[4] C. K. Ingold, G. W. King. *J.Chem.Soc.* **1953**, 2702 (1953).

[5] J. C. Stephenson, J. A. Blazy, D. King. *Chem.Phys.* **85**, 31 (1984).

[6] G. Herzberg. *Molecular Spectra and Molecular Structure, Volume II - Infrared and Raman Spectra of Polyatomic Molecules.* Krieger Publishing Company, Malabar, FL (1991).

[7] G. Herzberg. *Molecular Spectra and Molecular Structure, Volume III - Electronic Spectra and Electronic Structure of Polyatomic Molecules.* Krieger Publishing Company, Malabar, FL (1991).

[8] J. D. Tobiason, A. L. Utz, E. L. Sibert III, F. F. Crim. *J.Chem.Phys.* **99**(8), 5762 (1993).

[9] P. R. Bunker. *Molecular Symmetry and Spectroscopy.* Academic Press, Inc., San Diego, CA (1979).

[10] J. K. G. Watson, M. Herman, J. C. Van Craen, R. Colin. *J.Mol.Spectros.* **95**(1), 101 (1982).

[11] R. N. Zare. *Angular Momentum.* John Wiley & Sons, Inc., New York, NY (1988).

[12] J. T. Hougen, J. K. G. Watson. *Can.J.Phys.* **43**, 298 (February 1965).

[13] K. K. Innes. *J.Chem.Phys.* **22**, 863 (1954).

[14] j. B. Marion, S. T. Thornton. *Classical Dynamics of Particles & Systems.* Harcourt Brace Jovanovich, Inc, San Diego, CA (1988).

[15] C. H. Townes, A. L. Schawlow. *Microwave Spectroscopy.* Dover Publications, Inc., New York, NY (1975).

[16] W. H. Press, B. P. Flannery, S. A. Teukolsky, W. T. Vetterling. *Numerical Recipes: The Art of Scientific Computing.* Cambridge University Press, New York, NY (1988).

[17] H. Lefebvre-Brion, R. W. Field. *Perturbations in the Spectra of Diatomic Molecules.* Academic Press, Inc., Orlando, FL (1986).

Chapter 3

Infrared-Ultraviolet Double Resonance in Acetylene

To understand the global dynamics of acetylene, spectra need to be recorded which sample many areas of the potential surface. Traditional infrared (IR) and Raman studies only probe the IR and Raman fundamentals and a few overtone, combination bands and hotbands. This includes typically not more than four quanta in the bends (roughly 2100 cm^{-1} total) in conjunction with one or two quanta of the CC stretch. The CH stretches, on the other hand, are highly anharmonic and provide detectable overtone transitions that can reach as high as eight quanta in the CH stretch motion, or 24,000 cm^{-1} [1]. Although the CH overtone work reaches very high energy levels, the CH stretches do not couple as extensively to other levels as one might think due to the large dynamical separation bewteen the CH stretches, CC stretch and bending vibrations, i.e. the large frequency separations between these modes does not allow very many low order (low quantum number change) resonances with small energy denominators (small energy differences between interacting states), see Table 3.1.

If the first excited singlet electronic state, the $\widetilde{A}$ state, of acetylene is used as an intermediate in, for example stimulated emission pumping (SEP) or dispersed fluorescence (DF) experiments, the *trans*-bent and CC double bonded geometry of the $\widetilde{A}$ state compared to the linear, CC triple bonded ground state allows Franck-Condon (FC) access to levels in the $\widetilde{X}$ state that have excitation in very high quanta in the *trans*-bend and moderate quanta in the CC stretch. Many studies in this research group and others have focused on these Franck-Condon allowed bright states to further elucidate the dynamics of the ground state acetylene. During my tenure here I have tried to open up the possibility of additional intermediate vibrational levels in the $\widetilde{A}$ state that would allow access to other $\widetilde{X}$ state vibrational levels than the traditional *trans*-bend and CC stretch combinations, in particular, to take maximum advantage of some of the DF analysis (unzipping) techniques developed by myself and Jon O'Brien and discussed later in this thesis.

To understand why some "non-traditional" $\widetilde{A}$ state intermediate levels would be useful, it is instructive to understand the following simplified version of the resonance pathways discovered by the "traditional" SEP and DF PUMP intermediates. Taking advantage of the Franck-Condon factors and the thermally populated levels of the ground state, traditional PUMP preparations access the zero point, $2\nu_3'$ or $3\nu_3'$ (two and three quanta of the $\widetilde{A}$ state *trans*-bend [6], respectively) levels of the $\widetilde{A}$ state. Each of these PUMP intermediates prepares the same zero-order bright states for a DF or SEP experiment, that is, the FC active very high quanta in the *trans*-bend and moderate quanta in the CC stretch. The only difference is in the actual FC envelope, e.g. $2\nu_3'$ would have two nodes in the *trans*-bend wavefunction, *etc.*

A much simplified version of the resonances seen in the SEP experiments is shown in Figure 3.1. Traditional intermediate vibrational levels used in acetylene SEP and DF have Peak A as their zero-order bright state. This allows levels connected by ground state resonances (such as the Darling-Dennison bend or "2345" resonance) to be illuminated, shown here pictorially as Peaks B and C. The next set of resonances would connect Peaks D and E to the A/B/C set, but they are too weak to be observed with Peak A as

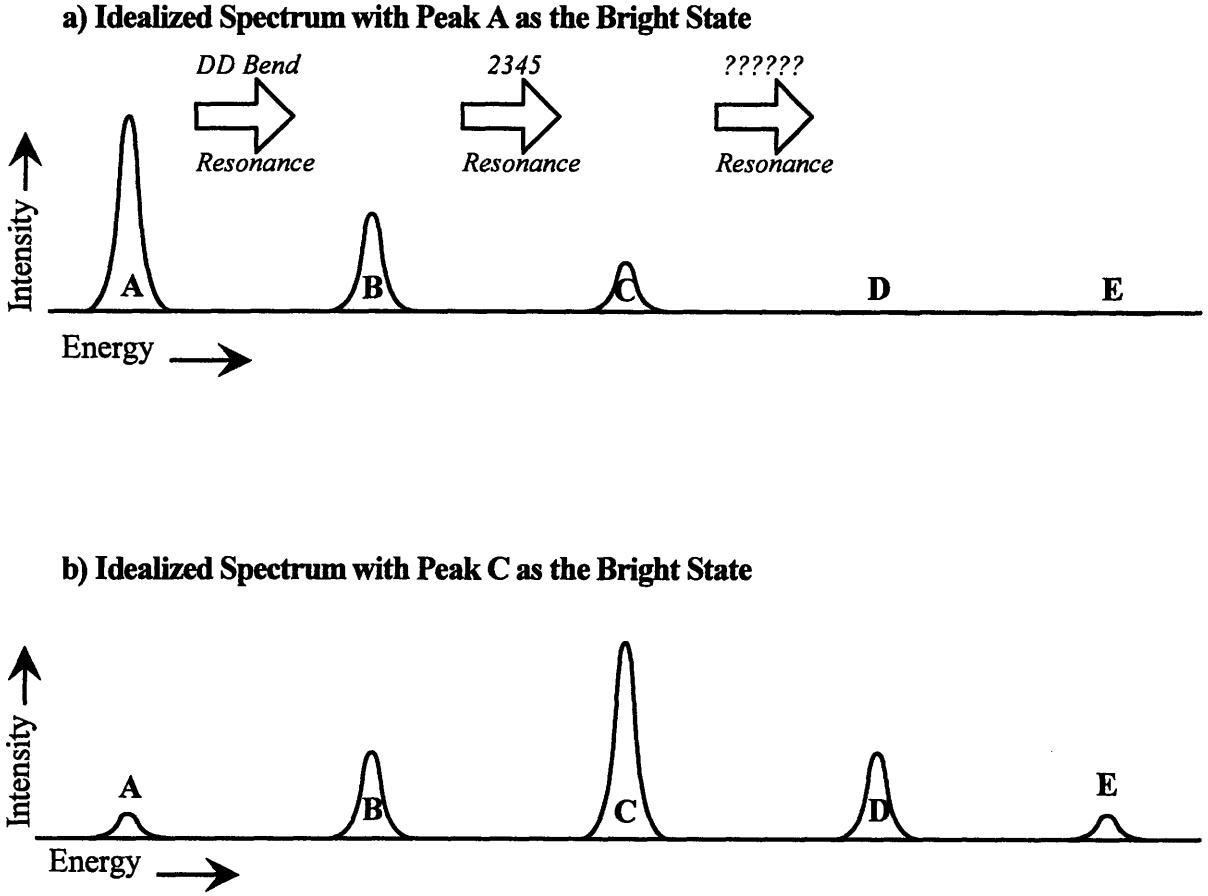

Figure 3.1: Traditional intermediates used in acetylene SEP and DF have Peak A as their zero-order bright state. This allows levels connected by ground state resonances (such as the Darling-Dennison bend or "2345" resonance) to be illuminated, shown here pictorially as Peak B and Peak C. The next set of resonances would connect Peaks D and E, but they are too weak to be observed with Peak A as the Bright State. Choosing an intermediate vibrational level in the $\tilde{A}$ state that has Peak C as the Bright State would then allow Peaks D and E to be observed and analyzed.

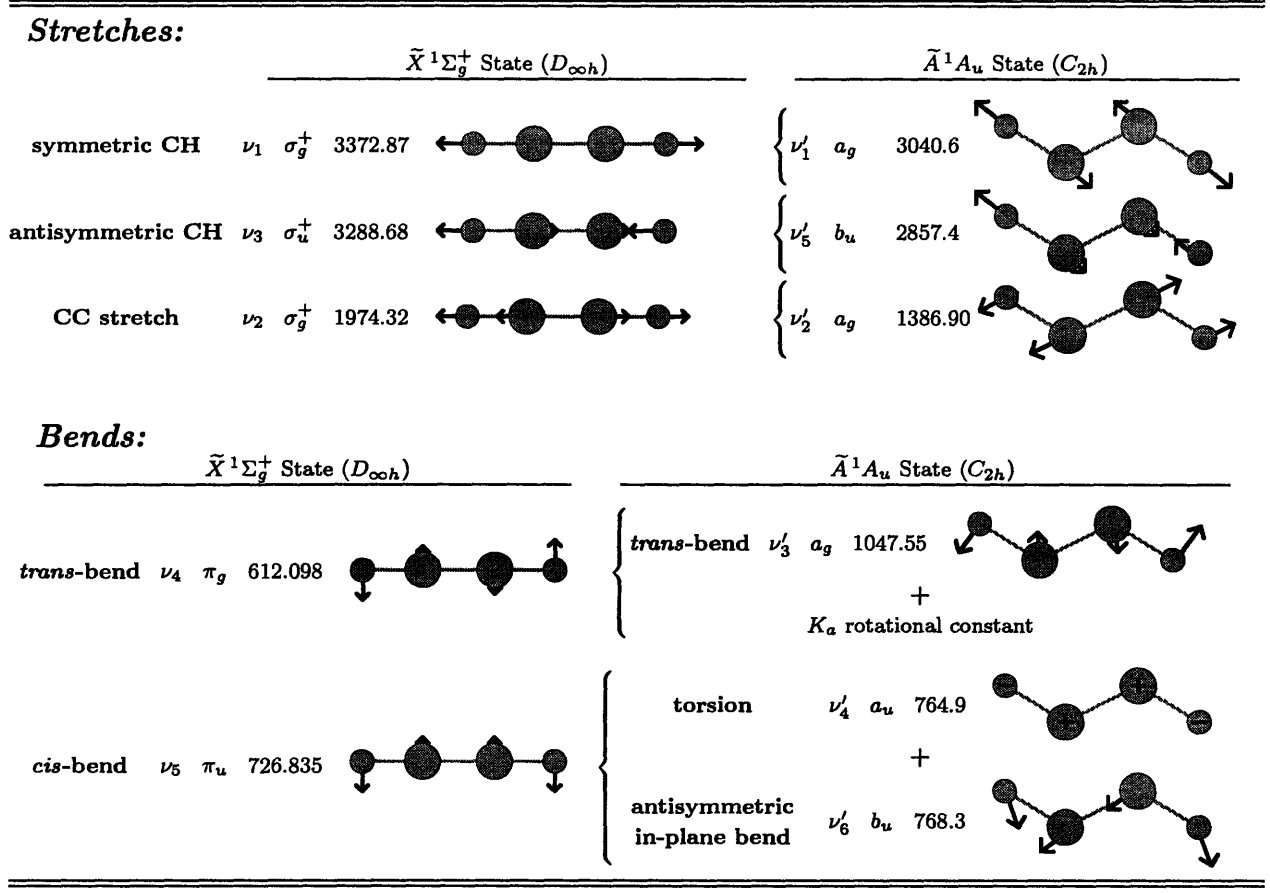

Table 3.1: The normal modes (seven vibrational degrees of freedom) for the $\widetilde{X}$ state of acetylene and their correlations to the modes (six vibrational degrees of freedom + one rotational degree of freedom) for the $\widetilde{A}$ state, including mode numbering, symmetries, frequencies in cm^{-1} ($\nu_i = \omega_i^0 + x_{ii}^0$) and vibrational motions [2–5].

the bright state. On the other hand, if Peak C is selected as the Bright State, Peaks D and E would be readily observable and the elucidation of their resonance mechanism could be accomplished. Pictorially, this is equivalent to shining a flashlight at a complicated maze and thereby being able to map it piece by piece.

3.1 ν_5' as an Alternative $\widetilde{A}$ State Intermediate

An example of a useful alternate bright state would be one that has one quantum in the antisymmetric CH stretch, ν_3. Since the antisymmetric CH stretch is FC vertical, *i.e.* $\Delta v = v_5' - v_3 = 0$, the intermediate vibrational level that must be prepared in the $\widetilde{A}$ state for a DF or SEP experiment must also have one quantum in the antisymmetric CH stretch, ν_5', see Figure 3.2. prepare the ν_5' $\widetilde{A}$ state intermediate, a PUMP transition must be initiated from the $\widetilde{X}$ state vibrational level with one quantum in the antisymmetric CH stretch, ν_3''. Unfortunately, the ν_3'' is not significantly thermally populated thus requiring an additional "prePUMP" laser to move population to the ν_3'' level via the strong IR transition from the $\widetilde{X}$ state zero-point level.

In order to use the ν_5' $\widetilde{A}$ state intermediate in an SEP or DF experiment, the spectroscopy of that level must be known and particular attention must be paid to the possibility of perturbations in that level, since the success of the DF analysis, in particular, depends heavily on knowing the exact vibrational character of the intermediate.

The spectroscopy of ν_5' $\widetilde{A}$ state intermediate vibrational level has been partially analyzed previously by Tobiason and co-workers [7]. In their experiment they populated the $3\nu_3''$ level via a Raman-shifted dye laser followed by a UV excitation to the ν_5' $\widetilde{A}$ state level. In this manner they could use the UV excitation as a sensitive probe in energy transfer experiments of the $3\nu_3''$ level. The $3\nu_3''$ level would not be suitable for our DF or SEP experiments, since not enough population would be transferred ultimately to the $\widetilde{A}$ state to carry out the subsequent DF or SEP steps, since the oscillator strength for the overtone transition would be at least two orders of magnitude weaker than that for the ν_3'' fundamental.

An experiment was carried out with two immediate objectives: 1) determine if enough $\widetilde{A} \rightarrow \widetilde{X}$ UV fluorescence could be generated for a DF or SEP experiment by prePUMPing the ν_3'' fundamental, followed by a UV PUMP to ν_5'; and 2) use the high resolution lasers to carry out a complete spectroscopic study of the $\widetilde{A}$ state ν_5' fundamental to assure the proper characterization of the vibrational character for future DF or SEP experiments.

3.2 Experimental Details

The 532 nm output of a Continuum NY61-20 Nd:YAG laser pumped a Spectra Technologies, Inc., HRL-100 Ti:Sapphire laser to produce tunable near-IR (730-940 nm) radiation. The near-IR light was passed through a custom built Raman-shifter [8] specifically designed by Jody Klaassen to produce high output powers of the 2nd Stokes (H_2) radiation. Typical output powers of the 2nd Stokes were 0.75-2.0 mJ of radiation at 3.3 μm. The Stokes and anti-Stokes frequencies were separated with a simple 60° prism. The 3.3 μm light was then passed through one of two matched static gas cells each containing 25-50 mTorr of acetylene (Matheson purified grade, further purified by several liquid nitrogen freeze, evacuate, and thaw cycles and sublimed into the cell at thermal equilibrium with a pentane slush).

A small part of the 3.3 μm IR beam was diverted through another static gas cell equipped with a microphone. The acoustic signal from the ν'' fundamental vibrational transition could be monitored and the Ti:Sapphire could then be locked on a single rovibrational transition of this strong acetylene IR fundamental.

A Lambda Physik LPX210icc excimer pumped a Lambda Physik 2002EC (with extracavity etalon removed) dye laser with an internal cavity etalon, resolution=0.05 cm^{-1}. The Coumarin 480 nm output of the dye laser was frequency doubled in β-BBO (CSK crystals) producing tunable UV radiation around 240 nm. The dye laser was pressure scanned with $0-1.5$ atm of SF_6 to produce UV frequency scans roughly 30 cm^{-1} in length calibrated by the Te_2 absorption of a small portion of the blue fundamental [9]. The fundamental and second harmonic laser beams were separated by 60° S1UV fused silica prisms, and a second 60° prism

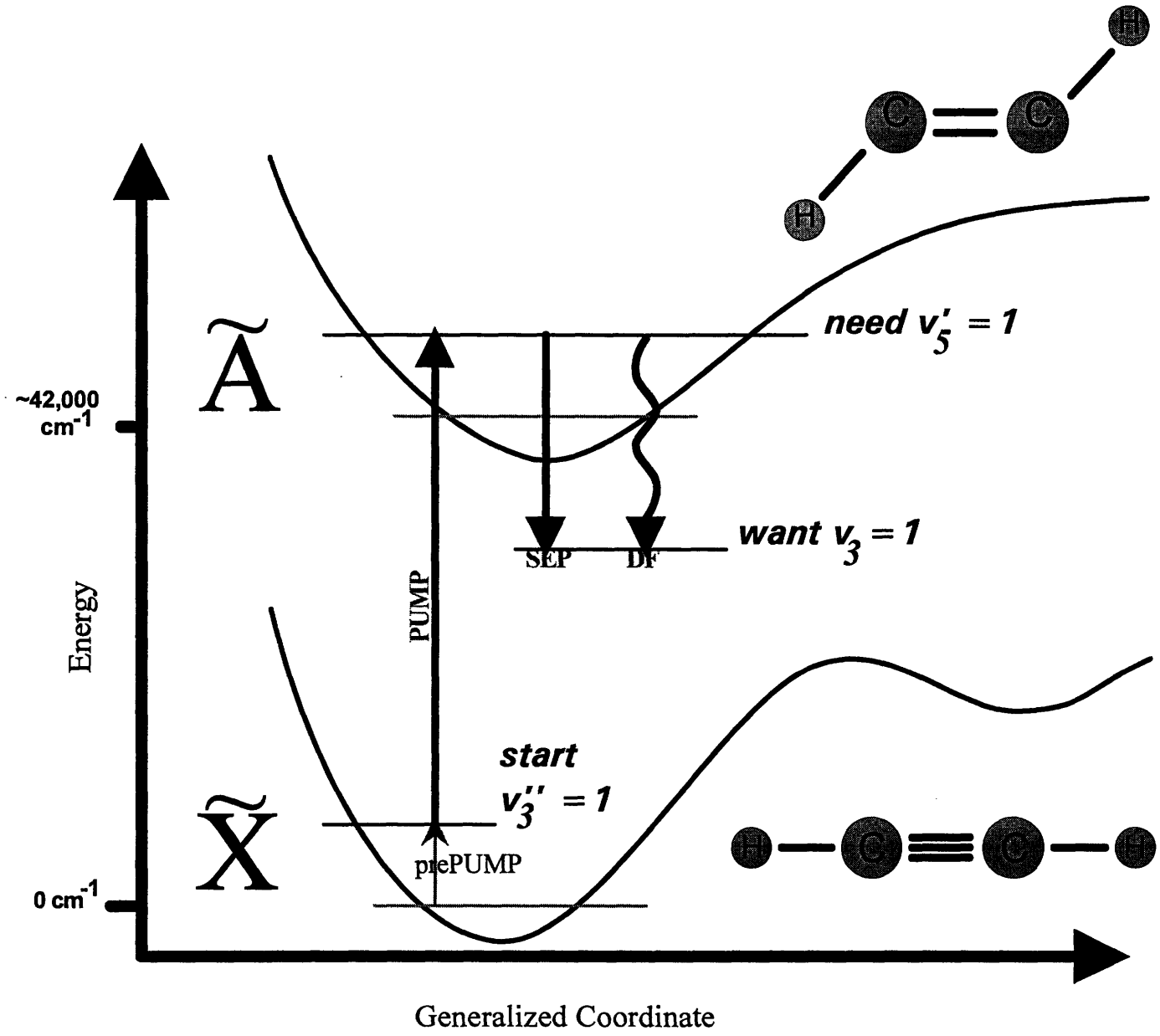

Figure 3.2: To have FC access to $\widetilde{X}$ state vibrational levels with one quantum in the antisymmetric CH stretch, ν_3, an $\widetilde{A}$ state intermediate also with one quantum in the antisymmetric CH stretch, ν_5', must be prepared via a PUMP laser which then must originate from the $\widetilde{X}$ state level with one quantum in the antisymmetric CH stretch, ν_3''. Since the ν_3'' level does not have significant thermal population, molecules must be moved there via a prePUMP IR transition.

compensated for the first prism in such a way that the second harmonic emerged travelling parallel to its initial direction. This arrangement minimized beam walk as the laser frequencies were tuned. The doubled UV laser beam was split by a 240 nm 50% beamsplitter, so that about 50 μJ of light entered the identical signal and reference static gas cells.

The UV laser beam through the signal cell was counter-propagated along the IR laser beam path. When the UV laser frequency was coincident with an $\widetilde{A} \leftarrow \widetilde{X}$ transition from the J'', ν_3'' level in the $\widetilde{X}$ state to an allowed rovibrational level in the $\widetilde{A}$ state, spontaneous side fluorescence from the subsequent $\widetilde{A} \rightarrow \widetilde{X}$ transition could be monitored. If, on the other hand, the UV laser beam excited an $\widetilde{A} \leftarrow \widetilde{X}$ transition from a thermally populated ground state level, then side fluorescence would be emitted in both the signal and reference cells. In this manner spurious hot band transitions could be eliminated, although none were noticed in this IRUV region.

The side fluorescence was imaged by S1UV f/1.9 collection optics onto matched photomultipliers (Hamamatsu R331). Schott BG1, BG3, BG25, UG1 or UG5 filters were used to eliminate scattered UV light from the doubled laser beam. The outputs of the photomultipliers were amplified by LeCroy VV100BTB amplifiers, and fed into a home-built differential amplifier consisting of an Intersil 733 differential video amplifier and an OEI 9911 high current linear voltage follower (50Ω line driver). The output of the line driver was connected to a SRS 250 boxcar which was connected to a National Instruments DT2801 A/D converter in an IBM PC, where the acetylene side fluorescence intensity could be monitored as a function of UV PUMP wavelength.

3.3 Analysis

Approximately 200 cm^{-1} were scanned around 45,000 cm^{-1} (2,900 cm^{-1} relative to the $\widetilde{A}$ state zero-point level), including $J' = 0-10$ of three observed vibrational bands (ν_5', $2\nu_3' + \nu_4'$ and $2\nu_3' + \nu_6'$) with $K_a' = 0-2$. By altering the relative polarizations of the UV and IR laser beams the Q versus P/R rotational transitions could be distinguished by the well known laser polarization effects discussed previously in the axis-switching chapter. This in conjunction with term value coincidences allowed complete and definitive determination of the J' and K_a' quatum numbers for the observed levels. A term value plot is shown in Figure 3.3. A future paper will discuss the spectroscopic fits, perturbation mechanisms and vibrational character of the observed levels.

The intensity of the fluorescence observed was substantial and encouraging for future DF experiments. Even though a second laser system was required to move population up to the $\widetilde{A}$ state vibrational level, the fluorescence intensity was indeed larger than that observed from the $\widetilde{A} \leftarrow \widetilde{X}$ Origin Band (zero-point $\widetilde{X}$ state to zero-point $\widetilde{A}$ state) transition from which we have recorded a DF spectrum.

3.4 Other Alternate $\widetilde{A}$ State Intermediate Levels

Other $\widetilde{A}$ state vibrational levels that would be useful include one quantum of symmetric CH stretch. Preliminary experiments were carried out to prePUMP using the strong Raman ν_1'' fundamental from which a UV transition to ν_1' could be executed. This experiment is also spectroscopically interesting since the ν_1' $\widetilde{A}$ state fundamental has never successfully been observed. At this writing this experiment has not been finished.

References

[1] B. C. Smith, J. S. Winn. *J.Chem.Phys.* **94**(6), 4120 (1991).

[2] G. Herzberg. *Molecular Spectra and Molecular Structure, Volume II - Infrared and Raman Spectra of Polyatomic Molecules.* Krieger Publishing Company, Malabar, FL (1991).

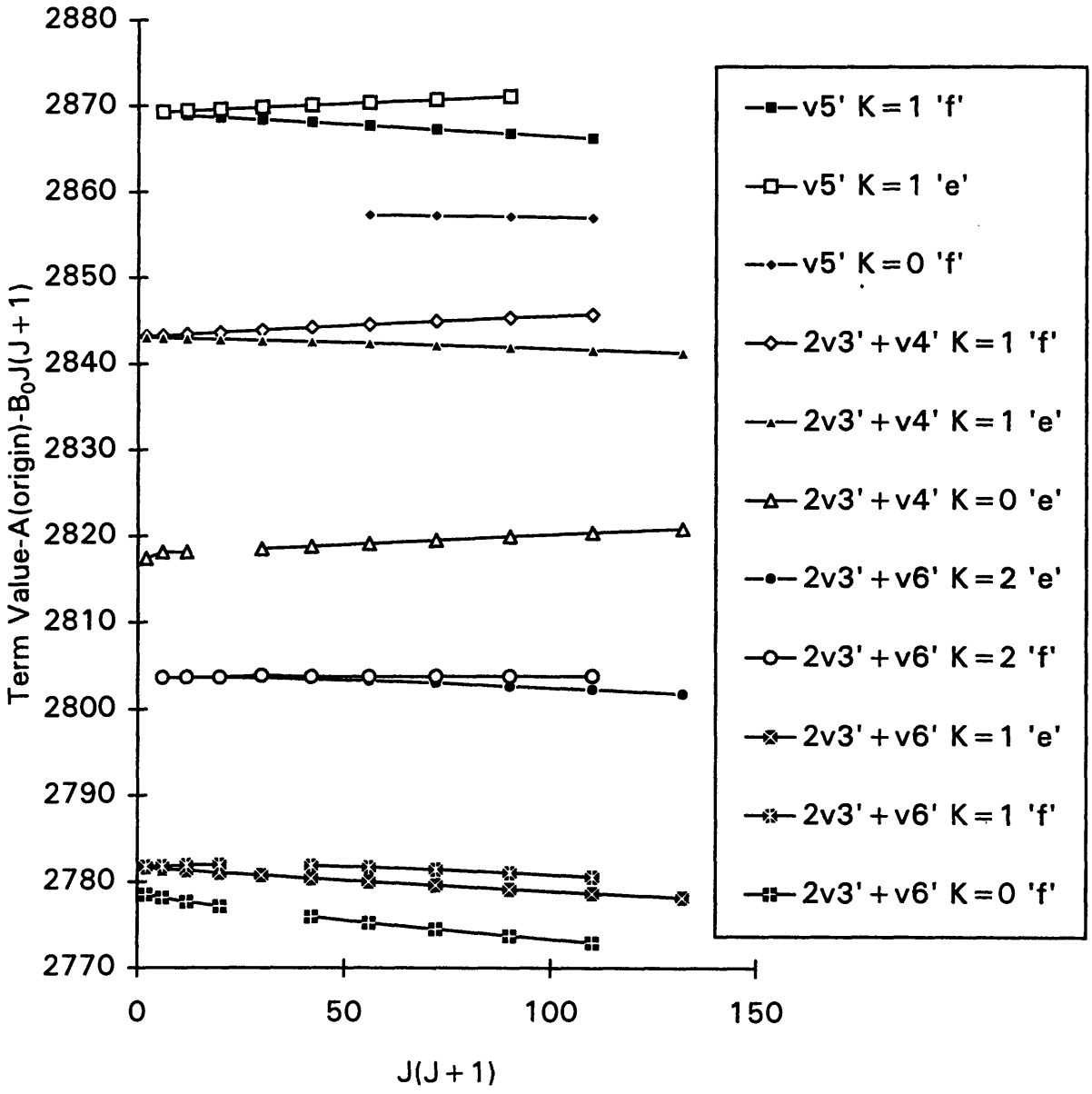

Figure 3.3: A partial reduced term value plot shows some of the observed rovibrational levels of the ν_5', $2\nu_3' + \nu_4'$ and $2\nu_3' + \nu_6'$ $\widetilde{A}$ state vibrational levels with $K_a' = 0 - 2$.

[3] G. Herzberg. *Molecular Spectra and Molecular Structure, Volume III - Electronic Spectra and Electronic Structure of Polyatomic Molecules.* Krieger Publishing Company, Malabar, FL (1991).

[4] D. M. Jonas, S. A. B. Solina, B. Rajaram, R. J. Silbey, R. W. Field, K. Yamanouchi, S. Tsuchiya. *J.Chem.Phys.* **99**(10), 7350 (1993).

[5] J. D. Tobiason, A. L. Utz, E. L. Sibert III, F. F. Crim. *J.Chem.Phys.* **99**(8), 5762 (1993).

[6] In the $\widetilde{A}$ state the *trans*-bend is ν_3', whereas in the $\widetilde{X}$ state the *trans*-bend is ν_4.

[7] J. D. Tobiason, A. L. Utz, F. F. Crim. *J.Chem.Phys.* **99**(2), 928 (1993).

[8] J. J. Klaassen. *Energy Transfer Processes in Methane and Trideuteromethane.* Ph.D. thesis, Massachusetts Institute of Technology (1994).

[9] J. Cariou, P. Luc. *Atlas du Spectre d'Absorption de la Molecule de Tellure.* Editions du C.N.R.S., Orsay (1979).

Part II

Dynamics of Acetylene: The DF Experiments

Chapter 4

Dispersed Fluorescence Experimental Setup and Considerations

4.1 Experimental Details

4.1.1 The Origin Band DF Spectrum

The high resolution DF spectra that sample the electronic ground state of acetylene-h_2, $\widetilde{X}\,^1\Sigma_g^+$, were recorded originating from the zero-point level, Origin Band, of the first excited singlet electronic state, $\widetilde{A}\,^1A_u$. The third harmonic of a Lumonics HY 1200 Nd:YAG laser pumped a Lumonics HyperDYE-300 dye laser. The Coumarin 480 output of the dye laser was doubled in a β-BBO crystal to produce 3 mJ of tunable 240 nm radiation which was used to populate the Origin Band $J'_{K_a,K_c} = 1'_{1,1}$ rovibronic level [1]. Matheson Gas Products purified acetylene (99.6% min.), used without further purification at a backing pressure of 1.5 atm, was expanded into vacuum through a 0.8 mm diameter General Valve Series 9 pulsed nozzle at 90° to the excitation laser beam, producing an effective pressure of acetylene in the beam of 350 mTorr. The relative rotational line intensities obtained from a fluorescence excitation (FE) scan were consistent with a rotational temperature of 30K.

The fluorescence was collected in a direction perpendicular to both the laser excitation beam and the jet and focused into a 3/4 meter monochromator(Spex 1700). The monochromator was operated in first and second orders, utilizing a 1200 gr/mm grating blazed at 500 nm, and the dispersed fluorescence was imaged onto a Princeton Instruments intensified CCD (ICCD) Model 576LDG/RB. 6000 laser shots were averaged for each segment. The advantages of using an ICCD are twofold. First, 576 spectral elements are recorded in parallel; *i.e.* a large segment of the spectrum is recorded simultaneously. At each monochromator setting the ICCD covers a spectral width of ~200 Å in first order. Second, and most importantly, frequency and intensity calibration can be carried out directly following each DF scan *without moving the grating*. This arrangement avoids corruption of the wavelength calibration by the stick/slip problems associated with many scanning monochromators.

A complete description of the calibration routine is forthcoming [2]. Briefly, we used thorium, neon and mercury atomic transitions for calibration, and by comparing successive slightly overlapping scans along a series, systematic errors could be compensated for, allowing overall high accuracy and precision. The precision was found to be 1.5 cm^{-1} ($2\bar{\sigma}$) at 7.0 cm^{-1} resolution by comparing peak centers in spectra recorded on separate days. The accuracy was found to be 1–2 cm^{-1} at 7 cm^{-1} resolution by comparing a DF spectrum to higher resolution stimulated emission pumping (SEP) spectra recorded previously with absolute experimental errors of $2\bar{\sigma} = 0.020$ cm^{-1} [3].

Since the fluorescence intensity was the limiting factor in sensitivity, a series of spectra was recorded with entrance slit widths corresponding to resolutions of 10, 12 and 30 cm^{-1} at 355 nm in first order and 7 cm^{-1} for 355 nm photons in second order (grating position at 710 nm). Features with very low intensity in the

higher resolution spectra were easily discernible in the spectra recorded at larger slit widths.

4.1.2 The Preliminary Higher Resolution $2\nu_3'$ DF Spectrum

A preliminary higher resolution $2\nu_3'$ DF spectrum was recorded at M.I.T. A previously recorded $2\nu_3'$ DF spectrum, was recorded by Professor Kaoru Yamanuochi at the University of Tokyo, that had a resolution of roughly 30-50 cm^{-1} with an experimental accuracy of $\pm 50 - 100$ cm^{-1}. The preliminary higher resolution $2\nu_3'$ DF spectrum was recorded at M.I.T. and used to locally recalibrate the older DF spectrum since the calibration accuracy was far superior. Unfortunately the signal to noise of the preliminary higher resolution $2\nu_3'$ DF spectrum was insufficient to allow the use of the spectrum for anything other than recalibration purposes. This band has since been re-recorded by Jon O'Brien with an optimized DF setup and is far superior to anything previously recorded. Further analysis of Jon O'Brien's new spectrum $2\nu_3'$ spectrum will postdate this thesis and promises to provide very interesting results.

The preliminary higher resolution $2\nu_3'$ DF spectrum was recorded as follows. A Lambda Physik LPX210icc excimer laser pumped a Lambda Physik FL2002EC (with the extracavity etalon removed) dye laser. The Coumarin 450 output was doubled in a β-BBO crystal to produce tunable 225 nm light to populate the $2\nu_3'$ $J = 1$, $K_a = 1$, 'f' parity rovibronic level [1]. The side fluorescence from a static gas cell was collected and focused into a 1 meter monochromator(Spex 1802). The monochromator was operated in second order using a 1200 gr/mm grating blazed at 500 nm, and the dispersed fluorescence was imaged onto a Princeton Instruments ICCD Model 1024MG-E. Spectra were recorded with an entrance slit width which corresponds to a resolution of 7 cm^{-1} for 355 nm photons in second order, grating position at 710 nm. The spectrum was calibrated exactly the same as the Origin Band DF spectrum.

4.2 Spectral Purity of the PUMP Transition

Since the PUMP transition in these experiments was the Q(1) rotational line ($J'_{K_a,K_c} = 1'_{1,1} \leftarrow J''_{\ell,\text{parity}} = 1''_{0,e}$) of the origin band, the intermediate level cannot be affected by B-type Coriolis [4] interactions ($\Delta K_a = \pm 1, \Delta K_c = \pm 1$), and there are also no $\Delta K_a = \pm 2$ asymmetric top interactions for this level. Since the closest C-type Coriolis perturber would be the $\nu_3' \cong 1048$ cm^{-1} level with a matrix element on the order of $C_v\sqrt{J(J+1)} \approx 1$ cm^{-1}, an estimate of the maximum contribution of $K_a' = 0$ character would be $\approx 0.0001\%$. The contribution of $K_a' = 0$ character in the intermediate level, which arises from the axis-switching mechanism at $J' = 1$, is on the order of 0.001% [5]. Therefore, with its exceedingly pure $K_a' = 1$ character, the only allowed rovibronic transitions from the selected single rovibronic intermediate level terminate on $\widetilde{X}$-state rotational levels with $J_{\ell,\text{parity}} = 1_{0,e}$ or $2_{2,f}$.

Since we use a normal mode product basis set, the $\widetilde{X}$-state Coriolis coupling is minimized. In a worst case, the proportion of admixed $\ell = 1$ fractional character would be roughly $\approx v_{stretch}v_{bend} * 10^{-5}$ [6]. The DF spectrum of acetylene has a smaller sensitivity range (~100:1) than the SEP spectrum of acetylene (~1000:1) [7]. Indeed, the fluorescence intensity from the particular intermediate state we have selected here was at least three orders of magnitude weaker than that from the more Franck-Condon allowed $2\nu_3'$ or $3\nu_3'$ intermediate levels excited under comparable conditions. Therefore, we do not anticipate significant contributions in the Origin Band DF spectrum from levels with $\ell = 1$.

Furthermore, the only rotational structure in our DF spectra will be collapsed into a single feature. This can be seen from the modified Dunham expression [3],

$$T_{vr} = G_v + F_r, \tag{4.1}$$

where

$$G_v = G_v(v_1, v_2, v_3, v_4^{\ell_4}, v_5^{\ell_5}; J_{\ell,\text{parity}}) = \sum_{i=1}^{5} \omega_i^0 v_i + \sum_{i=1}^{5}\sum_{j=i}^{5} x_{ij}^0 v_i v_j + \sum_{t=4}^{5}\sum_{t'=t}^{5} g_{tt'}^0 \ell_t \ell_{t'} + \sum_{t=4}^{5}\sum_{t'=t}^{5}\sum_{t''=t'}^{5} y_{tt't''} v_t v_{t'} v_{t''} + \sum_{i=1}^{5}\sum_{t=4}^{5}\sum_{t'=t}^{5} y_i^{tt'} v_i \ell_t \ell_{t'} + \cdots - B_v \ell^2 \quad (4.2)$$

$$F_r = F_r(v_1, v_2, v_3, v_4^{\ell_4}, v_5^{\ell_5}; J_{\ell,\text{parity}}) = B_v J(J+1) + \ldots \quad (4.3)$$

and

$$B_v = B_0 - \sum_{i=1}^{5} \alpha_i^0 v_i + \sum_{t=4}^{5}\sum_{t'=t}^{5} (\gamma_{tt'} v_t v_{t'} + \gamma_\ell^{tt'} \ell_t \ell_{t'}) + \ldots \quad (4.4)$$

For the $1_{0,e}$ and $2_{2,f}$ pairs of rotational levels with the same $\mathbb{V} = (v_1, v_2, v_3, v_4, v_5)$ and $\ell_4 = 0$ or $\ell_5 = 0$, $T_{vr}(\mathbb{V}; 1_{0,e}) \cong T_{vr}(\mathbb{V}; 2_{2,f})$ since

$$F_r(\mathbb{V}; 1_{0,e}) - F_r(\mathbb{V}; 2_{2,f}) = B_v(1)(2) - B_v(2)(3) + \ldots \approx -4B_v \quad (4.5)$$

and

$$G_v(\mathbb{V}; 1_{0,e}) - G_v(\mathbb{V}; 2_{2,f}) = \cdots - B_v(0)^2 + B_v(2)^2 \approx 4B_v. \quad (4.6)$$

This rotational simplicity, combined with the accurate frequency calibration and meaningful relative intensities, should make this data set of substantial interest to theoreticians. Although SEP has a much higher resolution and allows simplified rotational assignments (since it is a double resonance technique), SEP's relative intensities are often inaccurate due to saturation effects [7]. Hence, theoretical analysis requiring moderate resolution and meaningful relative intensities benefits from the use of high resolution DF spectra.

References

[1] J. K. G. Watson, M. Herman, J. C. Van Craen, R. Colin. *J.Mol.Spectros.* **95**(1), 101 (1982).

[2] R. J. Bouwens, J. A. Hammerschmidt, M. M. Grzeskowiak, T. A. Stegink, P. M. Yorba, W. F. Polik. "Pure Vibrational Spectroscopy of S_0 Formaldehyde by Dispersed Fluorescence Spectroscopy." *J.Chem.Phys. in press.*

[3] D. M. Jonas, S. A. B. Solina, B. Rajaram, R. J. Silbey, R. W. Field, K. Yamanouchi, S. Tsuchiya. *J.Chem.Phys.* **99**(10), 7350 (1993).

[4] H. L. Dai, C. L. Korpa, J. L. Kinsey, R. W. Field. *J.Chem.Phys.* **82**(4), 1688 (1985).

[5] J. T. Hougen, J. K. G. Watson. *Can.J.Phys.* **43**, 298 (February 1965).

[6] D. M. Jonas. *Spectroscopy of Vibrationally Hot Molecules: Hydrogen Cyanide and Acetylene.* Ph.D. thesis, Massachusetts Institute of Technology (1992).

[7] D. M. Jonas, S. A. B. Solina, B. Rajaram, R. J. Silbey, R. W. Field, K. Yamanouchi, S. Tsuchiya. *J.Chem.Phys.* **97**(4), 2813 (1992).

Chapter 5

Dynamics Below 10,000 cm^{-1}

Controlling a reaction using laser radiation, a form of bond specific chemistry, has long been a goal of physical chemists. Developing a control strategy is predicated on developing an understanding of where and how fast energy flows in a molecule as a function of initial preparation. For reactions of an isolated molecule that occur on a single potential energy surface, this entails characterization of the important pathways of intramolecular vibrational redistribution(IVR).

Describing a system in a zero-order basis (*e.g.* uncoupled harmonic oscillator product states) that accurately depicts the initial state prepared by the laser enables elucidation of the dominant IVR pathways. These pathways are equivalent to the anharmonic resonances described by matrix elements evaluated in the harmonic oscillator product zero-order basis. Although high-resolution, frequency-domain spectroscopy is often naively thought of as only determining "static" information, such as equilibrium molecular structure, spectroscopy can also generate a complete, compact, and intuitive description of complex dynamical processes, such as IVR, by the elucidation of the subset of resonances most important to the dynamics. This compact, intuitive description is an effective Hamiltonian model.

In this chapter we will present only the analysis of the states at $E_{vib} < 10,000$ cm^{-1} in our new high resolution $\widetilde{A} \rightarrow \widetilde{X}$ Origin Band dispersed fluorescence (DF) spectrum of acetylene, Fig. 5.1. The improved frequency resolution, compared to previous DF spectra, and meaningful relative intensities, compared to those in SEP spectra, allow this new Origin Band DF spectrum to be of great use in developing an effective Hamiltonian model and in elucidating the initial energy flow pathways responsible for IVR.

5.1 The Effective Hamiltonian Model and DF Spectra

5.1.1 Utilizing the Appropriate Data Set

Previous acetylene $\widetilde{A} \rightarrow \widetilde{X}$ DF [1] and SEP [2] experiments have led to a description of the earliest time dynamics that results when energy is initially localized in very high excitation of the *trans*-bend and moderate excitation in the CC stretch (the Franck-Condon active modes). Our new higher resolution Origin Band DF spectrum recorded from the zero-point level of the $\widetilde{A}$-state, see Fig. 5.1, allows us to elaborate a more complete picture of the energy flow pathways on the acetylene $\widetilde{X}$-state potential surface. The new DF spectrum has a Franck-Condon (FC) envelope, $5,000 \leq E_{vib} \leq 20,000$ cm^{-1}, that extends to lower $\widetilde{X}$-state energy than the previous $2\nu_3'$ and $3\nu_3'$ DF spectra, see Fig. 5.2, allowing a comparison of the DF data to an effective Hamiltonian model that was initially developed for the high resolution SEP studies in the E_{vib}=7,000 cm^{-1} region [2]. Also, since the intermediate level used to record this new DF spectrum is the zero-point level of the $\widetilde{A}$-state, there are *no nodes* in the $\widetilde{A}$-state vibrational wavefunction, in contrast to the previous $2\nu_3'$ and $3\nu_3'$ DF spectra. Therefore features that were absent in the previous studies, especially at lower energy in the $\widetilde{X}$-state have been recovered, see Fig. 5.3, such as the $[0, 12]$ and $[1, 15]$ polyads in the $2\nu_3'$ DF spectrum (due to a node in the $\widetilde{A}$-state that corresponds to 12 quanta in the *trans*-bend). The

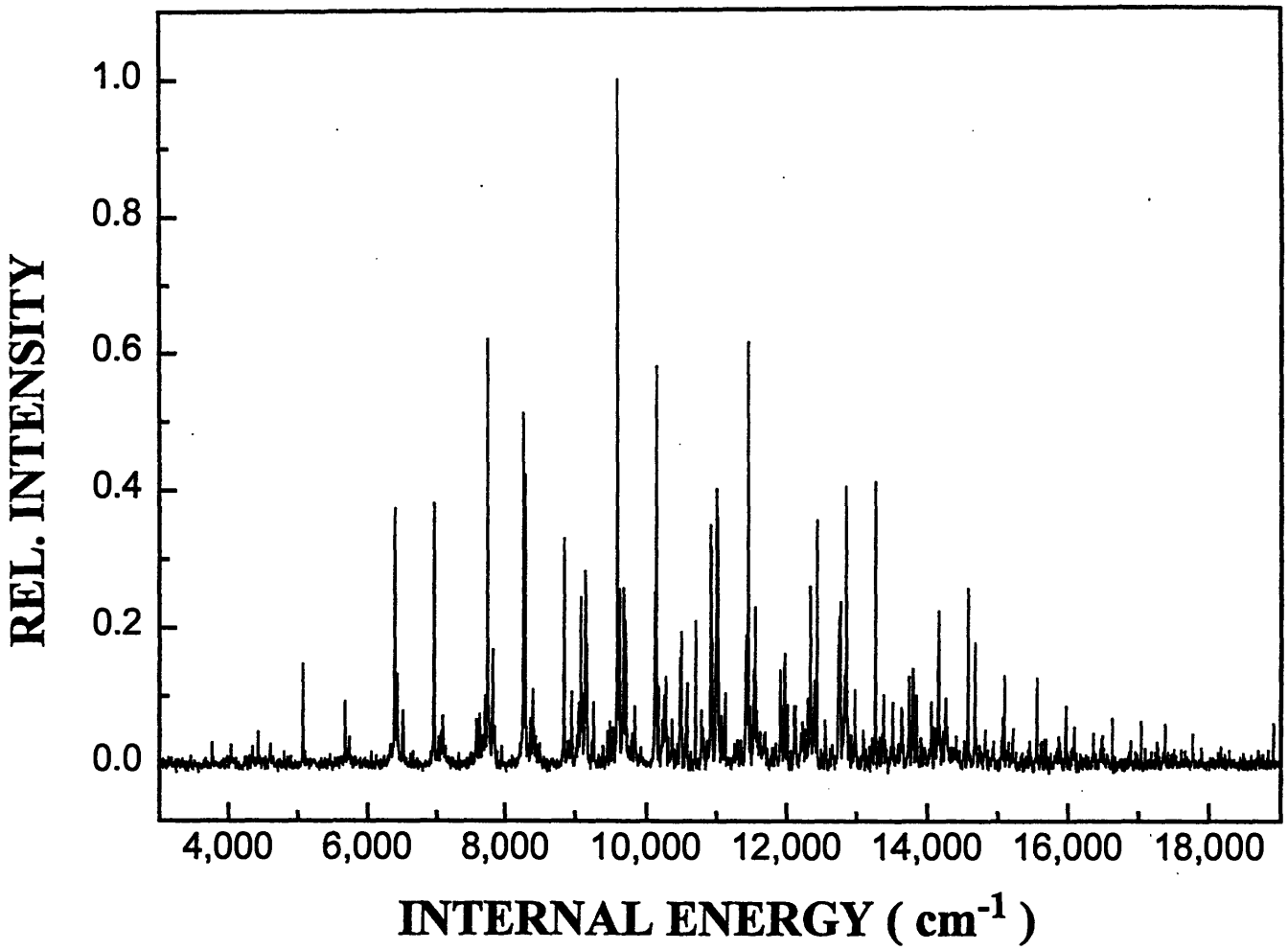

Figure 5.1: High resolution $\widetilde{A}\,^1A_u \rightarrow \widetilde{X}\,^1\Sigma_g^+$ dispersed fluorescence (DF) spectrum, of the ground state, $\widetilde{X}$-state, of acetylene-h_2 recorded from the zero-point level (Origin Band) of the $\widetilde{A}$-state.

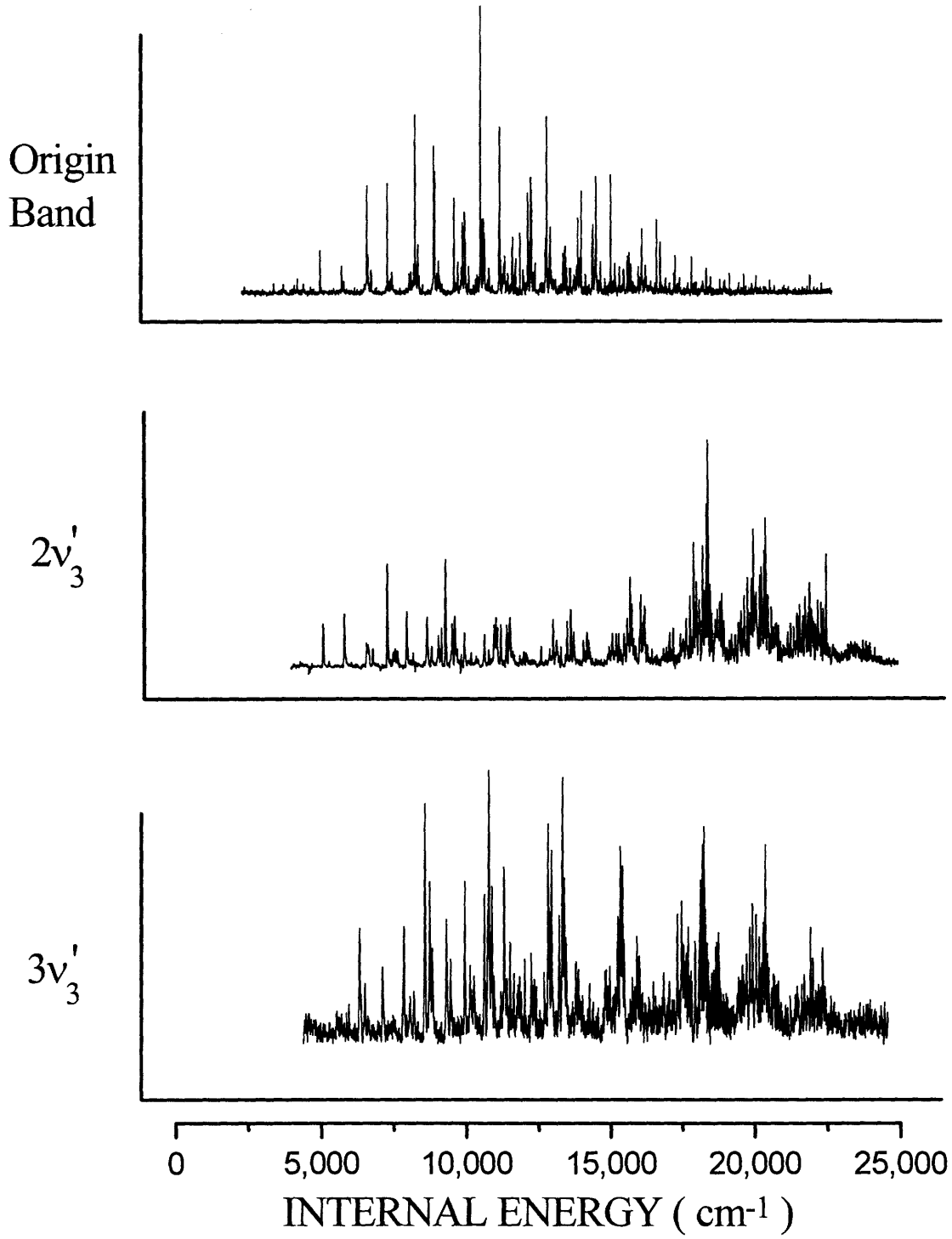

Figure 5.2: The Franck-Condon (FC) envelope of the Origin Band DF spectrum extends to lower $\tilde{X}$-state energies than the previously recorded $2\nu_3'$ and $3\nu_3'$ DF spectra [1].

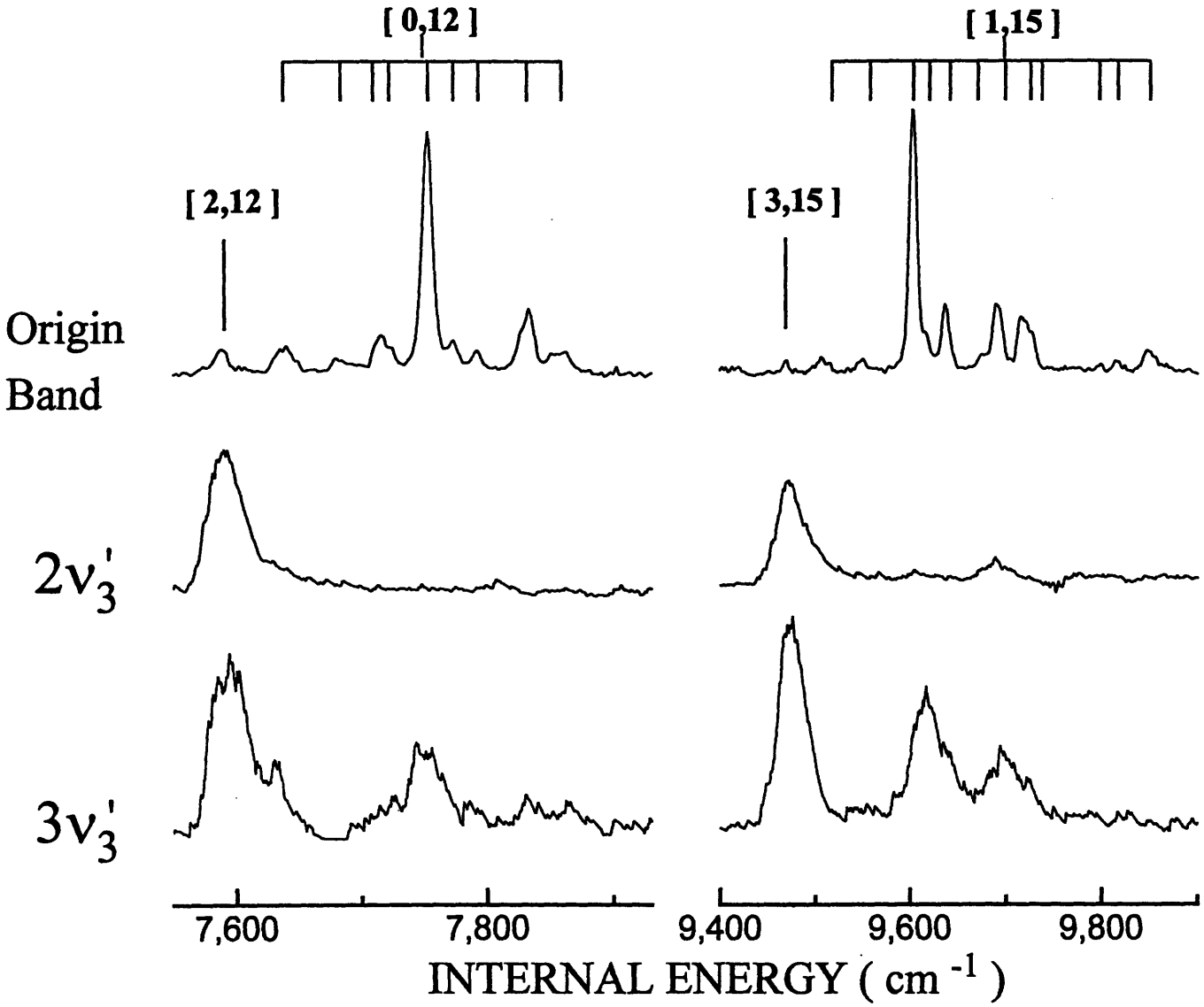

Figure 5.3: A comparison of the new Origin Band DF spectrum to the previous $2\nu_3'$ and $3\nu_3'$ DF spectra [1] shows that features, such as the $[0, 12]$ and $[1, 15]$ polyads which are missing in the $2\nu_3'$ DF spectrum, are recovered in the Origin Band DF spectrum.

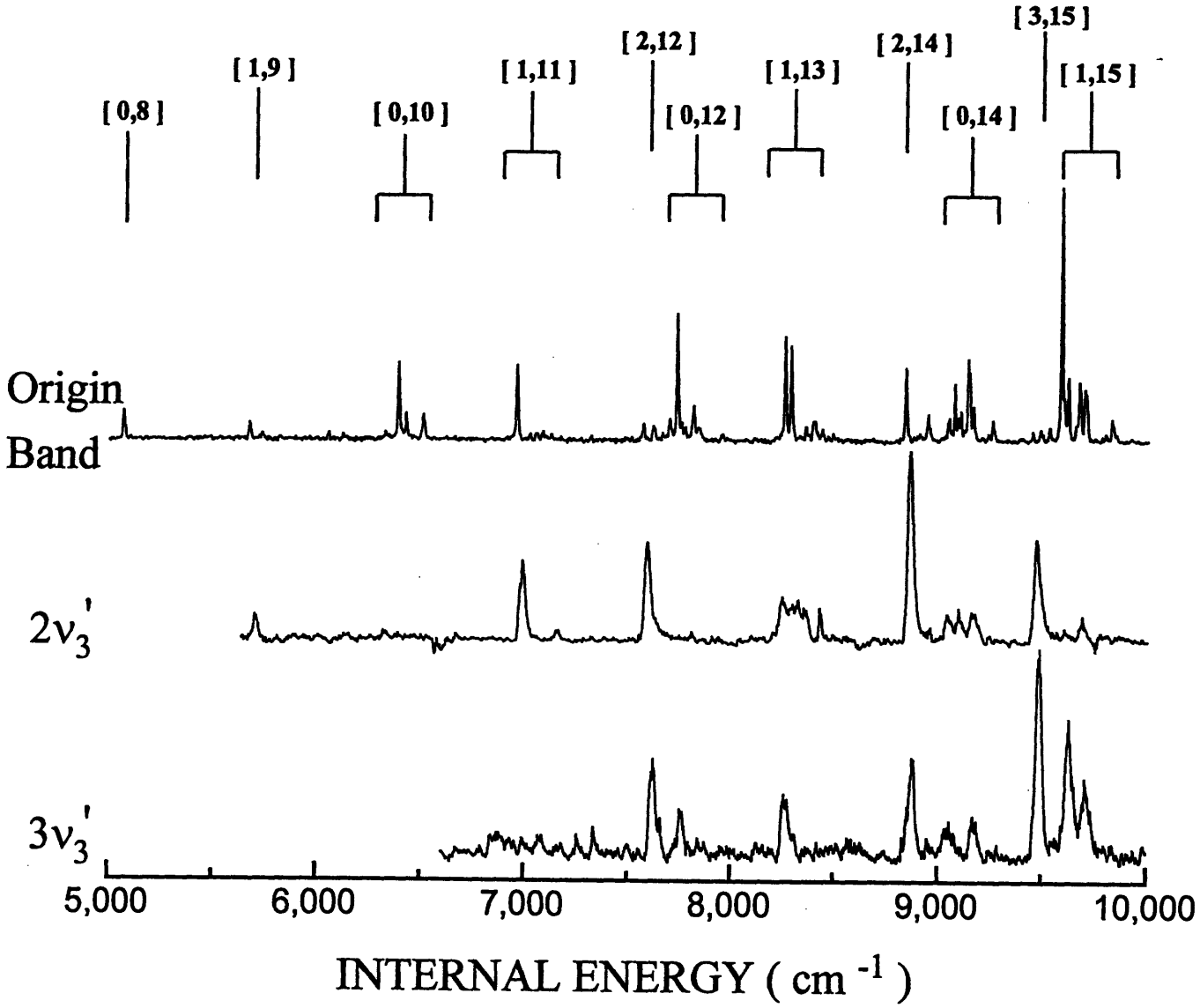

Figure 5.4: The new Origin Band DF spectrum is recorded at sufficiently increased resolution relative to the previous $2\nu_3'$ and $3\nu_3'$ DF spectra [1] that fractionation can be discerned at lower $\tilde{X}$-state energies.

ω_1^0	3398:74[a]	x_{34}^0	-6.96[a]	y_{444}	0.0062[b]
ω_2^0	1981.71[a]	x_{35}^0	-8.69[a]	y_{445}	-0.0379[b]
ω_3^0	3316.09[a]	x_{44}^0	3.082[b]	y_{455}	0.1576[b]
ω_4^0	609.016[b]	x_{45}^0	-2.406[b]	y_{555}	0.0141[b]
ω_5^0	729.170[b]	x_{55}^0	-2.335[b]		
		g_{44}^0	0.759[b]	B_0	1.176608[c]
x_{11}^0	-26.57[a]	g_{45}^0	6.541[b]	α_1^0	0.00686[c]
x_{12}^0	-12.62[a]	g_{55}^0	3.490[b]	α_2^0	0.00621[c]
x_{13}^0	-105.09[a]			α_3^0	0.00560[c]
x_{14}^0	-15.58[a]	y_4^{44}	0.0083[b]	α_4^0	-0.00129[c]
x_{15}^0	-10.85[a]	y_4^{45}	0.0114[b]	α_5^0	-0.00215[c]
x_{22}^0	-7.39[a]	y_4^{55}	-0.0632[b]	γ_{44}	0.0000010[b]
x_{23}^0	-6.10[a]	y_5^{44}	0.0639[b]	γ_{45}	-0.0000236[b]
x_{24}^0	-12.48[a]	y_5^{45}	0.0518[b]	γ_{55}	0.0000167[b]
x_{25}^0	-1.57[a]	y_5^{55}	-0.0070[b]	γ_ℓ^{44}	-0.0000710[b]
x_{33}^0	-27.41[a]			γ_ℓ^{45}	-0.0002255[b]
				γ_ℓ^{55}	-0.0001125[b]

[a]See [2]
[b]See [5]
[c]See [6]

Table 5.1: Molecular constants (in cm^{-1}) for acetylene-h_2.

most important advantage of this new DF spectrum is that the increase in resolution is sufficient to discern fractionation [3] at lower $\widetilde{X}$-state energies, see Fig. 5.4, where the initial IVR should be describable by our effective Hamiltonian model.

5.1.2 The $\hat{H}_{eff}^{\mathcal{R}}$ Effective Hamiltonian and Separation of Polyads

Our effective Hamiltonian, $\hat{\mathbf{H}}_{eff}^{\mathrm{R}}$, is expressed in terms of a normal mode product basis set, where the zero-order states, see Table 5.1, are coupled by harmonic oscillator matrix elements associated with the set of all resonances [4], $\mathcal{R}_{C_2H_2}$, found in the previous IR, Raman and CH overtone spectra, as well as the SEP study, see Table 5.2.

Each resonance is characterized by a selection rule (which defines a group of strongly coupled zero-order levels) and a scalable harmonic oscillator matrix element. The resonances may be summarized as follows:

$$\mathcal{R}_{C_2H_2} = \mathcal{B}_{C_2H_2} \cup \mathcal{X}_{C_2H_2} \cup \mathcal{S}_{C_2H_2} \tag{5.1}$$

where

$$\textit{Bend-Only Resonances} : \mathcal{B}_{C_2H_2} = \{\text{DD Bend I, DD Bend II,vib-}\ell\text{-res}\} \tag{5.2}$$

$$\textit{Bend-Stretch Resonances} : \mathcal{X}_{C_2H_2} = \{\text{“3,245”, “1,244”, “1,255”, “14,35”}\} \tag{5.3}$$

$$\textit{Stretch-Only Resonances} : \mathcal{S}_{C_2H_2} = \{\text{DD Stretch}\}. \tag{5.4}$$

By inspection of the set of all known [4] resonances, $\mathcal{R}_{C_2H_2}$, listed in Table 5.2, or by simple linear algebra [2, 11–13], it can be shown that out of the *seven* zero-order vibrational quantum numbers, there remains a

$\mathcal{R}_{C_2H_2}$: the Anharmonic Resonances used in $\hat{H}^R_{eff}$ [a], $H_{ij} = \langle v_i^{\ell_i} \vert \hat{H}^R_{eff} \vert (v_i + \Delta v_i)^{(\ell_i + \Delta \ell_i)} \rangle$		Scaling Matrix Element [b], H_{ij}, **in the signed-ℓ-basis**
$\mathcal{B}_{C_2H_2}$: ***Bend-only interactions***		
DD bend res. I	$\Delta v_5 = -\Delta v_4 = 2$	$\frac{1}{4} s_{45} \sqrt{(v_4 - l_4)^2 (v_5 - l_5 + 2)^2}$
DD bend res. II	$\Delta v_5 = -\Delta v_4 = 2$, $\Delta \ell_4 = -\Delta \ell_5 = \mp 2$	$\frac{1}{16} d^{eff}_{45} \sqrt{(v_4 \pm \ell_4 - 2)(v_4 \pm \ell_4)(v_5 \pm \ell_5 + 2)(v_5 \pm \ell_5 + 4)}$
vibrational-ℓ-res.	$\Delta \ell_4 = -\Delta \ell_5 = \mp 2$	$\frac{1}{4} r^{eff}_{45} \sqrt{(v_4 \pm \ell_4)(v_4 \mp \ell_4 + 2)(v_5 \mp \ell_5)(v_5 \pm \ell_5 + 2)}$
$\mathcal{X}_{C_2H_2}$: ***Stretch-Bend interactions***		
"3,245" res.	$\Delta v_3 = -\Delta v_2 = -\Delta v_4 = -\Delta v_5 = 1$, $\Delta \ell_4 = -\Delta \ell_5 = \pm 1$	$-\frac{1}{8} K_{3,245} \sqrt{(v_2)(v_3 + 1)(v_4 \pm \ell_4)(v_5 \mp \ell_5)}$
"1,244" res.	$\Delta v_1 = -\Delta v_2 = -\frac{1}{2} \Delta v_4 = 1$	$-\frac{1}{4} K_{1,244} \sqrt{(v_1 + 1)(v_2)(v_4^2 - l_4^2)}$
"1,255" res.	$\Delta v_1 = -\Delta v_2 = -\frac{1}{2} \Delta v_5 = 1$	$-\frac{1}{4} K_{1,255} \sqrt{(v_1 + 1)(v_2)(v_5^2 - l_5^2)}$
"14,35" res.	$\Delta v_1 = -\Delta v_3 = \Delta v_4 = -\Delta v_5 = 1$, $\Delta \ell_4 = -\Delta \ell_5 = \pm 1$	$-\frac{1}{8} K_{14,35} \sqrt{(v_1 + 1)(v_3)(v_4 \pm \ell_4 + 2)(v_5 \pm \ell_5)}$
$\mathcal{S}_{C_2H_2}$: ***Stretch-only interactions***		
DD stretch res.	$\Delta v_1 = -\Delta v_3 = 2$	$\frac{1}{4} K_{11,33} \sqrt{(v_1 + 1)(v_1 + 2)(v_3)(v_3 - 1)}$

Reduced coupling constants (in cm^{-1}) for acetylene-h_2

$s_{45} \cong -11.0$ [c]
$r^0_{45} = -6.238$ [e]
$r_{445} = 0.2125$ [e]
$r_{545} = -0.1063$ [e]

$|K_{3,245}| = 18.28$ [d]
$|K_{1,244}| = 6.379$ [f]
$|K_{1,255}| = 6.379$ [f]
$|K_{14,35}| = 29.044$ [f]
$|K_{11,33}| = 105.83$ [d]

where [g]:

$$\begin{aligned} d^{eff}_{45} &= r^{eff}_{45} + 2 g^{eff}_{45} \\ r^{eff}_{45} &= r^0_{45} + \sum_{t=4}^{5} r_{t45} \, (v_t - 1) \\ g^{eff}_{45} &= g^0_{45} + \sum_{i=1}^{5} y^{45}_i v_i \end{aligned}$$

[a] See [2, 7]
[b] See [2, 5, 7–9]
[c] See Section5.2.1.
[d] See [2].
[e] See [5].
[f] See [7].
[g] The index i is over all five vibrations, t is only the bends

Table 5.2: For the standard coupled normal mode Hamiltonian, the complete set of scalable resonances, $\mathcal{R}_{C_2H_2}$, used in the global treatment of the IR, Raman, overtone and SEP data is listed here. *Note: the matrix elements are given in the signed-ℓ-basis.* Since the laser prepares and probes acetylene states with a defined parity, an orthogonal transformation is performed on the signed-ℓ-basis states to transform them to a parity-basis. See [2, 10].

set, $\mathcal{N}_{C_2H_2}$, of *three* conserved quantities or polyad numbers,

$$\mathcal{N}_{C_2H_2} \equiv [N_s, N_{res}]^{\ell}, \text{ where } \begin{cases} N_s = v_1 + v_2 + v_3 \\ N_{res} = 5v_1 + 3v_2 + 5v_3 + v_4 + v_5 \\ \ell = \ell_4 + \ell_5. \end{cases} \tag{5.5}$$

N_s is the total stretch quantum number, ℓ is the total vibrational angular momentum quantum number, and N_{res} is a resonance quantum number arising from the frequency ratios of the normal modes, see Ref. [2]. The conserved polyad numbers mean that the harmonic oscillator product basis set for acetylene is effectively block diagonalized into groups of zero-order states, each labeled by $[N_s, N_{res}]^{\ell}$. Each group of strongly coupled states is called a "polyad". The set of known resonances, Table 5.2, connects the zero-order states *within* each polyad but never *between* polyads. These dynamically conserved polyad numbers (conserved on the timescale, *i.e.* resolution, of the experiment) are in addition to the rigorously conserved symmetries of acetylene that correlate to J, g/u point group inversion, and $+/-$ parity labels. The three polyad numbers plus the J, g/u, and $+/-$ parity labels provide a unique name for each polyad as well as a recipe for automatically setting up individual polyad blocks in an effective Hamiltonian matrix.

In contrast to the linear and CC triple-bonded ground state geometry, acetylene's first excited singlet electronic state, $\widetilde{A}\,^1A_u$, has an equilibrium geometry that is *trans*-bent and has a nominal CC double bond. This results in Franck-Condon (FC) activity in very high excitation of the *trans*-bend, ν_4, and moderate excitation in the CC stretch, ν_2, for spectroscopic schemes that probe the ground state using the $\widetilde{A}$-state as an intermediate such as DF and SEP.

These two particular FC-active modes, ν_2 and ν_4, in combination with the particular set of active resonances, $\mathcal{R}_{C_2H_2}$, lead to a fortuitous coincidence such that there will be **only one FC bright state per polyad**. This can be explained as follows. The symmetric CH stretch (ν_1), the antisymmetric CH stretch (ν_3) and the *cis*-bend(ν_5) are FC-inactive, whereas the CC stretch(ν_2) and the *trans*-bend(ν_4) are FC-active. This defines a set of zero-order bright states, or "chromostates", for SEP or DF spectra as the set of $(v_1, V_2, v_3, V_4, v_5)$'s where v_1, v_3, and v_5 are held constant and V_2 and V_4 are variable [14]. By inspection of the definitions of $[N_s, N_{res}]$, it is impossible to find more than one (V_2, V_4) pair with the same (v_1, v_3, v_5) for a given $[N_s, N_{res}]$. Therefore, there is only one bright state per polyad in the Origin Band DF spectrum *as long as the polyad numbers remain good.* The polyad numbers will be conserved as long as any previously undetected resonance only connects states within and not between polyads.

The pattern formed in the DF spectrum for each polyad is the distribution of the intensity of the zero-order bright state, or chromostate, among the ground state molecular eigenstates. Therefore, the intensity pattern within each polyad is solely a function of the ground state resonances, or dynamics, and the particular choice of chromostate. By comparing two or more DF spectra originating from different intermediate states that prepare the same set of chromostates, but in which the relative intensities of the different chromostates vary from one intermediate state DF spectrum to another, we see that the intensity pattern *within each polyad* is the same in each spectrum but the relative intensity of each entire polyad pattern varies from one DF spectrum to the next. By taking advantage of this intrapolyad intensity invariance, the polyads may be separated from each other; *i.e.*, each DF spectrum may be "unzipped" into its component polyads. See Ref. [15] and Ref. [16] for further details and an extension of this concept to higher $\widetilde{X}$-state energies than the analysis presented here.

5.1.3 The $\hat{H}^{\mathcal{R}'}_{eff}$ Effective Hamiltonian

The $\hat{H}^{\mathcal{R}'}_{eff}$ Hamiltonian is the Hamiltonian used to describe the peaks observed in the SEP experiments carried out in the 7,000 cm^{-1} region [2]. This Hamiltonian contains the resonances known in the SEP, IR, Raman, and overtone [4] acetylene-h_2 data at that time. Since then, Abbouti Temsamani and Herman [7] have fit the 122 known experimental vibrational energy levels of acetylene-h_2 up to 12,000 cm^{-1}. These

levels are predominantly characterized by high quanta in the CH stretches and only minimal quanta in the bends. The comparison of the Ref. [7] Hamiltonian, $\hat{\mathbf{H}}^{H}_{eff}$, to ours will be discussed in Sec. 5.2.2.2. Abbouti Temsamani and Herman found it necessary to include additional stretch/bend resonances, $\mathcal{R}''_{C_2H_2}$, to the set of resonances traditionally used for acetylene-h_2, $\mathcal{R}'_{C_2H_2}$, to accurately describe the levels included in their global fit. The effect of these extra resonances was examined by comparing the old $\hat{\mathbf{H}}^{R'}_{eff}$ to the new $\hat{\mathbf{H}}^{R}_{eff}$=$\hat{\mathbf{H}}^{R'}_{eff}$+new resonances. The sets of resonances may be summarized as follows:

$$\mathcal{R}'_{C_2H_2} = \mathcal{B}_{C_2H_2} \cup \mathcal{S}_{C_2H_2} \cup \{\text{"3,245"}\} \tag{5.6}$$

$$\mathcal{R}''_{C_2H_2} = \{\text{"1,244"}, \text{"1,255"}, \text{"14,35"}\} \tag{5.7}$$

$$\mathcal{R}_{C_2H_2} = \mathcal{R}'_{C_2H_2} \cup \mathcal{R}''_{C_2H_2} \tag{5.8}$$

It is interesting to note that $\mathcal{R}_{C_2H_2}$ is linearly dependent on $\mathcal{R}'_{C_2H_2}$. In other words, $\mathcal{R}''_{C_2H_2}$ does not destroy any polyad numbers, and the new resonances only connected states within the same polyad as the $\mathcal{R}'_{C_2H_2}$ Hamiltonian. Also since the pure bend polyads, N_s=0, have no states with any stretch quanta, $\hat{\mathbf{H}}^{R}_{eff}$=$\hat{\mathbf{H}}^{R'}_{eff}$=$\hat{\mathbf{H}}^{B}_{eff}$ (Bend-only resonances) for $[0, N_{res}]$ polyads.

5.2 Analysis of States Below 10,000 cm^{-1}

All the peaks found in the $\widetilde{A} \rightarrow \widetilde{X}$ Origin Band DF spectrum below 16,000 cm^{-1} are summarized in Table 5.3.

It should be no surprise that a traditional spectroscopic polynomial expansion cannot describe all of the features in the Origin Band DF spectrum, since the higher resolution Origin Band DF spectrum shows more fractionation, compared to the previous $2\nu'_3$ and $3\nu'_3$ DF spectra, even for $E_{vib} \leq$10,000 cm^{-1} levels, see Fig. 5.4. For the analysis presented here, polyad quantum numbers are assigned to groups of $E_{vib} \leq$ 10,000 cm^{-1} features, see Table 5.4,

and polyad spectral intensity patterns are compared to the predictions of the $\hat{\mathbf{H}}^{R}_{eff}$ and $\hat{\mathbf{H}}^{R'}_{eff}$ models. See Refs. [15] and [16] for some of the dynamical information that the unzipping procedure provides for states above 10,000 cm^{-1}.

5.2.1 Pure Bending Polyads ($N_s = 0$)

As a consequence of the FC selectivity, the Origin Band DF spectrum contains (among others) polyads illuminated by *pure bending overtone states.* By inspection of $\mathcal{R}_{C_2H_2}$ (or equivalently the definition of N_s), it is evident that a pure bend overtone state can ONLY couple to other pure bend states. A bright state with nonzero excitation in the CC stretch would be mandatory for further IVR, such as occurs via stretch-bend, $\mathcal{X}_{C_2H_2}$, or stretch-only, $\mathcal{S}_{C_2H_2}$, interactions. Consequently, pure bend polyads offer an *ultra-restrictive* test of the extent to which $\mathcal{R}_{C_2H_2}$ describes the dynamics of acetylene.

Up to fourth order in the energy expression, the diagonal and off-diagonal bending constants, except for the second-order anharmonic constants, had been previously determined by Plíva [5] from a fit to $\sim$ 1200 acetylene-h_2 vibration-rotation energy levels with up to four quanta of bend excitation (at a standard deviation of 0.006 cm^{-1}). When Plíva included the second-order anharmonic interactions, DD Bend I and DD Bend II, the fit did not significantly improve [5]. Since the DD Bend II constant, d_{45}, is just the sum of the vibrational-ℓ-resonance constant, r_{45}, and the diagonal-in-ℓ constant, g_{45}, the only pure bend vibrational constant undetermined by Plíva was s_{45} [17]. If the $\hat{\mathbf{H}}^{R}_{eff}$ is qualitatively correct, then at the large bend excitation sampled in our DF spectrum, the sign and approximate value of $s^{h_2}_{45}$ can be determined by comparing the observed and predicted intensity patterns within each member of the $[0, N_{res}]$ series.

From the previously determined values of the acetylene-h_2 α_i's, $x_{tt'}$'s and $g_{tt'}$'s, $s^{h_2}_{45}$ can be estimated to be -9.3 cm^{-1} [2]. Alternatively, from isotopic substitution, the magnitude of $s^{h_2}_{45}$ can be approximated as |13| cm^{-1} from the observed value of $s^{d_2}_{45}$ [1, 18]. The intrapolyad intensity patterns predicted from the $\hat{\mathbf{H}}^{R}_{eff}$ for each member of the $[0, N_{res}]$ series were calculated and observed to vary smoothly for values of

Term Value (cm^{-1})	Relative Intensity	Term Value (cm^{-1})	Relative Intensity	Term Value (cm^{-1})	Relative Intensity	Term Value (cm^{-1})	Relative Intensity	Term Value (cm^{-1})	Relative Intensity
5072.1	0.115	9106.1	0.113	10786.1	0.071	12157.7	0.013	13003.7	0.020
5678.9	0.067	9119.8	0.059	10806.3	0.046	12195.0	0.050	13015.1	0.017
6331.1	0.026	9127.0	0.044	10828.2	0.017	12220.6	0.051	13051.7	0.009
6369.4	0.019	9140.0	0.314	10862.9	0.030	12238.7	0.053	13091.8	0.034
6389.9	0.309	9147.6	0.269	10881.1	0.019	12256.6	0.041	13139.3	0.028
6407.0	0.038	9154.5	0.072	10913.8	0.324	12267.6	0.029	13182.8	0.026
6427.0	0.104	9165.9	0.136	10919.8	0.293	12275.9	0.032	13218.8	0.039
6445.5	0.021	9177.0	0.038	10924.8	0.241	12290.9	0.086	13239.7	0.029
6461.3	0.013	9209.4	0.017	10935.6	0.195	12307.3	0.106	13251.5	0.040
6512.3	0.091	9240.1	0.029	10951.8	0.025	12322.8	0.119	13268.0	0.379
6961.3	0.301	9260.2	0.082	10965.4	0.012	12328.8	0.274	13303.9	0.019
7025.1	0.026	9268.6	0.044	10974.3	0.047	12343.7	0.095	13316.5	0.048
7128.7	0.023	9452.0	0.041	10985.8	0.185	12362.2	0.060	13327.7	0.031
7572.0	0.065	9492.0	0.049	11000.4	0.426	12369.5	0.034	13342.7	0.013
7621.6	0.059	9532.8	0.054	11016.9	0.374	12383.0	0.109	13366.9	0.034
7645.4	0.012	9587.3	0.962	11030.8	0.055	12395.7	0.092	13385.2	0.093
7666.7	0.030	9600.1	0.165	11048.5	0.048	12401.2	0.087	13411.6	0.050
7699.8	0.086	9620.9	0.251	11068.7	0.060	12425.0	0.321	13431.8	0.022
7735.3	0.504	9658.2	0.066	11077.0	0.057	12464.6	0.014	13464.7	0.008
7755.9	0.071	9675.5	0.233	11099.3	0.026	12484.2	0.022	13475.3	0.014
7774.4	0.055	9699.8	0.201	11119.0	0.071	12496.1	0.013	13489.7	0.021
7815.7	0.139	9707.2	0.196	11128.0	0.116	12512.0	0.018	13515.2	0.068
7840.6	0.050	9799.7	0.042	11297.3	0.032	12541.9	0.066	13537.6	0.022
7954.6	0.025	9833.4	0.089	11347.6	0.029	12548.7	0.038	13558.4	0.014
8217.6	0.029	9851.3	0.027	11411.4	0.163	12554.1	0.048	13572.6	0.023
8257.5	0.417	10113.4	0.248	11422.0	0.167	12616.6	0.020	13583.8	0.031
8287.0	0.382	10134.1	0.537	11447.7	0.626	12645.2	0.032	13595.9	0.025
8302.2	0.045	10144.1	0.116	11480.1	0.064	12653.8	0.016	13627.7	0.036
8329.4	0.018	10152.0	0.025	11525.9	0.180	12669.1	0.019	13644.6	0.063
8360.1	0.059	10168.8	0.097	11546.6	0.233	12693.8	0.008	13662.0	0.025
8373.9	0.028	10204.8	0.028	11556.4	0.124	12729.7	0.176	13692.3	0.007
8400.4	0.085	10218.2	0.021	11575.4	0.071	12741.3	0.201	13717.6	0.024
8439.5	0.044	10247.8	0.082	11679.3	0.061	12757.1	0.148	13726.6	0.032
8469.7	0.021	10273.4	0.122	11692.4	0.042	12763.5	0.238	13740.4	0.138
8498.3	0.029	10285.4	0.048	11812.4	0.022	12791.9	0.043	13751.0	0.067
8798.0	0.007	10311.9	0.020	11834.0	0.030	12800.5	0.032	13759.1	0.027
8816.0	0.016	10359.9	0.067	11873.3	0.024	12818.7	0.113	13782.3	0.036
8839.4	0.299	10438.3	0.028	11904.9	0.156	12825.0	0.126	13789.6	0.071
8856.0	0.025	10457.1	0.034	11917.4	0.076	12845.0	0.422	13795.8	0.138
8879.1	0.021	10475.4	0.126	11931.4	0.043	12853.9	0.247	13805.4	0.034
8896.7	0.029	10494.2	0.178	11962.1	0.153	12865.5	0.070	13813.9	0.029
8910.3	0.036	10505.4	0.062	11973.4	0.183	12884.2	0.014	13824.8	0.017
8936.3	0.034	10524.4	0.013	12003.2	0.081	12894.4	0.039	13843.7	0.104
8946.4	0.103	10536.8	0.014	12011.5	0.088	12903.2	0.045	13851.7	0.045
8954.9	0.054	10550.7	0.038	12034.7	0.010	12916.4	0.027	13868.9	0.008
9012.7	0.017	10564.6	0.083	12056.8	0.019	12925.6	0.058	13906.1	0.034
9047.3	0.088	10579.0	0.128	12091.7	0.020	12944.5	0.022	13916.3	0.031
9061.5	0.034	10617.2	0.009	12101.8	0.084	12961.1	0.045	13935.7	0.004
9076.0	0.221	10635.2	0.016	12111.1	0.049	12974.3	0.088	13947.8	0.020
9093.2	0.093	10699.6	0.194	12125.0	0.074	12993.5	0.029	13971.8	0.028

Table 5.3: Observed term values(cm^{-1}), $2\bar{\sigma}$=1.5 cm^{-1}, and intensities(a.u.), $2\bar{\sigma}$ = 0.024, for the Origin Band DF Spectrum for levels $E_{vib} < 16,000$ cm^{-1}.

Term Value (cm^{-1})	Relative Intensity	Term Value (cm^{-1})	Relative Intensity	Term Value (cm^{-1})	Relative Intensity	Term Value (cm^{-1})	Relative Intensity	Term Value (cm^{-1})	Relative Intensity
13995.2	0.015	14292.8	0.028	14672.5	0.180	15143.0	0.016	15480.1	0.014
14010.8	0.011	14314.1	0.010	14686.1	0.027	15151.5	0.038	15499.7	0.013
14021.6	0.019	14333.8	0.025	14693.7	0.046	15157.5	0.027	15516.9	0.005
14052.7	0.086	14370.2	0.026	14736.8	0.030	15173.3	0.015	15530.7	0.032
14058.5	0.077	14391.8	0.018	14743.4	0.030	15181.9	0.009	15546.8	0.030
14068.1	0.046	14398.8	0.022	14750.2	0.031	15193.1	0.011	15555.0	0.115
14096.4	0.024	14406.3	0.037	14768.3	0.022	15204.0	0.023	15564.8	0.038
14103.2	0.051	14422.5	0.019	14783.3	0.014	15209.5	0.032	15581.3	0.016
14120.2	0.015	14432.1	0.015	14795.5	0.017	15215.6	0.050	15597.8	0.015
14132.2	0.031	14448.7	0.009	14805.8	0.019	15223.3	0.022	15609.0	0.034
14141.0	0.046	14459.1	0.017	14821.9	0.036	15259.7	0.019	15621.4	0.033
14148.4	0.145	14466.5	0.005	14834.9	0.020	15284.5	0.013	15630.7	0.030
14159.2	0.198	14479.3	0.006	14860.0	0.018	15302.8	0.008	15647.1	0.014
14171.0	0.055	14502.8	0.012	14919.3	0.019	15309.2	0.005	15668.6	0.031
14176.8	0.033	14519.5	0.023	14940.5	0.032	15320.2	0.015	15679.3	0.013
14187.3	0.035	14529.8	0.039	14949.5	0.012	15328.2	0.010	15687.6	0.033
14213.0	0.031	14537.6	0.023	14964.8	0.006	15338.7	0.020	15692.8	0.030
14222.6	0.041	14549.9	0.003	15026.3	0.011	15347.9	0.009	15704.2	0.003
14228.7	0.032	14572.5	0.306	15047.5	0.033	15354.9	0.029	15715.4	0.012
14237.3	0.017	14586.1	0.026	15055.2	0.030	15386.3	0.009	15733.4	0.003
14244.3	0.045	14594.8	0.021	15065.4	0.065	15396.8	0.012	15745.8	0.009
14255.1	0.115	14604.9	0.020	15093.0	0.110	15429.5	0.014	15755.4	0.012
14261.2	0.100	14614.5	0.018	15107.6	0.005	15446.1	0.007		
14266.8	0.075	14641.8	0.004	15120.2	0.021	15451.5	0.043		
14280.6	0.051	14655.2	0.016	15128.4	0.015	15467.6	0.019		

Table 5.3: cont. Observed term values(cm^{-1}), $2\bar{\sigma}$=1.5 cm^{-1}, and intensities(a.u.), $2\bar{\sigma} = 0.024$, for the Origin Band DF Spectrum for levels $E_{vib} < 16,000$ cm^{-1}.

Polyad Assignment	Zero-Order Bright State	Term Value (cm^{-1})	Relative Intensity
$[0,8]_g$	$(0,0,0,8,0)$	5072.1	0.115
$[0,10]_g$	$(0,0,0,10,0)$	6369.4	0.019
		6389.9	0.309
		6407.0	0.038
		6427.0	0.104
		6445.5	0.021
		6461.3	0.013
		6512.3	0.091
$[0,12]_g$	$(0,0,0,12,0)$	7621.6	0.059
		7645.4	0.012
		7666.7	0.030
		7699.8	0.086
		7735.3	0.504
		7755.9	0.071
		7774.4	0.055
		7815.7	0.139
		7840.6	0.050
		7954.6	0.025
$[0,14]_g$	$(0,0,0,14,0)$	8910.3	0.036
		8936.3	0.034
		8946.4	0.103
		8954.9	0.054
		9047.3	0.088
		9061.5	0.034
		9076.0	0.221
		9093.2	0.093
		9106.1	0.113
		9119.8	0.059
		9127.0	0.044
		9140.0	0.314
		9147.6	0.269
		9154.5	0.072
		9165.9	0.136
		9177.0	0.038
		9209.4	0.017
		9240.1	0.029
		9260.2	0.082
		9268.6	0.044

Polyad Assignment	Zero-Order Bright State	Term Value (cm^{-1})	Relative Intensity
$[1,9]_g$	$(0,1,0,6,0)$	5678.9	0.067
$[1,11]_g$	$(0,1,0,8,0)$	6961.3	0.301
		7025.1	0.026
		7128.7	0.023
$[1,13]_g$	$(0,1,0,10,0)$	8257.5	0.417
		8287.0	0.382
		8302.2	0.045
		8329.4	0.018
		8360.1	0.059
		8373.9	0.028
		8400.4	0.085
		8439.5	0.044
		8469.7	0.021
		8498.3	0.029
$[1,15]_g$	$(0,1,0,12,0)$	9492.0	0.049
		9532.8	0.054
		9587.3	0.962
		9600.1	0.165
		9620.9	0.251
		9658.2	0.066
		9675.5	0.233
		9699.8	0.201
		9707.2	0.196
		9799.7	0.042
		9833.4	0.089
		9851.3	0.027
$[2,10]_g$	$(0,2,0,4,0)$	6331.1	0.026
$[2,12]_g$	$(0,2,0,6,0)$	7572.0	0.065
$[2,14]_g$	$(0,2,0,8,0)$	8798.0	0.007
		8816.0	0.016
		8839.4	0.299
		8856.0	0.025
		8879.1	0.021
		8896.7	0.029
		9012.7	0.017
$[3,13]_g$	$(0,3,0,4,0)$	8217.6	0.029
$[3,15]_g$	$(0,3,0,6,0)$	9452.0	0.041

Table 5.4: Listing of the peaks, $E_{vib} < 10,000$ cm^{-1}, in the Origin Band DF spectrum by Polyads. Note the increase in fractionation for fixed N_s as N_{res} is increased.

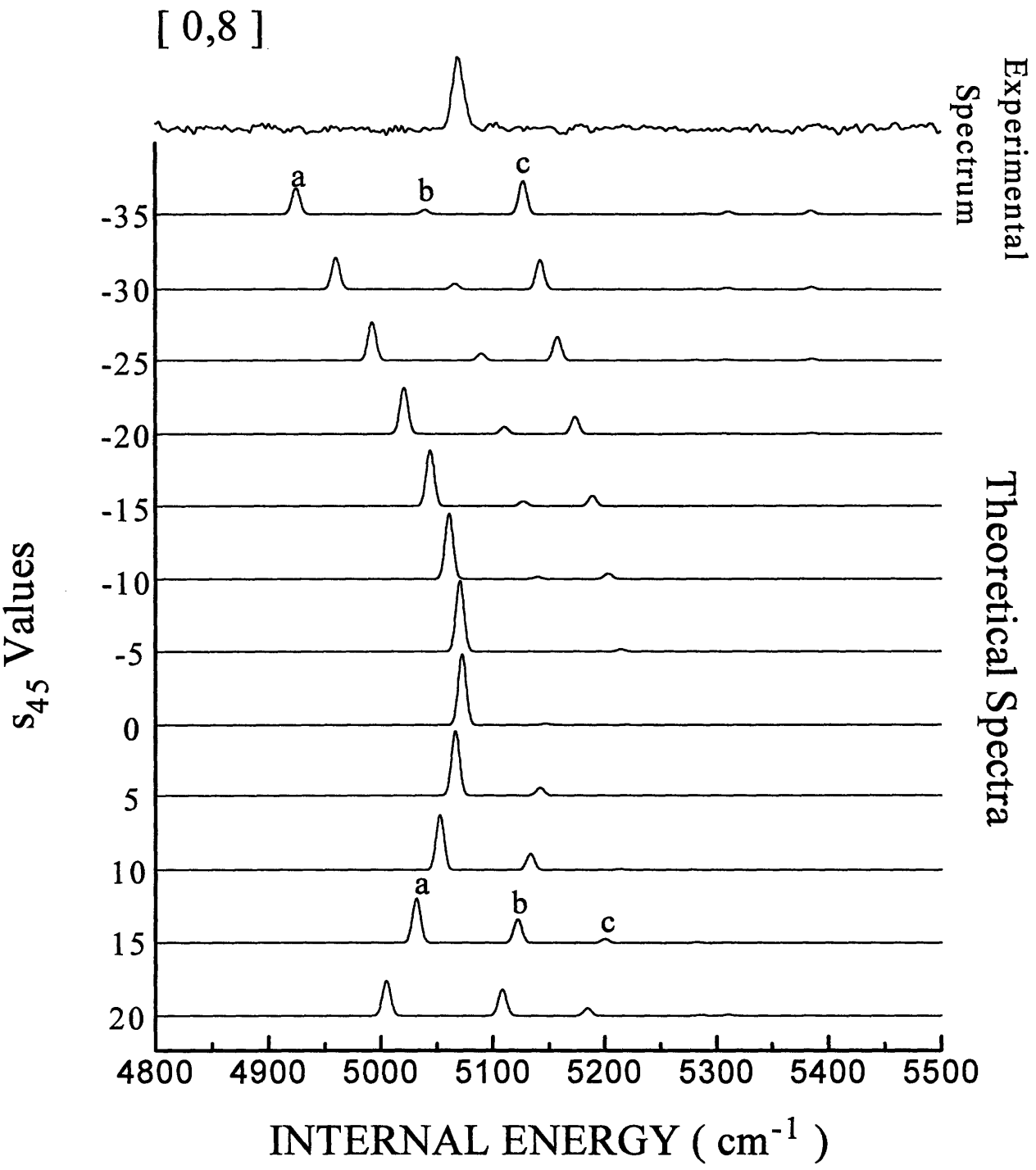

Figure 5.5: The calculated theoretical spectrum for the $[0, 8]$ polyad is calculated from our $\hat{\mathbf{H}}^{\mathrm{R}}_{eff}$ for different values of the DD Bend I resonance constant, s_{45}, and compared to the experimental Origin Band DF spectrum

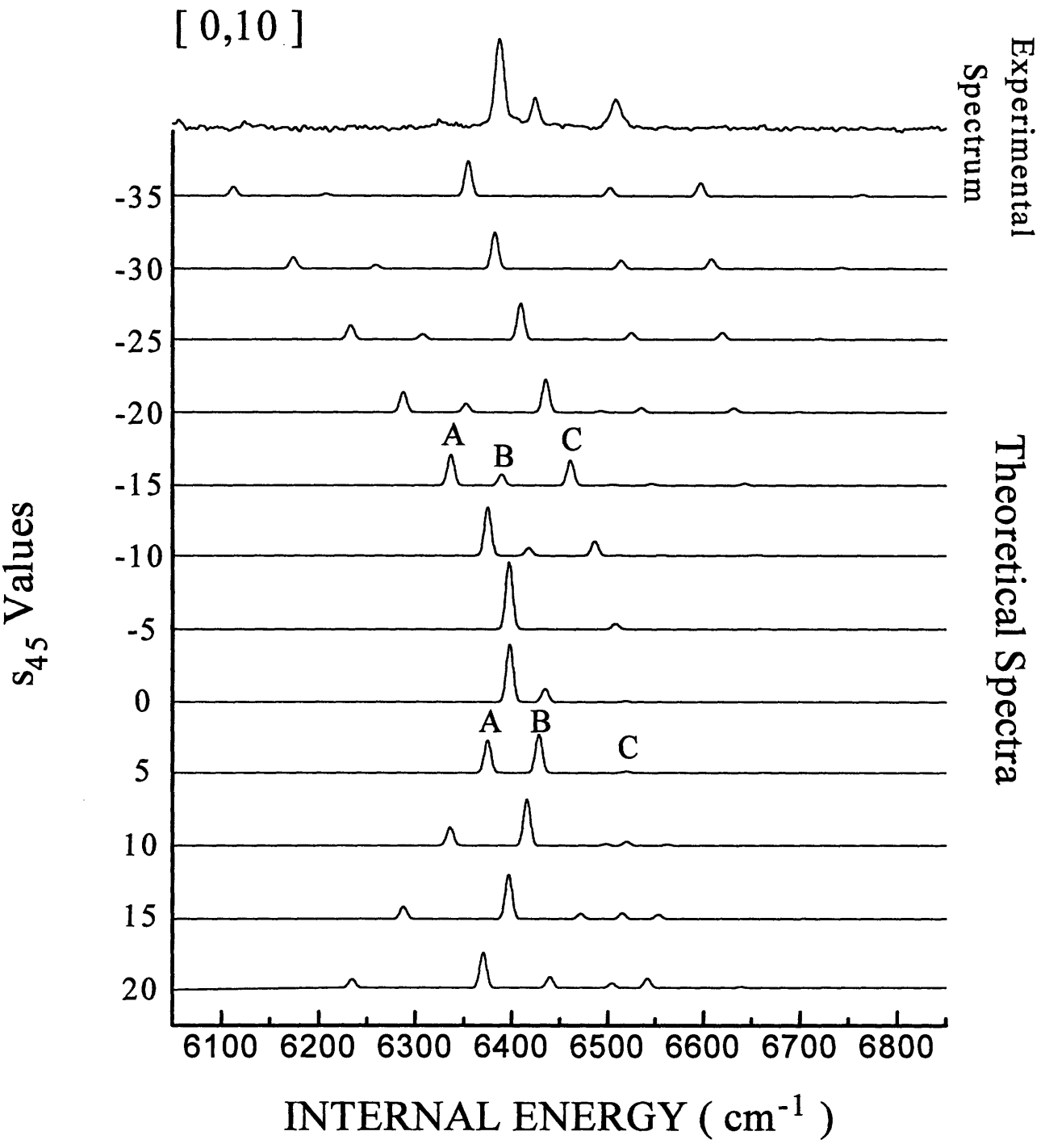

Figure 5.6: The calculated theoretical spectrum for the [0, 10] polyad is calculated from our $\hat{\mathbf{H}}^{\mathrm{R}}_{eff}$ for different values of the DD Bend I resonance constant, s_{45}, and compared to the experimental Origin Band DF spectrum

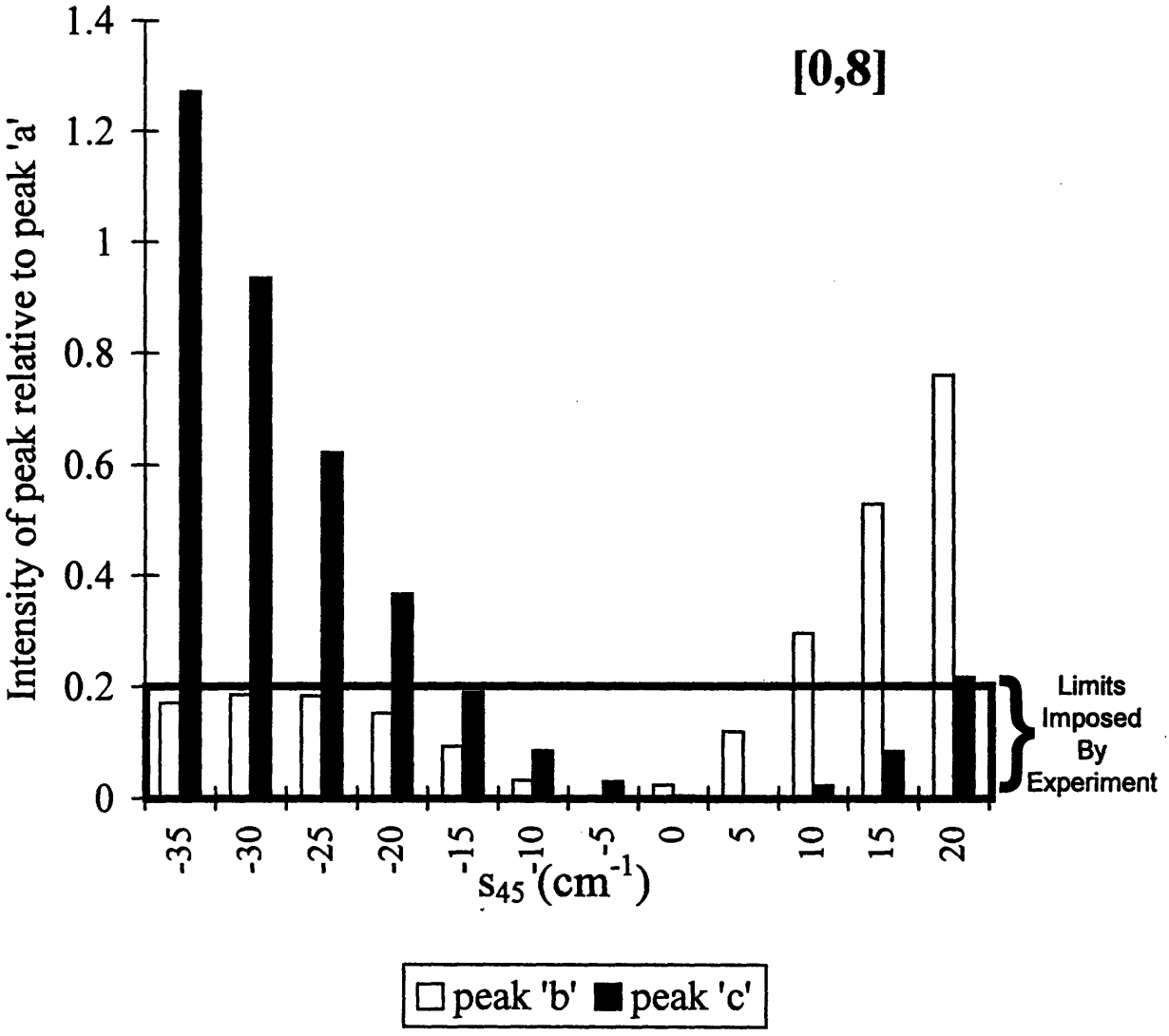

Figure 5.7: The ratio of peak 'b'/peak 'a' and peak 'c'/peak 'a' from the calculated theoretical spectrum for the [0,8] polyad from our $\hat{H}^R_{eff}$ is plotted for a range of values of the DD Bend I resonance constant, s_{45}, see Fig. 5.5. The experimental Origin Band spectrum places limits on the ratios, shown here as the shaded region. Since both ratios must lie within the shaded region, the value of $s^{h_2}_{45}$ is bounded by -20 cm^{-1} < $s^{h_2}_{45}$ < $+10$ cm^{-1}.

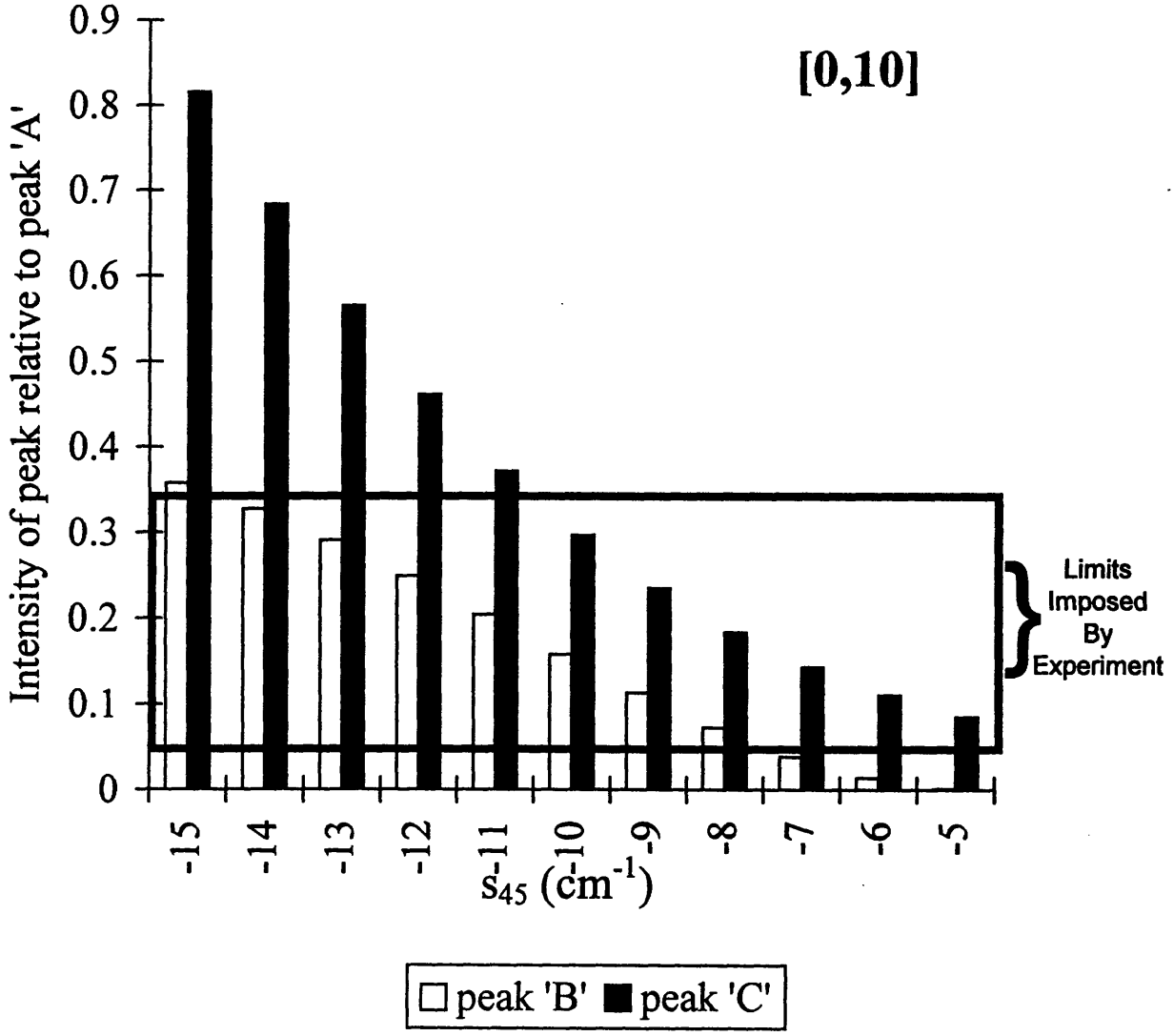

Figure 5.8: The ratio of peak 'B'/peak 'A' and peak 'C'/peak 'A' from the calculated theoretical spectrum for the [0, 10] polyad from our $\hat{\mathbf{H}}^{\mathbf{R}}_{eff}$ is plotted for a range of values of the DD Bend I resonance constant, s_{45}, see Fig. 5.6. The experimental Origin Band spectrum places limits on the ratios, shown here as the shaded region. Since both ratios must lie within the shaded region, the value of $s^{h_2}_{45}$ is calculated to be -11(2) cm^{-1}.

$s_{45}^{h_2}$ between -50 cm$^{-1}\leq s_{45}^{h_2} \leq +50$ cm^{-1}. As an example, the intrapolyad intensity patterns for the [0,8] and the [0,10] polyads are plotted in Fig. 5.5 and Fig. 5.6, respectively, for values of $s_{45}^{h_2}$ in the range -35 cm$^{-1}\leq s_{45}^{h_2} \leq +20$ cm^{-1}. In the experimental Origin Band DF Spectrum, only one peak is evident in the [0,8] polyad. By comparing the relative intensities of the extra peaks (Fig. 5.5), 'b' and 'c', to peak 'a', and accounting for a worst case signal/noise scenario, the only acceptable values of $s_{45}^{h_2}$ are those that imply that the ratios 'b'/'a' and 'c'/'a' should fall within the shaded region of Fig. 5.7. This puts bounds on the value of $s_{45}^{h_2}$: -20 cm$^{-1}< s_{45}^{h_2} < +10$ cm^{-1}. Upon inspection of Fig. 5.6, the three-peak [0,10] polyad in the experimental Origin Band DF Spectrum looks very similar to the predicted pattern for $s_{45}= -10$ cm^{-1}. In Fig. 5.8 the predicted peak ratios, 'B'/'A' and 'C'/'A', of the three-peak pattern are plotted versus the value of $s_{45}^{h_2}$. By indicating the experimentally determined intensity ratios (with generous uncertainties) for both the 'B' and 'C' peaks by the shaded region in Fig. 5.8, the value of $s_{45}^{h_2}$ is determined to be -11(2) cm^{-1}, since both peaks' ratios must lie in the shaded region.

In Fig. 5.9 the theoretical spectrum, $\hat{\mathbf{H}}^{\mathrm{R}}_{eff}$, for the [0,12] polyad with $s_{45}^{h_2}$=-11 cm^{-1} is plotted with the experimental Origin Band DF Spectrum. The qualitative agreement of the theoretical spectrum, $\hat{\mathbf{H}}^{\mathrm{R}}_{eff}$, with the experimental spectrum for the [0,12] polyad, as well as the [0,10] and [0,8] polyads, is interesting since the constants (with the exception of $s_{45}^{h_2}$) used in the $\hat{\mathbf{H}}^{\mathrm{R}}_{eff}$ for the bending resonances are derived from fits to spectra with *eight fewer quanta of the bend* [5].

Most theoretical studies of highly excited systems including acetylene [19,20], choose basis sets where the bending vibrations are described roughly as "chemist's bends", *i.e.* bond-angle internal coordinate representation. Fits of such Hamiltonians to highly excited acetylene data invariably imply large bend-stretch couplings [19] in those basis sets. Either the dynamics are ergodic or the chemist's bend type of basis set is not a good description of the system. Spectroscopists, on the other hand, tend to favor the rectilinear normal mode spectroscopic Hamiltonian, due in part to the easily generated matrix elements needed for their fit models [21,22]. The new Origin Band DF spectrum indicates that spectroscopic *normal mode* bend states, although coupled to each other but totally decoupled from the normal mode stretches, appear to provide a good description of very highly excited bend levels in acetylene. Interestingly, Sibert's [23] *planar* acetylene calculation (using an extension of the coordinate system first used on acetylene by Bentley [24]) also shows a tendency to conserve the total quanta of bend up to $v_4 + v_5 = 16$.

5.2.2 Polyads with CC Stretch ($N_s > 0$)

The intermediate states used in our DF spectra result in FC activity in very high quanta of the *trans*-bend, v_4, and moderate quanta in the CC stretch, v_2. Thus $(0, V_2, 0, V_4, 0)$ is the set of zero-order bright states, or chromostates, prepared in our DF spectrum. The polyads that contain these states have low values of N_s and high values of N_{res} because

$$N_s = v_1 + v_2 + v_3 = V_2$$

and

$$N_{res} = 5v_1 + 3v_2 + 5v_3 + v_4 + v_5 = 3V_2 + V_4.$$

Although the $\hat{\mathbf{H}}^{\mathrm{R}}_{eff}$ qualitatively describes the spectral pattern observed in the Origin Band DF spectrum for the pure bend polyads (N_s=0) up to $V_4 = 12$, the polyads in the DF Spectrum with even minimal stretch character (N_s= 1) do not agree with predictions of the $\hat{\mathbf{H}}^{\mathrm{R}}_{eff}$ for $V_4 > 8$. Possible reasons for the disagreement can be understood by inspection of the structure of the $\hat{\mathbf{H}}^{\mathrm{R}}_{eff}$: the typical matrix elements, H_{ij}, and zero-order energy denominators, ΔE.

5.2.2.1 Internal Structure of the Polyads

As described at the beginning of the chapter, the $\hat{\mathbf{H}}^{\mathrm{R}}_{eff}$ was constructed from a normal mode basis set and includes diagonal anharmonicities and off-diagonal couplings [21,22]. The quantum number dependence of the scalable off-diagonal matrix elements and the values of the fitted constants are given in Table 5.2.

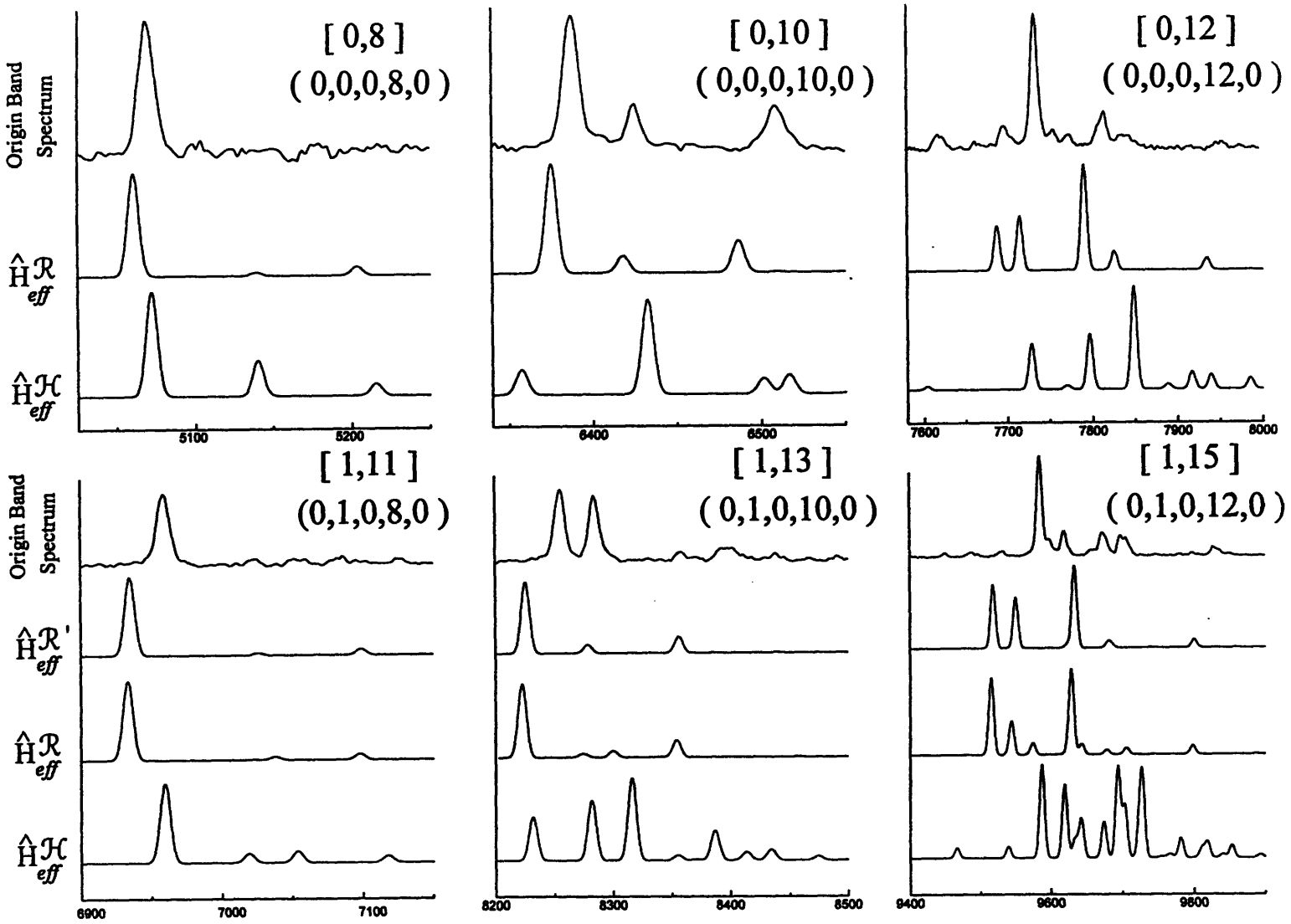

Figure 5.9: The theoretical spectra calculated from our $\hat{H}^{R}_{eff}$ and $\hat{H}^{R'}_{eff}$ with $s^{h_2}_{45} = -11$ cm^{-1} and from $\hat{H}^{H}_{eff}$ for the pure bend polyad series and the polyad series with one quantum in the stretch, $[0,8]/[0,10]/[0,12]$ and $[1,11]/[1,13]/[1,15]$, respectively, compared to the Origin Band DF spectrum.

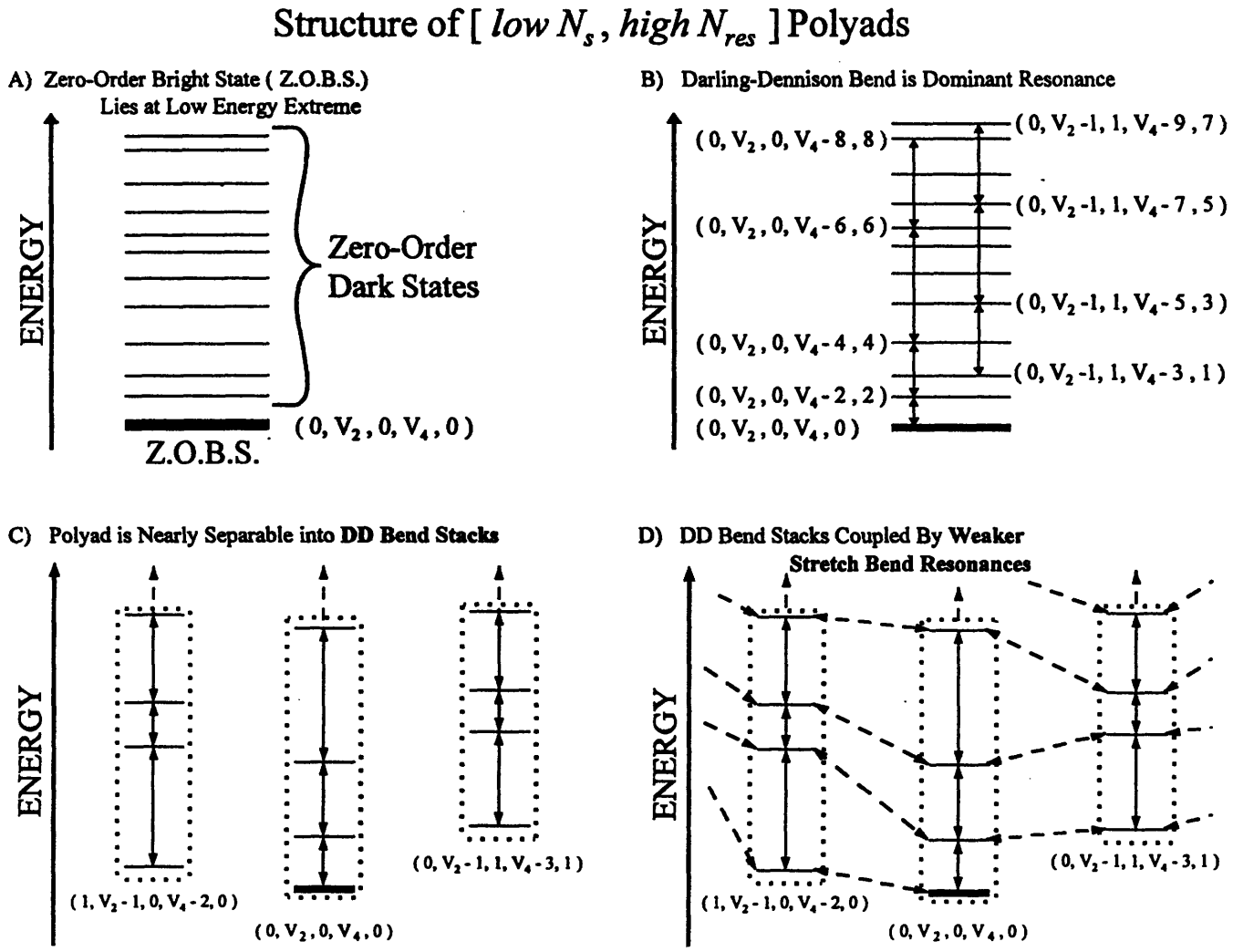

Figure 5.10: The structure of the low energy extreme of the [*low* N_s, *high*N_{res}] polyads.

In the [*low* N_s, *high* N_{res}] polyads, the zero-order bright state $(0, V_2, 0, V_4, 0)$ lies at the low energy extreme of its polyad, see Fig. 5.10a, as can be seen from the location of the strongest peak in the theoretical spectrum for $\hat{\mathbf{H}}^{\mathrm{R}}_{eff}$ in Fig. 5.9 for the polyads [0,8], [0,10], [1,11] and [1,13], which correspond to chromostates (0,0,0,8,0), (0,0,0,10,0), (0,1,0,8,0) and (0,1,0,10,0). As can be seen in Fig. 5.10b, the nearest neighbor intrapolyad zero-order state to $(0, V_2, 0, V_4, 0)$ is $(0, V_2, 0, V_4 - 2, 2)$, which also happens to be a state to which the bright state can couple most strongly via a Darling-Dennison (DD) bend resonance with a typical matrix element and zero-order energy denominator, $\mathrm{H}_{ij}/\Delta\mathrm{E}\approx 55/75$ cm^{-1} at $V_4 = 10$. Entering the next tier of coupled levels, by again applying the DD bend resonance, the $(0, V_2, 0, V_4 - 2, 2)$ state is coupled to $(0, V_2, 0, V_4 - 4, 4)$, with $\mathrm{H}_{ij}/\Delta\mathrm{E}\approx 88/80$ cm^{-1}, and so on, forming a "DD Bend stack". In the low energy region of the [*low* N_s, *high* N_{res}] polyads, the strongest resonances, in terms of $\mathrm{H}_{ij}/\Delta\mathrm{E}$, are generally the bend-only resonances, $\mathcal{B}_{C_2H_2}$. This partitions the low energy end of the polyad into $\binom{N_s+2}{2}$ DD Bend Stacks, see Figure 5.10c, one for each unique (v_1, v_2, v_3) combination [25]. These DD Bend stacks, $\{(0, V_2, 0, V_4, 0), (0, V_2, 0, V_4 - 2, 2), \dots\}$ and $\{(1, V_2 - 1, 0, V_4 - 2, 0), (1, V_2 - 1, 0, V_4 - 4, 2), \dots\}$, *etc.*, see Figure 5.10d, are interconnected by a web of weaker resonances, stretch-bend ($\mathcal{X}_{C_2H_2}$) and stretch-only ($\mathcal{S}_{C_2H_2}$), typically with $\mathrm{H}_{ij}/\Delta\mathrm{E}\approx 9/30\mathrm{cm}^{-1}$.

Polyad fractionation, and hence the extent of IVR, increases with increasing V_4, and therefore N_{res}, see Table 5.4. First, since the DD Bend matrix element is roughly proportional to $\sim v_4(v_5 + 2)$, see Table 5.2, increasing v_4 increases H_{ij}. Second, since $\omega_4^0(609\ \mathrm{cm}^{-1})$ is less than $\omega_5^0(729\ \mathrm{cm}^{-1})$ but x_{44}^0 is positive(+3.1 cm^{-1}) and x_{55}^0 is negative($-2.3\ \mathrm{cm}^{-1}$) [2], the ΔE's between successive members of the DD Bend stacks decrease as V_4 increases; thus, the DD Bend stacks compress. The increase in polyad fractionation with increasing V_4 (hence N_{res}), due to the increase in H_{ij} combined with the stack compression (decrease in ΔE) is evident in the evolution of the polyad fractionation pattern for the polyads [0,8] to [0,10] to [0,12] from (one peak) to (one strong peak/two weak peaks on the high energy side) to (one strong/many weak peaks) in both the Origin Band DF spectrum and the theoretical spectrum for $\hat{\mathbf{H}}^{\mathrm{R}}_{eff}$, see Fig. 5.9. Since each polyad in the $[0, N_{res}]$ polyad series has only one DD Bend Stack, the preceding evolution of the polyad fractionation pattern (increasing fractionation with increasing N_{res}) reflects increasing IVR further into the DD Bend Stack.

5.2.2.2 Comparison of the N_s=0 Polyads to the N_s=1 Polyads

The polyad fractionation patterns for the theoretical spectra of the $\hat{\mathbf{H}}^{\mathrm{R}}_{eff}$ for the [0,8]/[0,10]/[0,12] polyad series are very similar to the polyad fractionation patterns for theoretical spectra of the $\hat{\mathbf{H}}^{\mathrm{R}}_{eff}$ and $\hat{\mathbf{H}}^{\mathrm{R}'}_{eff}$ for the [1,11]/[1,13]/[1,15] polyad series (the respective polyads only differ by one quantum of CC stretch, V_2), see Fig. 5.9. The fractionation patterns for polyads [0,8] and [1,11] that have $V_4 = 8$ show one strong peak with two extremely weak peaks on the high energy side, while the fractionation patterns for polyads [0,10] and [1,13] that have $V_4 = 10$ show one strong peak with two weak peaks on the high energy side, and the fractionation patterns for polyads [0,12] and [1,15] that have $V_4 = 12$ show a strongest middle peak surrounded by several peaks, the weaker of which lie on the high energy side of the main peak. This similarity in appearance of the polyads with the same V_4 shows that, in the $\hat{\mathbf{H}}^{\mathrm{R}}_{eff}$ for the low energy extreme of the [*low* N_s, *high* N_{res}] polyads, the main IVR pathway is still upward along the initial DD Bend Stack rather than outward to nearby stacks, since the spectral patterns for the polyads which contain only one stack, N_s=0, match the spectral patterns for the polyads with three stacks, N_s=1, for the same quanta of V_4. This is also borne out by the similarity of the spectral patterns for $\hat{\mathbf{H}}^{\mathrm{R}}_{eff}$ and $\hat{\mathbf{H}}^{\mathrm{R}'}_{eff}$.

The similarity of the spectral patterns for the [1,11]/[1,13]/[1,15] polyad series for both the $\hat{\mathbf{H}}^{\mathrm{R}}_{eff}$ and $\hat{\mathbf{H}}^{\mathrm{R}'}_{eff}$ shows that, even with additional stretch/bend resonances, the main IVR pathway is up the DD Bend Stack, rather than out to nearby stacks. Unfortunately, the experimental Origin Band DF spectrum does not even qualitatively match the theoretical spectrum for the [1,13] and [1,15] polyads, in marked contrast to the reasonable match for the [0,8]/[0,10]/[0,12] series. It seems that the $\hat{\mathbf{H}}^{\mathrm{R}}_{eff}$ does not describe the dynamics for $V_4 > 8$ when $V_2 = 1$. Either a new resonance has become important, or the values of the fitted diagonal and off-diagonal molecular constants are too far off to reproduce the polyads with even minimal stretch character. A hitherto neglected resonance could be either intrapolyad or interpolyad (which would destroy one of the

Dominant Zero-Order Character	$J_{\ell,\text{parity}}$	Obs. SEP Term Value	Matching DF Term Value	Polyad Assignment	Zero-Order Bright State
$(0,1,0,8^0,0)^0$	$1_{0,e}$	6960.363	6961.3	$[1,11]_g$	$(0,1,0,8,0)$
$(0,1,0,8^{\mp 2},0)^2$	$2_{2,f}$	6963.804	6961.3	$[1,11]_g$	$(0,1,0,8,0)$
$(0,1,0,6^{\pm 2},2^{\mp 2})^0$	$1_{0,e}$	7022.962	7025.1	$[1,11]_g$	$(0,1,0,8,0)$
$(0,1,0,6^{\mp 4},2^{\pm 2})^2$	$2_{2,f}$	7026.038	7025.1	$[1,11]_g$	$(0,1,0,8,0)$
$(0,1,0,6^0,2^0)^0$	$1_{0,e}$	7123.115	7128.7	$[1,11]_g$	$(0,1,0,8,0)$
$(0,1,0,6^0,2^{\mp 2})^2$	$2_{2,f}$	7129.890	7128.7	$[1,11]_g$	$(0,1,0,8,0)$

Table 5.5: Observed SEP Term Values in the 7,000 cm^{-1} region [2] and the corresponding peaks in the Origin Band DF Spectrum (all units in cm^{-1}).

polyad quantum numbers). From the unzipping procedure, see [15,16], we know that $\mathcal{N}_{C_2H_2}$ remains good up to at least 16,000 cm^{-1}; therefore the new resonance must be an additional *intrapolyad* resonance. This new resonance could also be an "accidental" resonance, a resonance that appears when levels are "accidentally" close enough to allow a small H_{ij} to affect the spectrum, as opposed to a "dynamical" resonance that is strong/active throughout the spectrum. High resolution SEP studies of the [1, 13] and [1, 15] polyads would identify the nature and strength of this new resonance. If the *real* Hamiltonian mimics the $\hat{\mathbf{H}}^{\mathrm{R}}_{eff}$ in the sense that the IVR is predominantly upward along each DD Bend Stack, it is plausible that the [1, 13] polyad is affected by an accidental resonance, because the experimental intensity pattern for the [1, 15] polyad appears to be qualitatively closer to that of the [0, 12] polyad (they differ by only one quantum of CC stretch), than the intensity pattern of the [1, 13] polyad is to that of the [0, 10] polyad, see Fig. 5.9.

The Hamiltonian of Abbouti Temsamani and Herman [7], $\hat{\mathbf{H}}^{\mathrm{H}}_{eff}$, included fitted values only up to the x_{ij}'s for the diagonal terms. Since Plíva's fit to the bend-only states included higher-order diagonal terms for the bends, it is not surprising that the $\hat{\mathbf{H}}^{\mathrm{R}}_{eff}$ qualitatively matches the Origin Band DF spectrum better than the $\hat{\mathbf{H}}^{\mathrm{H}}_{eff}$, see Fig. 5.9. Since the $\hat{\mathbf{H}}^{\mathrm{H}}_{eff}$ theoretical polyad spectral patterns, especially the [1, 13] and [1, 15] polyads, show much more fractionation than the Origin Band DF spectrum, it is plausible that the off-diagonal couplings in the $\hat{\mathbf{H}}^{\mathrm{H}}_{eff}$ are too strong. Qualitatively speaking, a reduction in the magnitudes of the off-diagonal coupling constants and inclusion of higher-order terms on the diagonal might produce an effective Hamiltonian model that would match all of the known acetylene levels.

5.3 Comparison to Previous SEP Spectra

5.3.1 The 7,000 cm^{-1} Region SEP Spectrum

Since the sensitivity range of SEP (~1000:1) [26] is greater than that of the Origin Band DF (~100:1) spectrum, only the three most intense features of the 7,000 cm^{-1} SEP spectrum [2] are observed in the Origin Band DF spectrum. The peaks and their polyad assignments, from the DF analysis, as well as the dominant zero-order character of each level, from the SEP analysis, are listed in Table 5.5

along with their respective term values. As previously stated, the accuracy of the new Origin Band Band DF spectrum is 1–2 cm^{-1} for a resolution of 7 cm^{-1}.

5.3.2 The 9,500 cm^{-1} Region SEP Spectrum

SEP scans for a single $\widetilde{A}\,^1A_u3^3 \leftarrow \widetilde{X}\,^1\Sigma_g^+4_0\ ^rQ_0(5)$ PUMP transition were recorded previously in the 9,500 cm^{-1} region [27,28]. The allowed $\widetilde{A} \rightarrow \widetilde{X}$ SEP DUMP transitions subsequent to a $^rQ_0(5)$ PUMP terminate in $J_{\ell,\text{parity}}$=$4_{2,f}$,$5_{0,e}$,$5_{2,e}$ and $6_{2,f}$ rotational levels. The transition to the $4_{2,f}$ level is often missing since the predicted relative intensities of the transitions terminating in the four lower levels, $4_{2,f} : 5_{0,e} : 5_{2,e} : 6_{2,f}$, are 0.05 : 1 : 0.5 : 0.25 (with the PUMP polarization parallel to the DUMP polarization).

The observed SEP transitions in the 9,500 cm^{-1} region with known $J_{\ell,\text{parity}}$ (from rough relative intensities and correct rotational spacing) are tabulated in Table 5.6a.

As was previously noted [27], the 9,480 cm^{-1} and 9,615 cm^{-1} groups of lines were assigned to zero-order basis states (0,3,0,6,0) and (0,1,0,12,0), respectively, based on the B_v^{exp} and G_v^{exp} calculated from the observed SEP transitions. A predicted term value for the $1_{0,e}$ and $2_{2,f}$ rotational levels (the levels that would be observable in the Origin Band DF spectrum) for each vibrational state can be calculated from the B_v^{exp} and G_v^{exp} determined by the SEP transitions. The calculated term values match, within the experimental uncertainty of the Origin Band DF spectrum, the corresponding Origin Band DF peaks listed in Table 5.6a. The polyad assignment and zero-order bright state determined from the DF polyad analysis match that determined from the SEP rovibrational analysis.

For the group of lines at 9,650 cm^{-1}, although the $4_{2,f}$ transition is to weak to detect, the three peaks listed in Table 5.6a are consistent with $5_{0,e}$,$5_{2,e}$ and $6_{2,f}$ rotational assignments based on relative intensities and rough rotational splittings [27]. The calculated term value and matching DF assignment are also listed in Table 5.6a.

From the polyad analysis, the peaks observable in the 9,490–9,900 cm^{-1} range of the Origin Band DF spectrum belong to the (0,1,0,12,0) bright state of the $[1,15]_g$ polyad. If the rest of the SEP transitions observed in the 9,500 cm^{-1}region, Table 5.6b, are observed owing to intrapolyad vibrational resonances [29], then the probable rotational assignments are $5_{0,e}$,$5_{2,e}$ and $6_{2,f}$ [30]. The calculated term values that would then be observable in our DF spectrum are listed in Table 5.6b and plotted in Fig. 5.11a. From this calculation it is plausible that every observed SEP transition [27,28] is accounted for in the Origin Band DF spectrum. In addition, *every peak in the Origin Band DF spectrum in the regions scanned by SEP has its counterpart in the SEP spectrum.* Thus the probable $J_{\ell,\text{parity}}$ and polyad vibrational character assignments are all identified for peaks in the 9,500 cm^{-1} region of the SEP and DF spectra.

5.3.3 The 11,400 cm^{-1} Region SEP Spectrum

The SEP studies in the 11,400 cm^{-1} region [31] determined B_v^{exp} and G_v^{exp} values for the five observed vibrational bands. The B_v^{exp}'s and G_v^{exp}'s are listed in Table 5.7 along with the calculated term values for the rovibrational levels that would be observable in the Origin Band DF spectrum and the matching DF term values.

The only band that does not appear in the Origin Band DF spectrum is Band 3 of Ref. [31] which has a very unphysical B_v^{exp}=1.050. This anomalous B_v^{exp} value probably reflects a Coriolis interaction which gives rise to transitions too weak to be seen in the DF spectrum. Again, every SEP transition that should appear in the Origin Band DF spectrum is observed, and every DF transition has its counterpart in the SEP spectrum, see Fig. 5.11b. Vibrational assignments from the DF spectrum for this region will be presented in a forthcoming paper [15].

5.4 Conclusion

A new higher resolution dispersed fluorescence (DF) spectrum has been recorded from the zero-point level (Origin Band) of the $\widetilde{A}$-state, which allows us to elaborate a more complete picture of the energy flow pathways on the acetylene $\widetilde{X}$-state potential surface for initial states with high quanta in the *trans*-bend and moderate quanta in the CC stretch than previous spectra have permitted. The new DF spectrum has a Franck-Condon (FC) envelope that extends to lower $\widetilde{X}$-state energy than the previous DF spectra. There

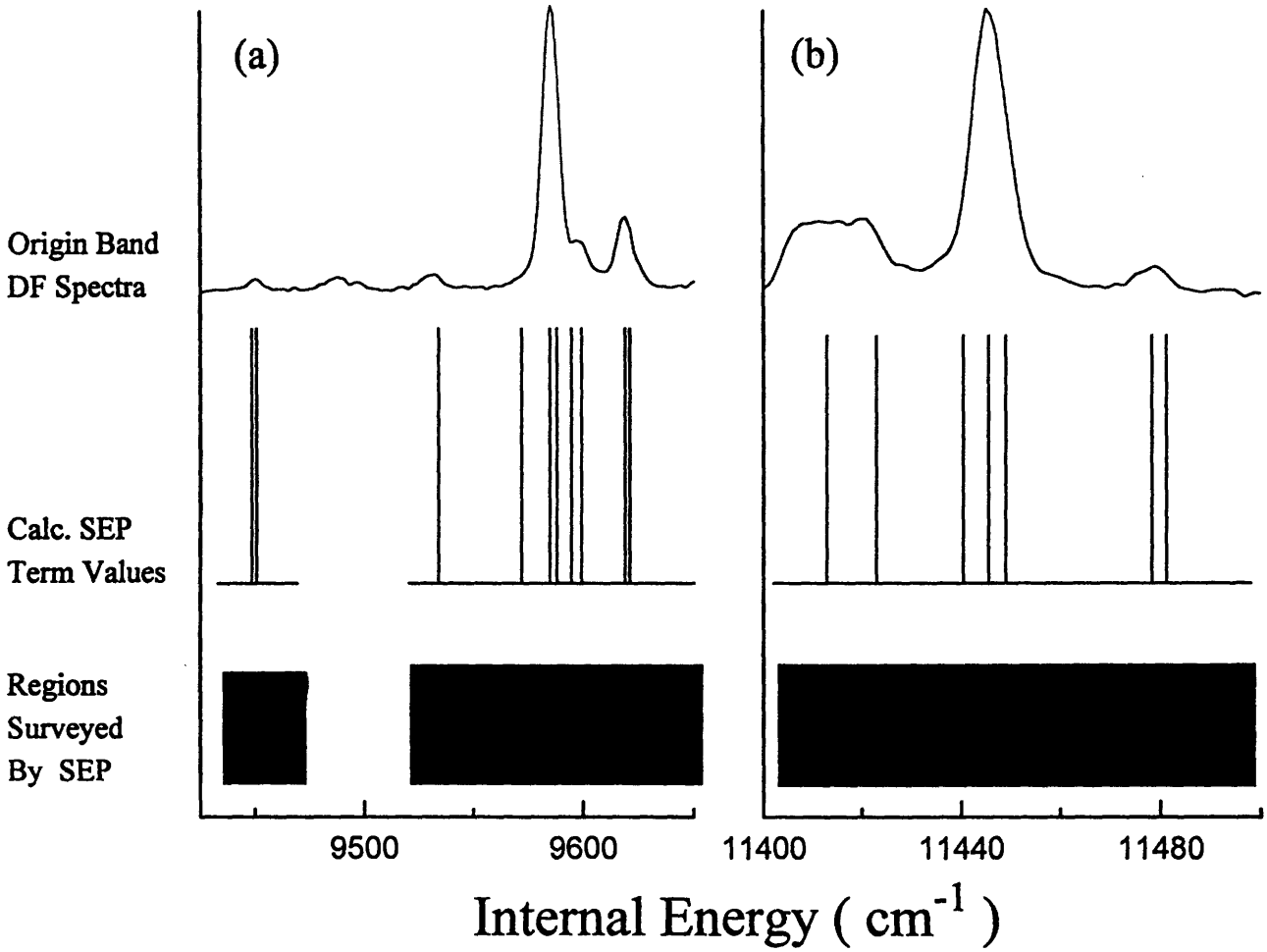

Figure 5.11: **a)** The regions previously examined by SEP at $E_{vib} \simeq 9,500$ cm^{-1}. A comparison of the calculated term values derived from the SEP analysis for states that could appear in the DF spectrum to the experimental Origin Band DF spectrum.
b) The region previously examined by SEP at $E_{vib} \simeq 11,400$ cm^{-1}. A comparison of the calculated term values derived from the SEP analysis for states that could appear in the DF spectrum to the experimental Origin Band DF spectrum.

a) Observed SEP Transitions in the 9,500 cm^{-1} region with Known $J_{\ell,\text{parity}}$

Obs. SEP Term Value	Intensity	$J^{exp}_{\ell,\text{parity}}$	B^{exp}_v	Calc. Term Values $2_{2,f}$	$1_{0,e}$	Obs. DF Term Value	Polyad Assignment	Zero-Order Bright State
9467.03	7%	$4_{2,f}$	1.162	9450.8	9448.6	9452.0	$[3,15]_g$	$(0,3,0,6,0)$
9478.61	31%	$5_{2,e}$						
9481.14	40%	$5_{0,e}$						
9492.60	22%	$6_{2,f}$						
9604.64	0.04	$4_{2,f}$	1.189	9588.0	9584.8	9587.3	$[1,15]_g$	$(0,1,0,12,0)$
9616.30	0.20	$5_{2,e}$						
9618.07	0.19	$5_{0,e}$						
9630.80	0.15	$6_{2,f}$						
9649.40	0.09	$5_{2,e}$	[a]	9621.1	9619.0	9620.9	$[1,15]_g$	$(0,1,0,12,0)$
9652.24	0.09	$5_{0,e}$						
9663.78	0.03	$6_{2,f}$						

[a]Used $B_{(0,1,0,12,0)} = B_0 - \sum_{i=1}^{5} \alpha_i v_i$ =1.1859(2) to calculate predicted Term Values

b) Observed SEP Transitions in the 9,500 cm^{-1} region with Unassigned $J_{\ell,\text{parity}}$

Obs. SEP Term Value	Intensity	If SEP State Is:	Calc. Term Value for $J_{\ell,\text{parity}}$	is:	Obs. DF Term Value	Polyad Assignment	Zero-Order Bright State
9627.91	0.11	$6_{2,f}$	$2_{2,f}$	9585.2	9587.3	$[1,15]_g$	$(0,1,0,12,0)$
		$5_{0,e}$	$1_{0,e}$	9594.7	9600.1		
		$5_{2,e}$	$2_{2,f}$	9599.4	9600.1		
9631.24	0.07	$6_{2,f}$	$2_{2,f}$	9588.5	9587.3	$[1,15]_g$	$(0,1,0,12,0)$
		$5_{0,e}$	$1_{0,e}$	9598.0	9600.1		
		$5_{2,e}$	$2_{2,f}$	9602.8	9600.1		
9664.20	0.02	$6_{2,f}$	$2_{2,f}$	9621.5	9620.9	$[1,15]_g$	$(0,1,0,12,0)$
		$5_{0,e}$	$1_{0,e}$	9631.0			
		$5_{2,e}$	$2_{2,f}$	9635.8			
9576.69		$6_{2,f}$	$2_{2,f}$	9534.0	9532.8	$[1,15]_g$	$(0,1,0,12,0)$
		$5_{0,e}$	$1_{0,e}$	9543.5			
		$5_{2,e}$	$2_{2,f}$	9548.2			
9600.40		$6_{2,f}$	$2_{2,f}$	9557.7		$[1,15]_g$	$(0,1,0,12,0)$
		$5_{0,e}$	$1_{0,e}$	9567.2	9570[a]		
		$5_{2,e}$	$2_{2,f}$	9571.9	9570[a]		

[a]Slight shoulder on peak 9587.3

Table 5.6: Observed SEP transitions in the 9,500 cm^{-1} region [28] and the corresponding peaks in the Origin Band DF Spectrum (all units in cm^{-1}).

Band	G_v^{exp}	B_v^{exp}	Calc. Term Values $2_{2,f}/1_{0,e}$	Matching DF Assignment
$1(\ell=0)$	11475.9	1.193	11478.3	11480.1
$1(\ell=2)$	11474.2	1.167	11481.2	11480.1
$2(\ell=0)$	11443.1	1.196	11445.5	11447.7
$2(\ell=2)$	11441.9	1.178	11449.0	11447.7
$3(\ell=2)$	11434.1	1.050	11440.4	
$4(\ell=2)$	11415.9	1.155	11422.9	11422.0
$5(\ell=2)$	11405.9	1.167	11412.9	11411.4

Table 5.7: Observed band origins and B_v values from fitted SEP transitions in the 11,400 cm^{-1} region [31] and the corresponding peaks in the Origin Band DF Spectrum (all units in cm^{-1}).

are *no nodes* in the $\widetilde{A}$-state zero-point vibrational wavefunction, and this allows features that were absent in the previous studies to be recovered. The increase in resolution is sufficient to discern fractionation at lower $\widetilde{X}$-state energies, where the initial IVR can be described by our $\hat{\mathbf{H}}^{\mathbf{R}}_{eff}$ model. In this chapter we have presented the analyses performed for levels with $E_{vib} \leq 10,000$ cm^{-1}. From the spectral intensity patterns originating from very high excitation in the *trans*-bend, the sign and approximate value of the only pure bend vibrational constant, $s^{h_2}_{45}$, previously undetermined [5] from pure bend states, was calculated to be -11(2) cm^{-1}. Our $\hat{\mathbf{H}}^{\mathbf{R}}_{eff}$ qualitatively describes the IVR pathways found in the Origin Band DF spectrum for zero-order bright states containing solely very high excitation in the *trans*-bend (up to $V_4 = 12$). In contrast, the zero-order bright states with one quantum in the CC stretch only match the $\hat{\mathbf{H}}^{\mathbf{R}}_{eff}$ model for *trans*-bend quanta $V_4 \leq 8$, indicating that a hitherto neglected stretch-bend or stretch-only resonance may be responsible for the discrepancy. Comparison of the Origin Band DF spectrum to previous SEP spectra has produced plausible rotational and vibrational character assignments for the transitions observed in the previous SEP spectra [27, 28, 31]. Building on what we have learned here, levels at higher E_{vib} previously described as *intrinsically unassignable* may soon yield their secrets as well.

References

[1] K. Yamanouchi, N. Ikeda, S. Tsuchiya, D. M. Jonas, J. K. Lundberg, G. W. Adamson, R. W. Field. *J.Chem.Phys.* **95**(9), 6330 (1991).

[2] D. M. Jonas, S. A. B. Solina, B. Rajaram, R. J. Silbey, R. W. Field, K. Yamanouchi, S. Tsuchiya. *J.Chem.Phys.* **99**(10), 7350 (1993).

[3] "*Fractionation*, or *fragmentation*, is defined to mean the complicated spectrum resulting from IVR. As opposed to *congestion*, a spectrum that looks complicated but NOT resulting from IVR." - Jon Hougen - Talk MH01, The Ohio State University International Symposium on Molecular Spectroscopy, June 14, 1993.

[4] A single sixth-order resonance, $K_{33,1244}$, has been reported by Smith and Winn [8]. This is probably an "accidental" resonance in the sense that the two levels in question are very close in energy, and, therefore a higher order (smaller resonance) term could efficiently transfer spectral intensity/zero-order character, as opposed to a "dynamical" resonance that is strong/active throughout the spectrum. Also, the effective Hamiltonian fit by Temsamani and Herman [7] showed that the intensity borrowing could also be explained by the extended net of fourth-order resonances listed in Table 5.2.

[5] J. Plíva. *J.Mol.Spectros.* **44**(1), 165 (1972).

[6] G. Strey, I. M. Mills. *J.Mol.Spectros.* **59**, 103 (1976).

[7] M. A. Temsamani, M. Herman. *J.Chem.Phys.* **102**(16), 6371 (1995).

[8] B. C. Smith, J. S. Winn. *J.Chem.Phys.* **89**(8), 4638 (1988).

[9] B. C. Smith, J. S. Winn. *J.Chem.Phys.* **94**(6), 4120 (1991).

[10] D. M. Jonas. *Spectroscopy of Vibrationally Hot Molecules: Hydrogen Cyanide and Acetylene.* Ph.D. thesis, Massachusetts Institute of Technology (1992).

[11] M. E. Kellman. *J.Chem.Phys.* **93**(9), 6630 (1990).

[12] M. E. Kellman, G. Chen. *J.Chem.Phys.* **95**(11), 8671 (1991).

[13] L. E. Fried, G. S. Ezra. *J.Chem.Phys.* **86**(7), 6270 (1987).

[14] ℓ is determined by the choice of K_a in the intermediate state($\ell = K_a \pm 1$). See [32].

[15] S. A. B. Solina, J. P. O'Brien, R. W. Field, W. F. Polik. "Unzipping Dispersed Fluorescence Spectra: An Unconventional Form of Franck-Condon Analysis Leads to Information about Dynamics." *in preparation.*

[16] S. A. B. Solina, J. P. O'Brien, R. W. Field, W. F. Polik. *Ber.Bunsenges.Phys.Chem.* **99**(3), 555 (1995).

[17] Although undetermined directly, s_{45} is not independent of $x_{tt'}$, $g_{tt'}$, r_{45} and $\alpha_t(t = 4,5; t' = 4,5)$. See [2,5].

[18] T. R. Huet, M. Herman, J. W. C. Johns. *J.Chem.Phys.* **94**, 3407 (1991).

[19] M. J. Bramley, S. Carter, N. C. Handy, I. M. Mills. *J.Mol.Spectros.* **157**(?), 301 (1993).

[20] A. B. McCoy, E. L. Sibert III. *J.Chem.Phys.* **95**(11), 3476 (1991).

[21] G. Amat, H. H. Nielson, G. Tarrago. *Rotation-Vibration of Polyatomic Molecules.* Marcel Dekker, Inc., New York, NY (1971).

[22] D. Papoušek, M. R. Aliev. *Molecular Vibrational-Rotational Spectra.* Elsevier Scientific Publishing Company, Amsterdam (1982).

[23] E. L. Sibert III, R. C. Mayrhofer. *J.Chem.Phys.* **99**(2), 937 (1993).

[24] J. A. Bentley, R. E. Wyatt, M. Menou, C. Leforestier. *J.Chem.Phys.* **97**(6), 4255 (1992).

[25] The number of combinations with repetitions of order N_s from 3 elements is $\tilde{C}(3,N_s) = \binom{N_s+2}{N_s} = \binom{N_s+2}{2}$.

[26] D. M. Jonas, S. A. B. Solina, B. Rajaram, R. J. Silbey, R. W. Field, K. Yamanouchi, S. Tsuchiya. *J.Chem.Phys.* **97**(4), 2813 (1992).

[27] E. Abramson, R. W. Field, D. Imre, K. K. Innes, J. L. Kinsey. *J.Chem.Phys.* **83**(2), 453 (1985).

[28] E. H. Abramson. *Molecular Acetylene in States of Extreme Vibrational Excitation.* Ph.D. thesis, Massachusetts Institute of Technology (1985).

[29] Due to slightly higher J, better sensitivity, and higher resolution (therefore, coupling over longer timescales is resolvable) weak SEP transitions may derive their intensity from axis-switching [26], Coriolis, or interpolyad dynamics.

[30] If a transition terminating in the $4_{2,f}$ rotational level was strong enough to detect, then the transition into the $6_{2,f}$ rotational level of the same vibrational state would also be easily detected.

[31] Y. Chen, S. Halle, D. M. Jonas, J. L. Kinsey, R. W. Field. *J.Opt.Soc.Am.B* **7**(9), 1805 (1990).

[32] J. K. G. Watson, M. Herman, J. C. Van Craen, R. Colin. *J.Mol.Spectros.* **95**(1), 101 (1982).

Chapter 6

Dynamics from the *Unzipping* Procedure

"Spectra to Dynamics" — that's the real problem, isn't it? How can one record a complicated spectrum like Figure 6.1a and from it infer the dynamics of the molecule? Figure 6.1a is complicated in the sense that the clues to the dynamics, are overlapped with one another. Would it not be nice if one could take a spectrum like Figure 6.1a and *unzip* it into regular progressions, as shown in Figure 6.1b, to be able to pull apart the information to facilitate an understanding of the dynamics? This chapter describes how one can record a set of dispersed fluorescence (DF) spectra of acetylene, unzip them, and reveal information about the vibrational energy flow dynamics on the S_0 surface.

6.1 The *Unzipping* Procedure

6.1.1 Motivation

Although acetylene is a linear tetratomic molecule of $D_{\infty h}$ point group symmetry in its electronic ground state equilibrium geometry, acetylene can isomerize to vinylidene which has C_{2v} symmetry, at about 16,000 to 17,000 cm^{-1} [1] of vibrational excitation. To try to sample the vinylidene region of the potential energy surface, and thereby the isomerization dynamics, one would attempt to record spectra in the energy and coordinate region near the isomerization barrier. The isomerization involves taking one hydrogen and moving it to the other side of the molecule. By naively inspecting the transition state [1], one might want to try to initially record spectra of very high quanta in the bends. Unfortunately, $E_{vib} \approx 16,000$ cm^{-1} requires 25 quanta of the bend, which is impossible to reach directly by any kind of overtone spectroscopy.

6.1.2 Polyads and the Choice of Bright States

In contrast to the linear and CC triple bonded ground state geometry, acetylene's first excited singlet electronic state, the $\widetilde{A}\,^1A_u$ state, has an equilibrium geometry that is *trans*-bent and has a nominal CC double bond. This results in Franck-Condon (FC) activity in very high quanta of the *trans*-bend, v_4, and moderate quanta in the CC stretch, v_2, for spectroscopic schemes that probe the ground state using the $\widetilde{A}$ state as an intermediate, such as DF and stimulated emission pumping(SEP).

These two particular FC active modes, v_2 and v_4, in addition to the particular set of active resonances found in the IR, Raman, overtone and SEP spectra given in Table 6.1,

lead to a *fortuitous coincidence* such that there will be **only one bright state per polyad**. This can be explained as follows. First, by inspection of the set of resonances in Table 6.1, or by simple linear algebra [2-5], it can be shown that there remain three conserved quantities or polyad numbers, $[N_s, N_{res}]^{\ell}$,

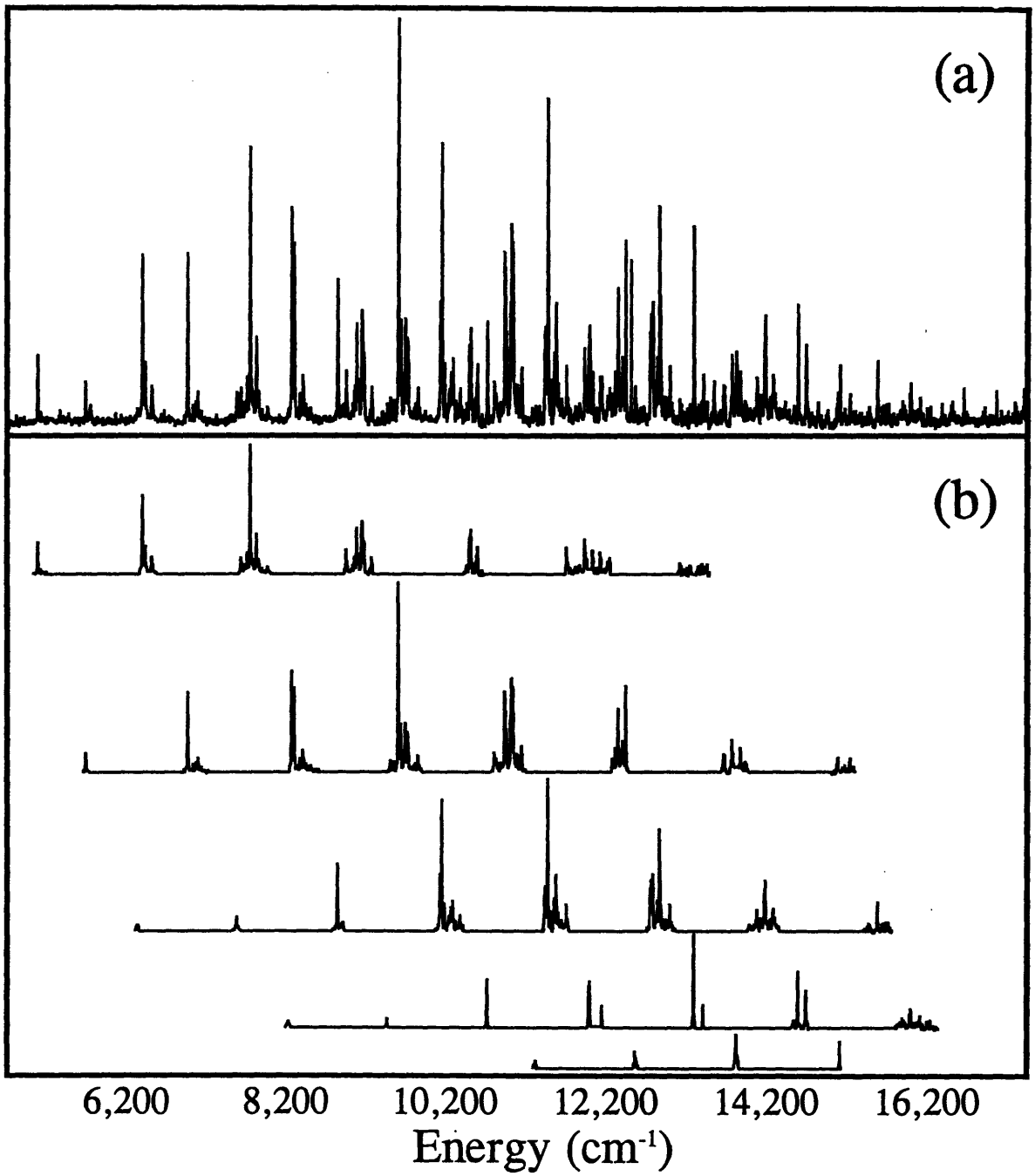

Figure 6.1: (a) Full Origin Band DF spectrum: complicated in the sense that the spectroscopic clues to the dynamics are overlapped with one another. (b) Unzipped Origin Band DF spectrum: the spectral features are now pulled apart to facilitate the understanding of the dynamics, revealing information about the vibrational energy flow in acetylene on the S_0 surface.

Anharmonic Resonances used in $\hat{\mathbf{H}}_{eff}$[a], $\mathrm{H}_{ij} = \langle v_i^{\ell_i} \vert \hat{\mathbf{H}}_{eff} \vert (v_i + \Delta v_i)^{(\ell_i + \Delta \ell_i)} \rangle$		Quantum Number Dependence of H_{ij}[b]
Bend only interactions:		
DD bend res. I	$\Delta v_4 = -\Delta v_5 = 2$	$\sqrt{(v_4 - l_4)^2 (v_5 - l_5 + 2)^2}$
DD bend res. II	$\Delta v_4 = -\Delta v_5 = 2$, $\Delta \ell_4 = -\Delta \ell_5 = \mp 2$	$\sqrt{(v_4 \pm \ell_4 - 2)(v_4 \pm \ell_4)(v_5 \pm \ell_5 + 2)(v_5 \pm \ell_5 + 4)}$
vibrational-ℓ-res.	$\Delta \ell_4 = -\Delta \ell_5 = \mp 2$	$\sqrt{(v_4 \pm \ell_4)(v_4 \mp \ell_4 + 2)(v_5 \mp \ell_5)(v_5 \pm \ell_5 + 2)}$
Stretch/Bend interactions:		
"2345" res.	$\Delta v_3 = -\Delta v_2 = -\Delta v_4 = -\Delta v_5 = 1$, $\Delta \ell_4 = -\Delta \ell_5 = \pm 1$	$\sqrt{(v_2)(v_3 + 1)(v_4 \pm \ell_4)(v_5 \mp \ell_5)}$
"1244" res.	$\Delta v_1 = -\Delta v_2 = -\frac{1}{2} \Delta v_4 = 1$	$\sqrt{(v_1 + 1)(v_2)(v_4^2 - l_4^2)}$
"1255" res.	$\Delta v_1 = -\Delta v_2 = -\frac{1}{2} \Delta v_5 = 1$	$\sqrt{(v_1 + 1)(v_2)(v_5^2 - l_5^2)}$
"1345" res.	$\Delta v_1 = -\Delta v_3 = \Delta v_4 = -\Delta v_5 = 1$, $\Delta \ell_4 = -\Delta \ell_5 = \pm 1$	$\sqrt{(v_1 + 1)(v_3)(v_4 \pm \ell_4 + 2)(v_5 \mp \ell_5)}$
Stretch only interactions:		
DD stretch res.	$\Delta v_1 = -\Delta v_3 = 2$	$\sqrt{(v_1 + 1)(v_1 + 2)(v_3)(v_3 - 1)}$

[a] See [5, 18]
[b] See [5, 14–17]

Table 6.1: Set of scalable resonances used in the global treatment of the IR, Raman, overtone and SEP data for the standard coupled normal mode Hamiltonian.

where:

$$N_s = v_1 + v_2 + v_3$$
$$N_{res} = 5v_1 + 3v_2 + 5v_3 + v_4 + v_5$$
$$\ell = \ell_4 + \ell_5.$$

This means that the traditional spectroscopic coupled harmonic oscillator basis set for acetylene is effectively block diagonalized into groups of zero-order states or "polyads" where the set of resonances, Table 6.1, connects zero-order states *within* each polyad but never *between* polyads. The polyad numbers provide a unique name for each polyad as well as a recipe for automatically setting up individual polyad blocks in an effective Hamiltonian matrix. Second, the symmetric CH stretch (ν_1), the antisymmetric CH stretch (ν_3) and the *cis*-bend(ν_5) are FC inactive, whereas the CC stretch(ν_2) and the *trans*-bend(ν_4) are FC active. This defines the set of zero-order bright states, or "chromostates", for SEP or DF spectra as the set of $(v_1, V_2, v_3, V_4, v_5)$'s where v_1, v_3 and v_5 are held constant and V_2 and V_4 are variable [6]. Finally, by inspection of the definitions of $[N_s, N_{res}]$, it is impossible to find more than one (V_2, V_4) pair with the same (v_1, v_3, v_5) for a given $[N_s, N_{res}]$. Therefore, there is only one bright state per polyad in the DF spectrum *as long as the polyad numbers remain good.* The polyad numbers will be conserved as long as all previously undetected resonances only connect states within a polyad and not between polyads.

The pattern formed in the DF spectrum for each polyad is the distribution of the intensity of the zero order bright state, or chromostate, among the ground state molecular eigenstates. Therefore, the intensity pattern within each polyad is solely a function of the ground state resonances, or dynamics. By comparing DF spectra from different intermediate states that prepare the same set of chromostates, but in which the relative intensities of the different chromostates vary, the intensity pattern *within each polyad* will be the same in each spectrum, but the relative intensity of each polyad pattern as a whole will vary from one spectrum to the next. By taking advantage of this intrapolyad intensity invariance, the polyads may be separated, *i.e.*, the DF spectrum may be **unzipped** into its component polyads.

The fact that the DF spectrum can be unzipped also serves as a verification that the polyad numbers remain good. By comparing our $2\nu_3'$ and Origin Band DF spectra [7] and Yamanouchi's $3\nu_3'$ DF spectrum [8], these DF spectra, which prepare zero-order bright states with very high excitation in the *trans*-bend (up to $v_4 = 20$) and moderate excitation of CC stretch (up to $v_2 = 4$), can be unzipped up to *at least* 16,400 cm^{-1}. We are in the process of collecting more spectra to determine how far up in E_{vib} the unzipping procedure is viable. So far we conclude that the three polyad numbers, $[N_s, N_{res}]^{\ell}$, remain good for initial excitation very high in *trans*-bend and moderate CC stretch, at least up to 16,400 cm^{-1} .

This is interesting because one would expect to lose all conserved vibrational quantities when acetylene isomerizes to vinylidene. A normal mode basis set meant to describe a linear tetratomic molecule should be ill-suited to describing the energy levels of vinylidene or the transition state. Locating the E_{vib} (and its dependence on the nature of the intermediate state) at which one loses the ability to unzip the DF spectrum could provide a way of characterizing the adiabatic barrier to vinylidene. One could compare the current series of DF spectra to a series with one added quantum in the antisymmetric CH stretch or symmetric CH stretch and thereby systematically map regions of the potential energy surface.

6.2 Franck-Condon Intensity Trends

Since there is only one bright state per polyad, this system provides a nice opportunity to examine FC intensity trends, once a DF spectrum has been unzipped. In Figure 6.2a the unzipped polyads from the Origin Band DF spectrum are arranged as progressions in v_4 such that each row has constant v_2 and each column has constant v_4. By inspection of Figure 6.2a or the plot of integrated intensity per polyad, Figure 6.2b, each progression in v_4 has the same smooth Gaussian-like intensity profile for each value of v_2. The same is also true if the polyads are plotted as progressions in v_2. As expected, there are no nodes in the either the CC stretch or *trans*-bend unzipped progressions, since the intermediate for the Origin Band

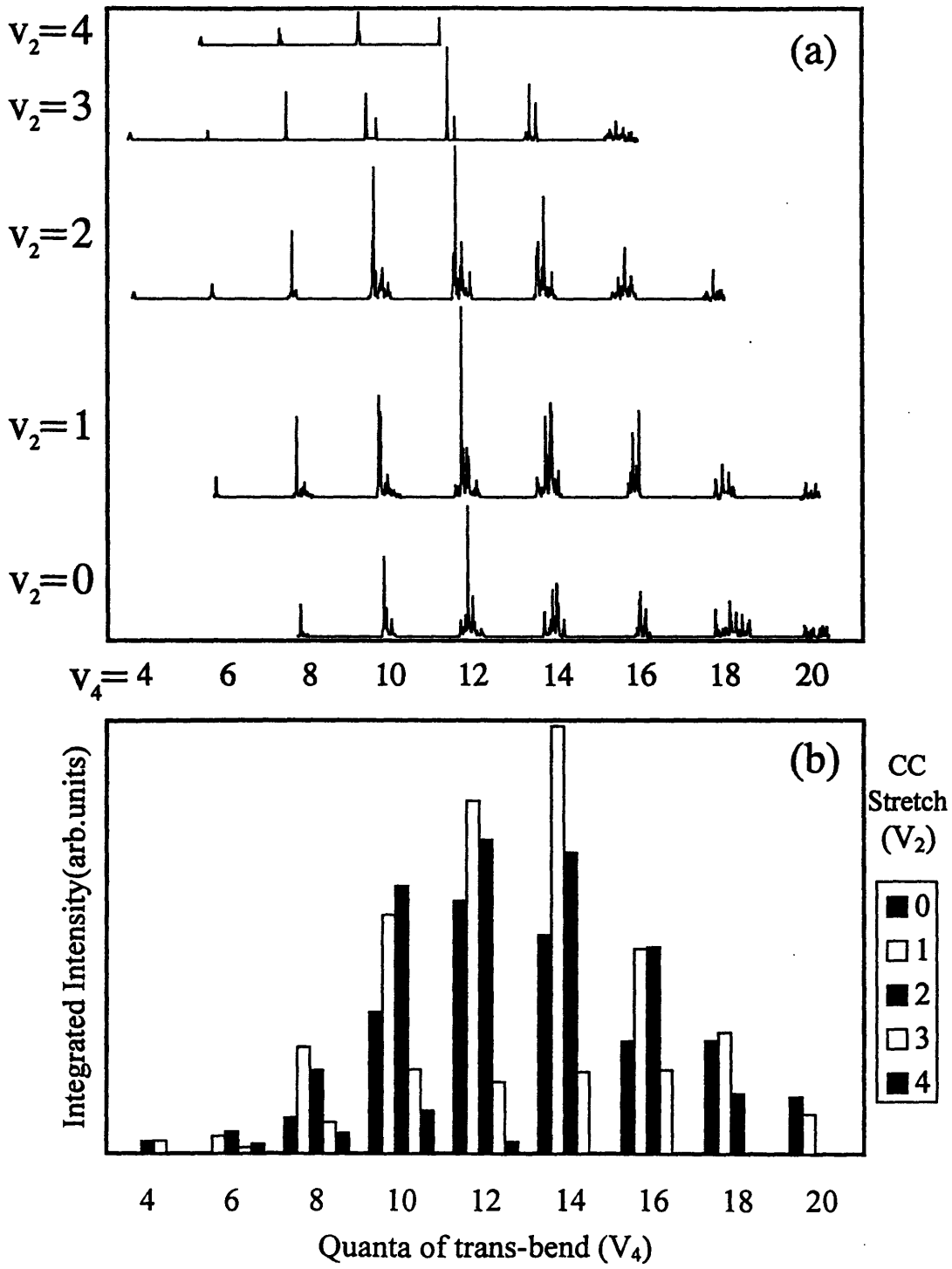

Figure 6.2: (a) Unzipped polyads from the Origin Band DF spectrum arranged as progressions in v_4 such that each row has constant v_2 and each column has constant v_4. (b) Integrated intensity for each polyad from the Origin Band DF spectrum.

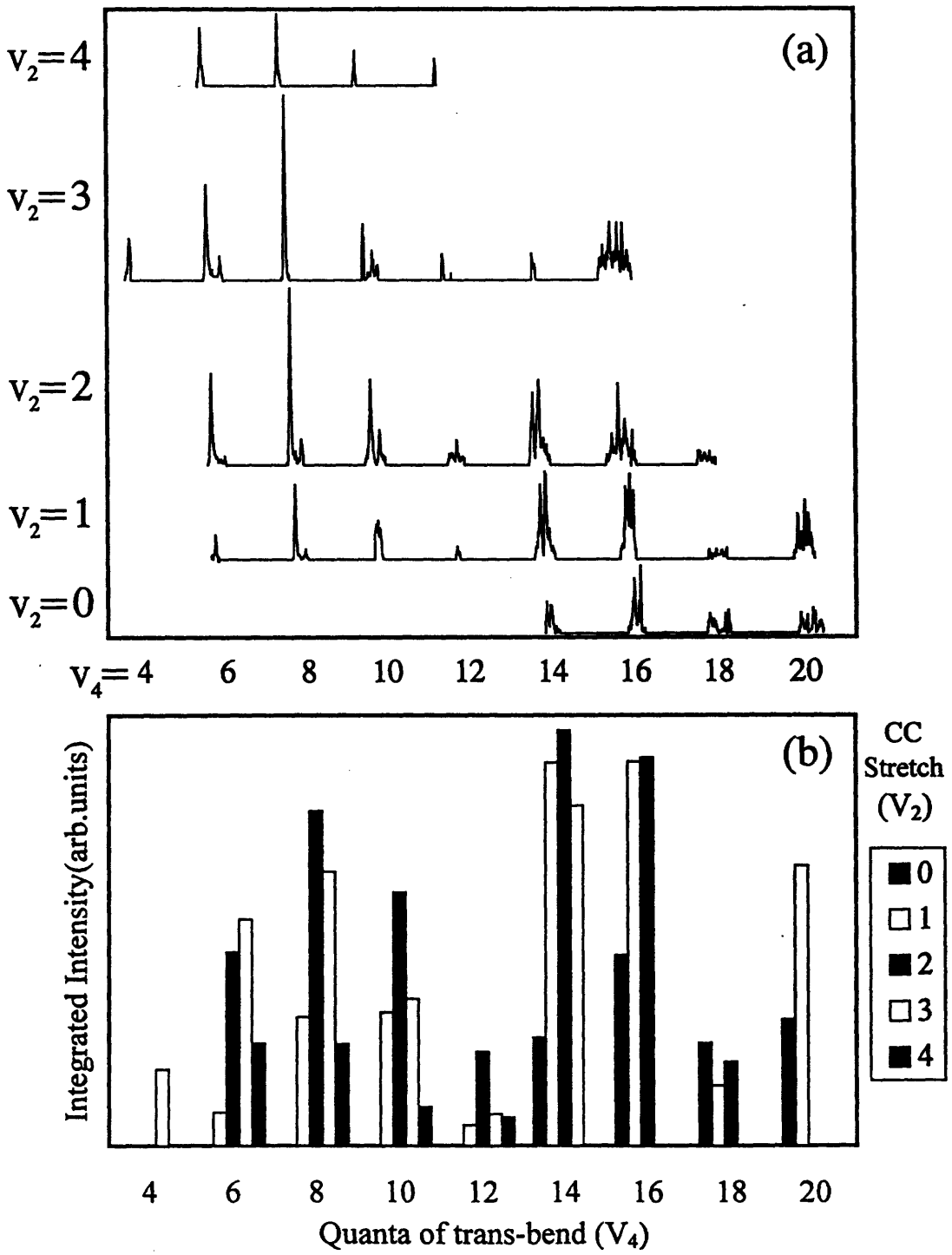

Figure 6.3: (a) Unzipped polyads from the $2\nu_3'$ DF spectrum arranged as progressions in v_4 such that each row has constant v_2 and each column has constant v_4. (b) Integrated intensity for each polyad from the $2\nu_3'$ DF spectrum. *Note the nodes at* $v_4 = 12$ *and* 18.

DF spectrum, the zero-point level, should have no nodes in its $\widetilde{A}$ state vibrational wavefunction. On the contrary, the same plots for the DF spectrum recorded from $2\nu_3'$ in the $\widetilde{A}$ state, Figure 6.3,

show two distinct nodes in the *trans*-bend progression at $v_4 = 12$ and $v_4 = 18$, and no nodes in the v_2 (CC stretch) progression, as is expected for an intermediate that has two nodes in its *trans*-bend wavefunction [9]. As can be seen, unzipping the DF spectrum to facilitate arranging the polyads and comparing the polyad intensities in progressions, can make the polyad progressions in the $\widetilde{A} \rightarrow \widetilde{X}$ band system prime candidates for tests of polyatomic molecular FC intensity calculations.

6.3 IVR trends from Unzipped Polyads

Intramolecular vibrational redistribution (IVR) is manifested in spectra by the degree of fractionation of the zero-order state among the molecular eigenstates. Once the DF spectrum is unzipped, two trends in IVR become apparent. For the particular chromostates selected in these experiments, IVR increases with increasing excitation in the *trans*-bend, ν_4, and, surprisingly, IVR decreases with increasing excitation in the CC stretch, ν_2. This can be seen by inspection of Figure 6.4 which displays the unzipped polyads arranged as progressions in ν_4, where the rows are constant v_2 and columns constant v_4. The extent of IVR, or fractionation, increases across a row, increasing v_4, but the fractionation decreases up a column, increasing v_2. For each row, constant v_2, v_4 increases to the right, and for each column, constant v_4, v_2 increases up a column; therefore, energy increases to the right and up a column. Since the number of states per polyad and the density of states per polyad both increase with increasing v_2 and v_4, see Figure 6.5, one would expect for statistical reasons to observe an increase in IVR with increasing v_4, consistent with the spectrum, and increasing v_2, contrary to the spectrum. As opposed to statistical expectations, *both* IVR trends turn out to be local effects. The extent of IVR, for the initial states prepared in these experiments, is controlled by the strength of the off-diagonal matrix elements, H_{ij}, and the zero-order energy differences, ΔE, of the first few initial resonance steps, or tiers, and is independent of the number or density of states of the statistical bath many tiers away [10].

6.3.1 IVR as a Function of v_4

The IVR trends can be understood by inspection of the structure, ΔE and H_{ij}, of the effective Hamiltonian, $\hat{\mathbf{H}}_{eff}$, used in our acetylene work [5, 7, 11]. An effective Hamiltonian was constructed from a normal mode basis set with diagonal anharmonicities and off-diagonal coupling [12, 13]. The quantum number dependence of the scalable off-diagonal matrix elements is given in Table 6.1, and the fitted constants in [5, 14–18]. In these DF spectra, the zero-order bright state, $(0, V_2, 0, V_4, 0)$, lies at the low energy extreme of its polyad as can be seen from the location of the strongest peak in each $v_4 = 8, 10$ and 12 polyad in Figure 6.4 and the zero-order energy level diagrams in Figures 6–8. The nearest neighbor intrapolyad zero-order state to $(0, V_2, 0, V_4, 0)$ is $(0, V_2, 0, V_4 - 2, 2)$, which also happens to be one to which the bright state can couple most strongly via a Darling-Dennison (DD) bend resonance, see Table 6.1 and the diagram in Figure 6.6, with a typical matrix element and zero-order energy denominator, $H_{ij}/\Delta E \approx 70/10$ cm^{-1} at $v_4 = 14$. Entering the next tier, by again applying the DD bend resonance, connects $(0, V_2, 0, V_4 - 2, 2)$ to $(0, V_2, 0, V_4 - 4, 4)$, with $H_{ij}/\Delta E \approx 120/30$ cm^{-1}, and so on, forming a "DD bend stack". The energy spacing and coupling strength near the low energy end of each polyad is dominated by these stacks. These DD bend stacks, $\{(0, V_2, 0, V_4, 0), (0, V_2, 0, V_4 - 2, 2), \dots\}$ and $\{(1, V_2 - 1, 0, V_4 - 2, 0), (1, V_2 - 1, 0, V_4 - 4, 2), \dots\}$, *etc.*, see diagram in Figure 6.8, are interconnected by a web of resonances that are not as strong, typically $H_{ij}/\Delta E \approx 10/30$cm^{-1}. The reason why IVR, and therefore the polyad fractionation, increases with increasing v_4 is twofold. First, the DD bend matrix element is roughly proportional to $\sqrt{(v_4)^2(v_5 + 2)^2}$, see Table 6.1, and increasing v_4 increases H_{ij}. Second, since $\omega_4^0(610\text{ cm}^{-1})$ is less than $\omega_5^0(729\text{ cm}^{-1})$ BUT x_{44}^0 is positive$(+3.0\text{ cm}^{-1})$ and x_{55}^0 is negative(-2.3 cm^{-1}) [5], the ΔE's between successive members of the DD bend stacks decrease as v_4 increases! The DD bend stacks are compressing while the matrix elements are increasing, see Figure 6.6, until the crossing of the zero-order energies, E^0, as a function of (ω_4^0, x_{44}^0) and (ω_5^0, x_{55}^0) occurs around $v_4 = 16 - 18$ [5]. These effects dramatically increase the IVR as one increases v_4.

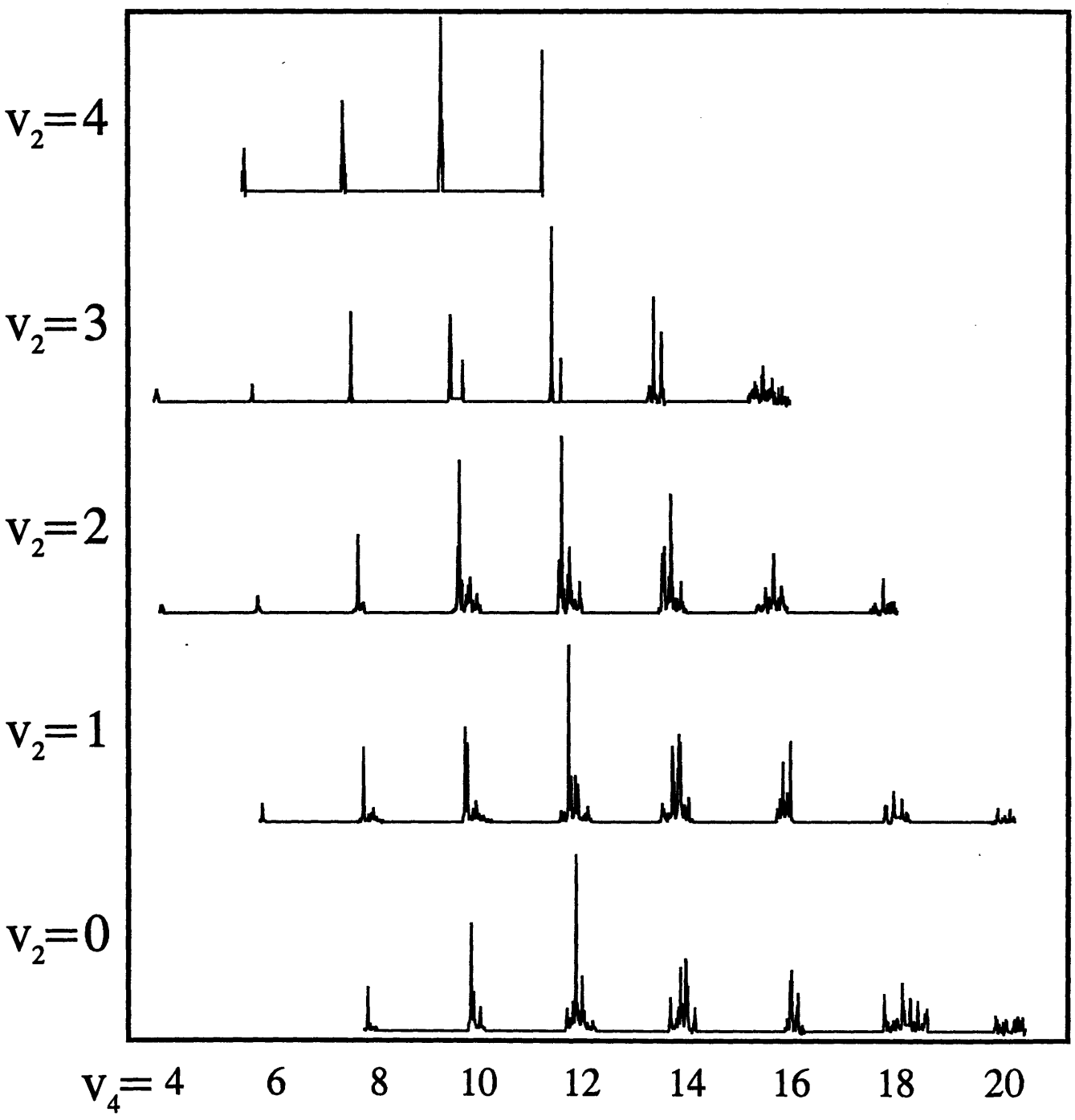

Figure 6.4: Unzipped polyads from the Origin Band DF spectrum arranged in progressions of v_4 such that each row has constant v_2 and each column constant v_4. Note that IVR, or fractionation, increases with **increasing v_4 and decreasing v_2**

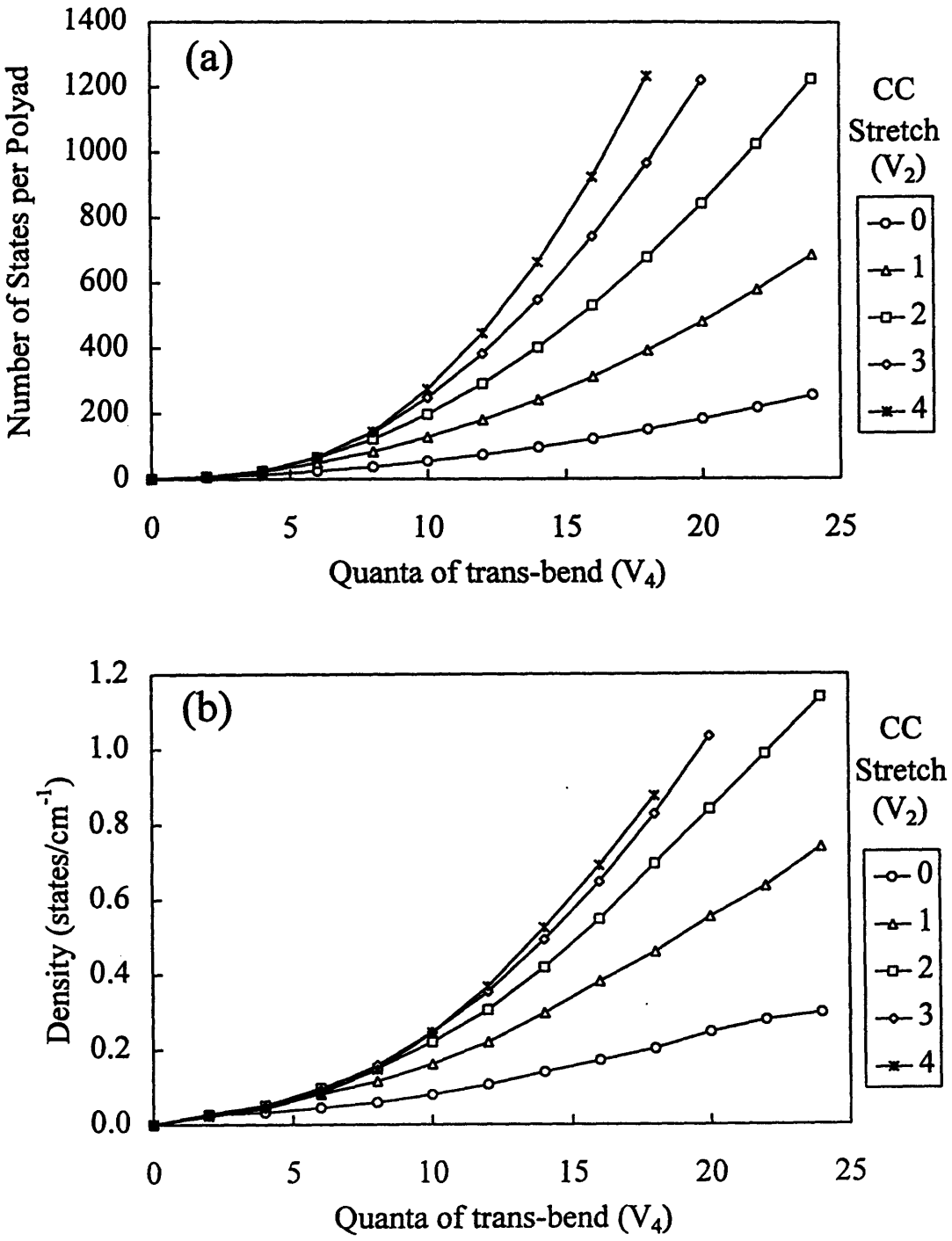

Figure 6.5: (a) The number of states within each polyad as a function of v_4 and v_2 of the bright state. (b) The density of states within each polyad as a function of v_4 and v_2 of the bright state.

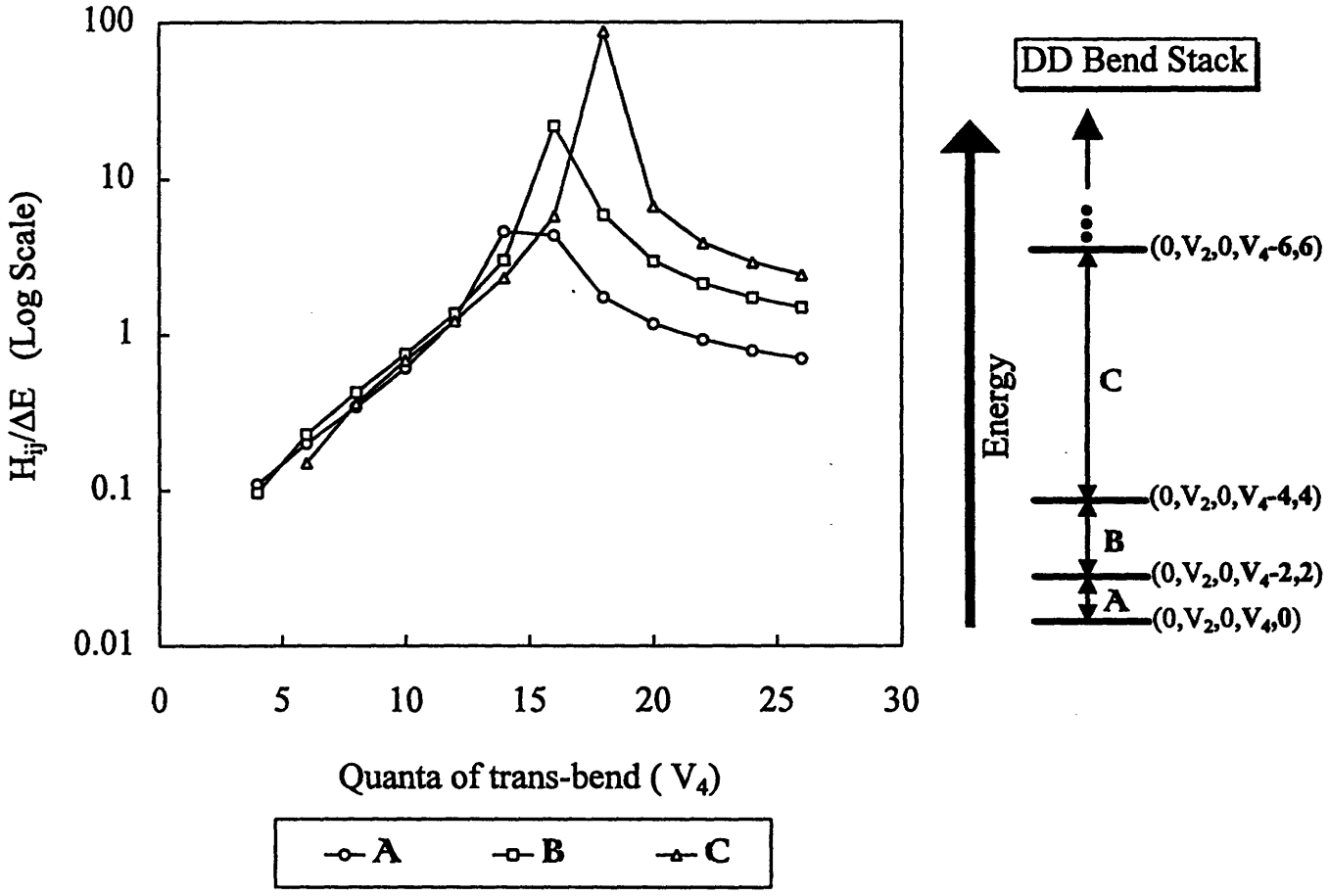

Figure 6.6: Within a DD bend stack, H_{ij} increases and ΔE decreases with increasing v_4 until the crossing of the zero-order energies, E^0, as a function of (ω_4^0, x_{44}^0) and (ω_5^0, x_{55}^0) around $v_4 = 16 - 18$.

6.3.2 IVR as a Function of v_2

Previous workers [5] had noticed that by inspection of the definition of the polyad numbers, $[N_s, N_{res}]^\ell$, one could immediately deduce that polyads with $N_s = 0$ contain states which have excitation purely in the bend, *i.e.*, no stretches. In other words, if energy were placed in these polyads, the excitation would stay purely in the bends and *never* flow into the CC or CH stretches. On the contrary, polyads with $N_s > 0$ allow one access to a larger range of motion and a larger region of phase space, *i.e.*, a larger density of states and number of states per polyad, see Figure 6.5. In this sense, initial excitation of both the CC stretch and the *trans*-bend, as opposed to *trans*-bend alone, could be seen as an ON/OFF switch to IVR. Since the DF spectrum can now be unzipped, the actual fractionation of the polyads for a wide range of initial excitation in the CC stretch and the *trans*-bend can be examined. Therefore, the *extent* to which IVR is affected in regard to excitation of the CC stretch can be investigated. As can be seen in Figure 6.4, too much CC stretch reduces IVR for the initial states probed here, which have very high excitation in the *trans*-bend and moderate excitation in the CC stretch.

Why does increasing v_2 *decrease* IVR? Since $x^0_{24} = -13$ cm^{-1} and $x^0_{25} = -2$ cm^{-1} [5], as v_2 increases the DD bend matrix element does not change, but the ΔE's change rapidly. For example, the first DD bend resonance, connecting the bright state, $(0, V_2, 0, V_4, 0)$, to $(0, V_2, 0, V_4 - 2, 2)$, has $H_{ij}/\Delta E \approx 70/10$ cm^{-1} at $v_2 = 0$, but $H_{ij}/\Delta E \approx 70/80$ cm^{-1}at $v_2 = 4$, see Figure 6.7.

The next DD bend resonance, connecting $(0, V_2, 0, V_4 - 2, 2)$ to $(0, V_2, 0, V_4 - 4, 4)$, has $H_{ij}/\Delta E \approx 120/30$ cm^{-1}at $v_2 = 0$, but $H_{ij}/\Delta E \approx 120/160$ cm^{-1}at $v_2 = 4$, and so on, see Figure 6.7. The DD bend resonance stacks are pulling apart, or more precisely, the bright state, which is at the low energy end of the polyad, is decreasing in energy faster than the rest of the stack, thus turning off the IVR. The effect of the resonances that interconnect the DD bend stacks also becomes weaker for two reasons. First, the entire DD bend stack containing the bright state as a whole pulls away from the other DD bend stacks, because the DD stack with the chromostate contains the most quanta in bend and CC stretch. Second, although the H_{ij}'s between the DD stacks increase roughly in proportion to $\sqrt{v_2}$, see Table 6.1, the H_{ij}'s do not increase rapidly enough to compensate for the increase in ΔE, see Figure 6.8. These effects together contribute to reducing IVR in acetylene when v_2 increases for the initial states probed here, very high excitation in the *trans*-bend and moderate excitation in the CC stretch.

6.4 Conclusion

Dispersed Fluorescence spectra of acetylene have been recorded and unzipped, through a fortuitous coincidence of FC active modes and active anharmonic resonances, thereby pictorially revealing the key factors controlling the vibrational dynamics on the acetylene S_0 surface. When energy is placed into very high excitation of the *trans*-bend and moderate excitation of the CC stretch, three approximately conserved quantities survive, *i.e.*, no trace of the expected total breakdown of vibrational constants of motion due to energetic access to the vinylidene isomer is observed for vibrational energies up to at least 16,400 cm^{-1}. Unzipping the DF spectrum reveals the FC intensity profiles for the acetylene $\tilde{A} \rightarrow \tilde{X}$ system with two FC active modes. Also, the unzipped DF spectrum clearly demonstrates that IVR increases within a polyad by increasing *trans*-bend, v_4, and by decreasing CC stretch, v_2. Increasing IVR with increasing v_4 or decreasing v_2, are both cases where the first few resonance tiers play the dominant role in controlling IVR for the initial states prepared in these experiments, very high excitation in the *trans*-bend and moderate excitation in the CC stretch.

References

[1] M. M. Gallo, T. P. Hamilton, H. F. Schaefer III. *J.Amer.Chem.Soc.* **112**(24), 8714 (1990). and references cited therein.

[2] M. E. Kellman. *J.Chem.Phys.* **93**(9), 6630 (1990).

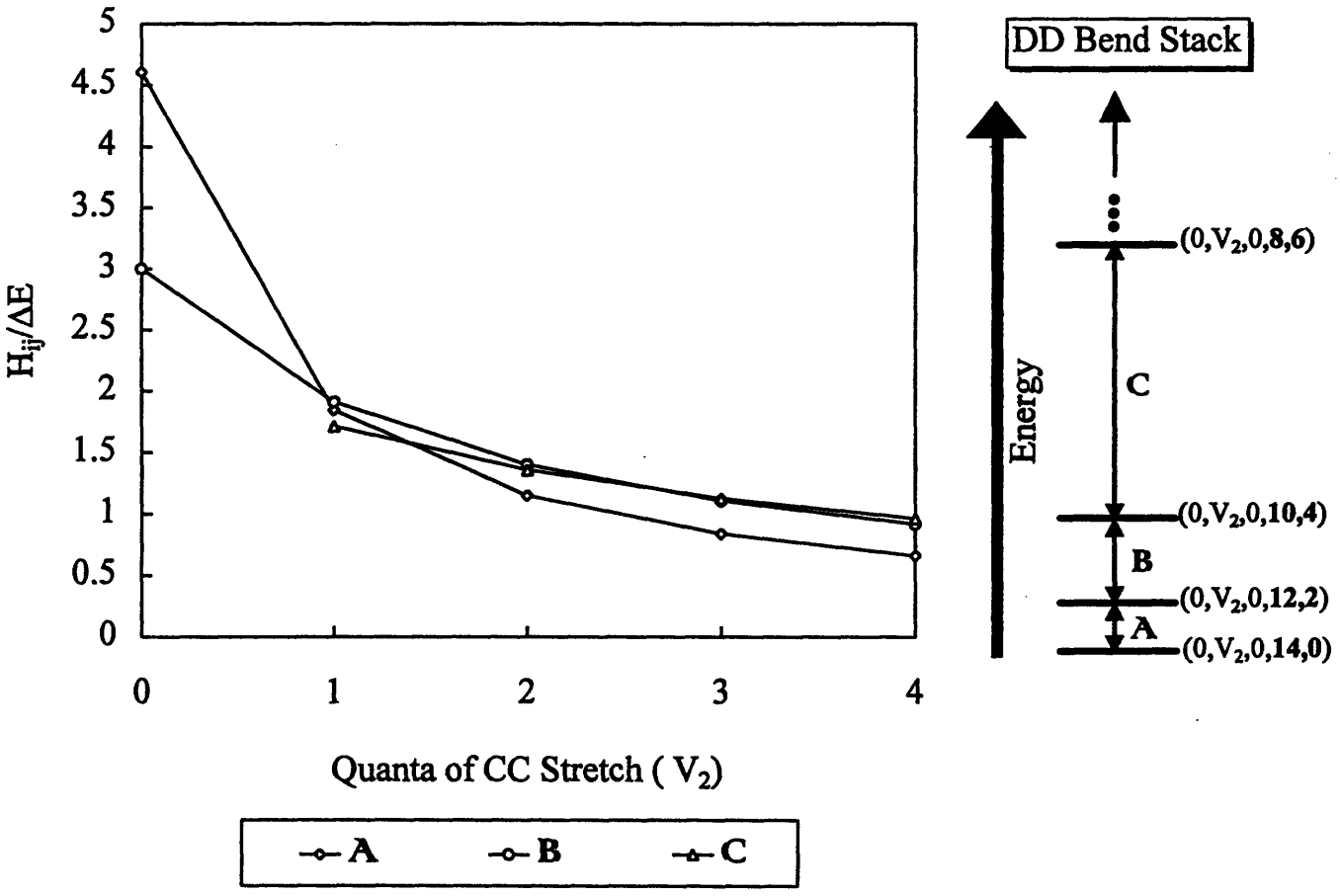

Figure 6.7: Within a DD bend stack, H_{ij} increases but ΔE increases more rapidly with increasing v_2 resulting in a reduction of $H_{ij}/\Delta E$.

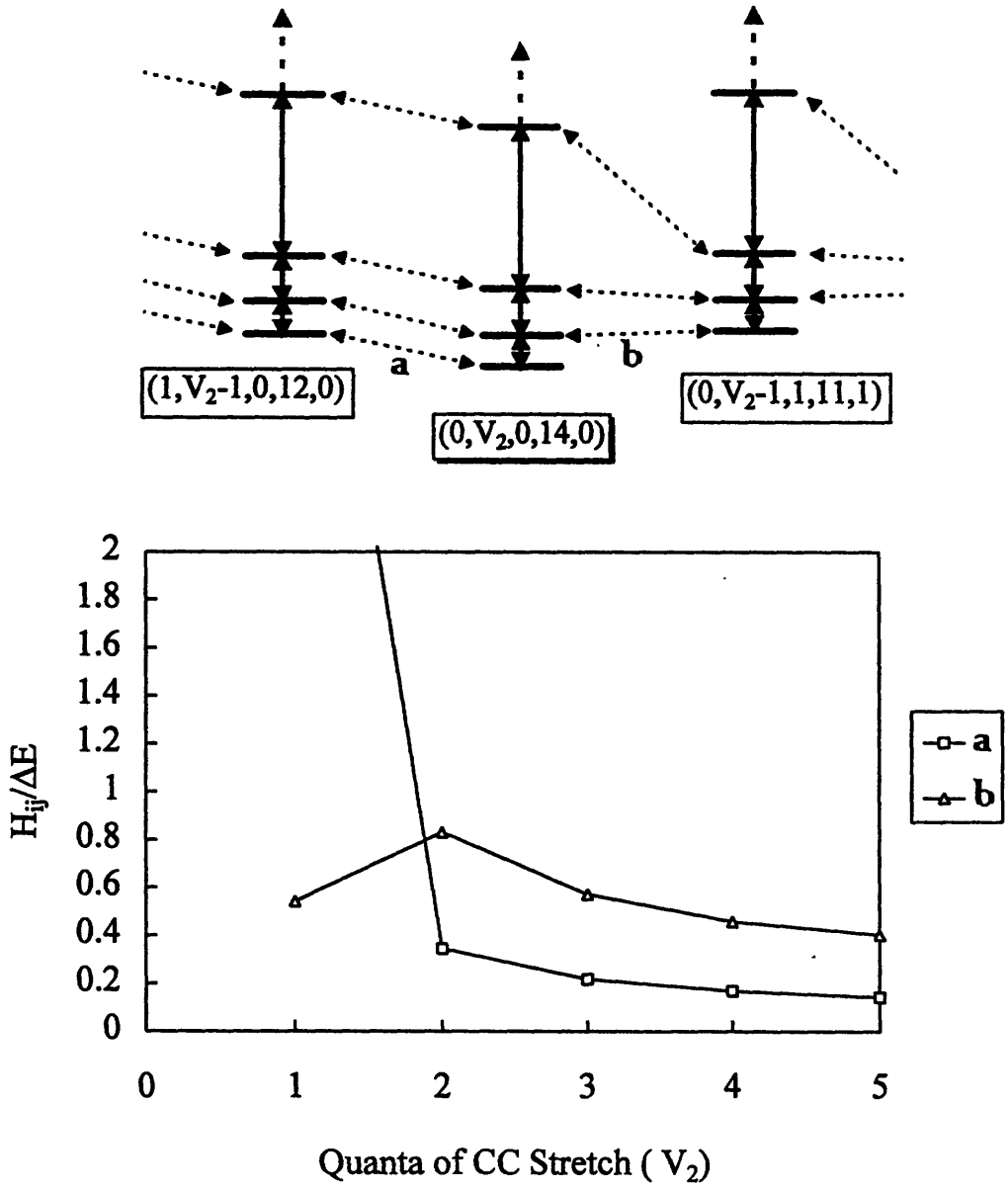

Figure 6.8: The entire DD bend stack containing the bright state as a whole pulls away from the other DD bend stacks(ΔE increases) as v_2 increases, because the DD stack with the chromostate contains the most quanta of both bend and CC stretch. Although H_{ij} between stacks increase with increasing v_2, H_{ij} does not increase rapidly enough to compensate for the increase in ΔE.

[3] M. E. Kellman, G. Chen. *J.Chem.Phys.* **95**(11), 8671 (1991).

[4] L. E. Fried, G. S. Ezra. *J.Chem.Phys.* **86**(7), 6270 (1987).

[5] D. M. Jonas, S. A. B. Solina, B. Rajaram, R. J. Silbey, R. W. Field, K. Yamanouchi, S. Tsuchiya. *J.Chem.Phys.* **99**(10), 7350 (1993).

[6] ℓ is determined by the choice of K_a in the intermediate state. See [19].

[7] S. A. B. Solina, J. P. O'Brien, R. W. Field, W. F. Polik. *J.Phys.Chem.* **100**(19), XXX (1996).

[8] K. Yamanouchi, N. Ikeda, S. Tsuchiya, D. M. Jonas, J. K. Lundberg, G. W. Adamson, R. W. Field. *J.Chem.Phys.* **95**(9), 6330 (1991).

[9] In the $\widetilde{A}$ state the *trans*-bend is ν_3', whereas in the $\widetilde{X}$ state the *trans*-bend is ν_4.

[10] A. A. Stuchebrukhov, R. A. Marcus. *J.Chem.Phys.* **98**(8), 6044 (1993).

[11] D. M. Jonas, S. A. B. Solina, B. Rajaram, R. J. Silbey, R. W. Field, K. Yamanouchi, S. Tsuchiya. *J.Chem.Phys.* **97**(4), 2813 (1992).

[12] G. Amat, H. H. Nielson, G. Tarrago. *Rotation-Vibration of Polyatomic Molecules.* Marcel Dekker, Inc., New York, NY (1971).

[13] D. Papoušek, M. R. Aliev. *Molecular Vibrational-Rotational Spectra.* Elsevier Scientific Publishing Company, Amsterdam (1982).

[14] J. Plíva. *J.Mol.Spectros.* **44**(1), 165 (1972).

[15] B. C. Smith, J. S. Winn. *J.Chem.Phys.* **89**(8), 4638 (1988).

[16] B. C. Smith, J. S. Winn. *J.Chem.Phys.* **94**(6), 4120 (1991).

[17] G. Di Lonardo, P. Ferracuti, L. Fusina, E. Venuti. *J.Mol.Spectros.* **164**(1), 219 (1994).

[18] Q. Kuo, G. Guelachvili, M. Abbouti Temsamani, M. Herman. *Can.J.Phys.* **72**(11&12), 1241 (1994).

[19] J. K. G. Watson, M. Herman, J. C. Van Craen, R. Colin. *J.Mol.Spectros.* **95**(1), 101 (1982).

Chapter 7

Hierarchical Analysis of the Acetylene Dispersed Fluorescence Spectra

The reader is highly encouraged to peruse the article "Hierarchical Analysis of Molecular Spectra," [1] by Mike Davis who developed this very interesting new method for extracting dynamical information from spectra. Many thanks to Mike whose method is already providing some very interesting insights into acetylene dynamics.

Spectra are the only windows that we have onto the dynamics of molecules. From spectra we try to infer information about the potential energy surface to ask questions such as: Where does energy go when we place it in a specific location in the molecule and how fast?

7.1 Traditional Analysis Methods for Spectra

The time honored method of extracting information from a spectrum entails fitting the peaks (in general, just the peak positions) to a spectroscopic Hamiltonian, *i.e.* a polynomial expansion in some set of quantum numbers with or without coupling between the states. The essential problem with this method of extracting information from the spectrum is that a spectrum may be too complicated to attempt a spectroscopic fit.

On the flip side, statistical analysis methods [2–4], such as $P(S)$, Δ_3 and Σ^2, were created in an attempt to extract even a minute amount of information from hopelessly complicated spectra. The drawbacks of these statistical methods are twofold. First, these statistical measures reduce the information in spectra containing thousands of lines to only a few numbers. Obviously an enormous amount of useful information in these spectra is not recovered. Second, these measures only use either the peak intensities OR the peak positions, never both. Why is this a problem? Consider the following example: two pairs of peaks that have the same frequency separation, but set A has a 100:1 intensity ratio and set B has a 50:50 intensity ratio. According to the frequency based measures, these two pairs are the same, but obviously from a molecular viewpoint, set A reveals a weaker coupling than set B. The converse example (two pairs of peaks both with 50:50 intensity ratios, but the frequency separation in set C is ten times that of set D) would be described by the same value for the intensity measures, even though the coupling in set C must be much stronger than in set D to cause intensity to be transferred over a wider frequency range.

Clearly for the case of intramolecular vibrational energy redistribution (IVR) in molecules, the hallmark of which is fractionation [5] in the spectra, any method that extracts information from the spectrum should include BOTH the intensities and the frequencies.

7.2 Hierarchical Analysis

Hierarchical analysis is a method for characterizing spectra that uses both the energies and intensities in the spectrum. Furthermore, hierarchical analysis is a method that extracts information about timescales in the spectrum, a quantity of central interest in the study of IVR: when and how fast does energy flow, and are there different timescales of energy flow. Hierarchical analysis extracts in a natural manner a "tree" from a spectrum, and then measures from classification theory and multivariate analysis can be run on this tree to extract timescale information, *e.g.* how many distinct timescales, how strong is the separation between timescales, where in the spectrum do these timescales appear, and so on.

Hierarchical analysis is not new. It is used in many forms in a wide variety of scientific disciplines, including protein marker correlations in biology to determine taxonomy, *e.g.* is a crayfish more closely related to a cow or a bee. Any area of study that requires measures for questions such as how are different sets of things grouped, is treading in an area of mathematics called classification theory. The hallmark of IVR in spectra is fractionation, *i.e.* clumps of obviously related lines. We, as chemists, want to be able to apply measures to these clumpings, to compare them and to extract timescale information. Hierarchical analysis allows us to do that.

7.2.1 Generating a Tree from a Spectrum

Quantum Mechanics encodes time information in a frequency domain spectrum. Via the uncertainty principle, a spectrum is a snapshot of all the dynamics that a system undergoes from $t = 0$ until $t = \tau_{res}$ (a time determined by the resolution of the spectrum). A lower resolution spectrum does not follow the evolution of the system to evolve vary long, very much like a snapshot taken close to the beginning of a race where the runners are still closely packed and have not yet had the time to spread out. A higher resolution spectrum may show much more fractionation than a lower resolution spectrum, much like a later snapshot in the race where the runners have had more time to spread out.

A fictitious spectrum is shown in Figure 7.1. In Figure 7.1, the spectrum at a resolution of 0.01 shows five peaks. At a lower resolution (less than 0.22) peak "b" has melded into peak "a", *i.e.* the system has not had sufficient enough time to resolve "b" from "a". By degrading the resolution (and therefore going to shorter time) one by one the peaks will coalesce together. Dynamically, it might be easier to think of this in the following manner. At a time, t = *very short*, there is only one peak in the spectrum, *i.e.* only one motion is resolvable. A peak in a *frequency* domain spectrum is a recurrence time, when at least part of the initial wavepacket has overlapped with the wavepacket propagated in time. In simple vibrational oscillator spectra the wavepacket returns to the initial coordinate position at a frequency of the oscillation by following in coordinate space the periodic orbit or motion of the oscillation. By sequentially allowing the system a longer time to evolve more peaks will appear when the system has had enough time to resolve separate motions.

This is shown pictorially in Figure 7.2. At t equivalent to a resolution of 1.8 the spectrum shows only two peaks. At t equivalent to a resolution of 0.7 the spectrum now has fractionated into three peaks. At t equivalent to a resolution of 0.25 the system now has evolved in time enough to start to resolve peak "d" from "e", and so on.

A "tree" displays this natural time evolution. A tree is made up of nodes which correspond to the resolution at which two peaks coalesce. The lowest node (longest time, highest resolution) in Figure 7.2b occurs at a resolution of 0.22, when peak "b" coalesces into peak "a". The next node is at a resolution of 0.335, when peak "e" coalesces into peak "d". At a resolution of 1.4, peak "c" joins with the "d+e" peak, and at 2.0 "a+b" joins with "c+(d+e)". The important information in a tree is the relative heights of the nodes and the overall branching pattern. The terms *node height* and *split width* are used interchangeably to describe the resolution at which two peaks become one.

In classification literature, if the heights of the nodes have a value associated with them, *i.e.* the tree is not just showing relational information, then technically the diagram is a called a dendrogram. In this chapter and in Mike Davis's work the more colloquial term tree is used instead.

A tree for the Origin Band DF spectrum, Figure 7.3a, is shown in Figure 7.3b. A tree for the $2\nu_3'$ DF spectrum [6], Figure 7.4a, is shown in Figure 7.4b.

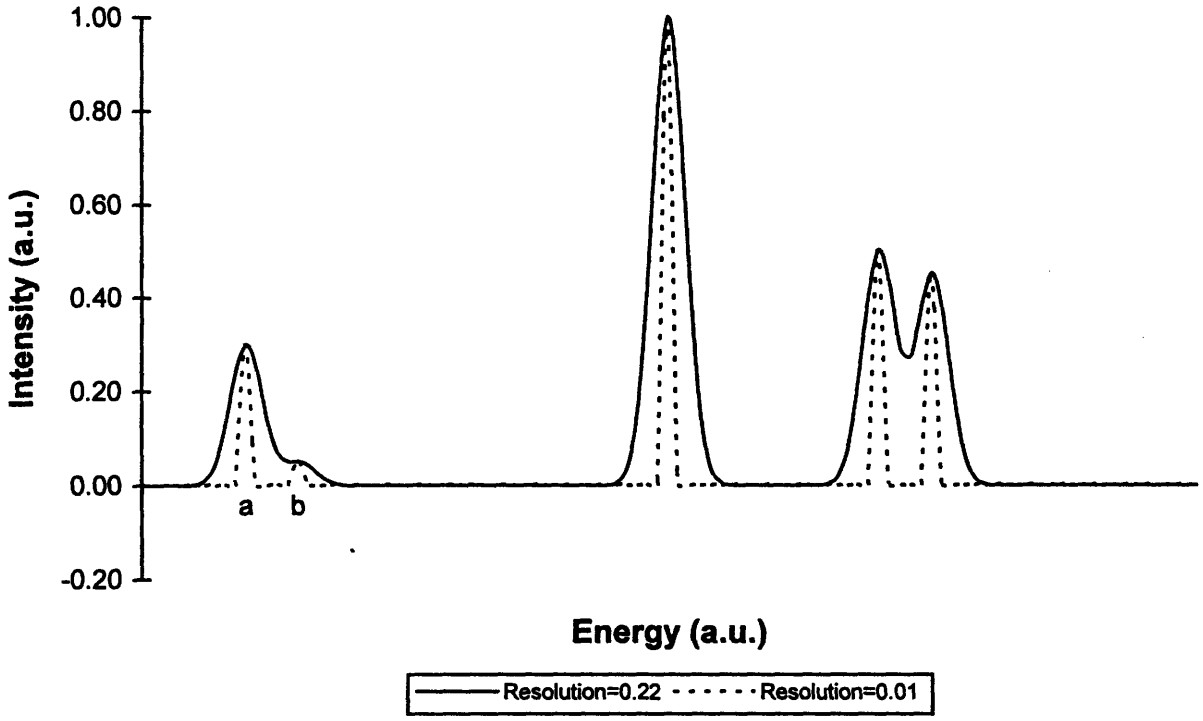

Figure 7.1: A fictitious spectrum showing five peaks at 0.01 resolution. At a resolution lower than 0.22, peak "b" will meld into peak "a".

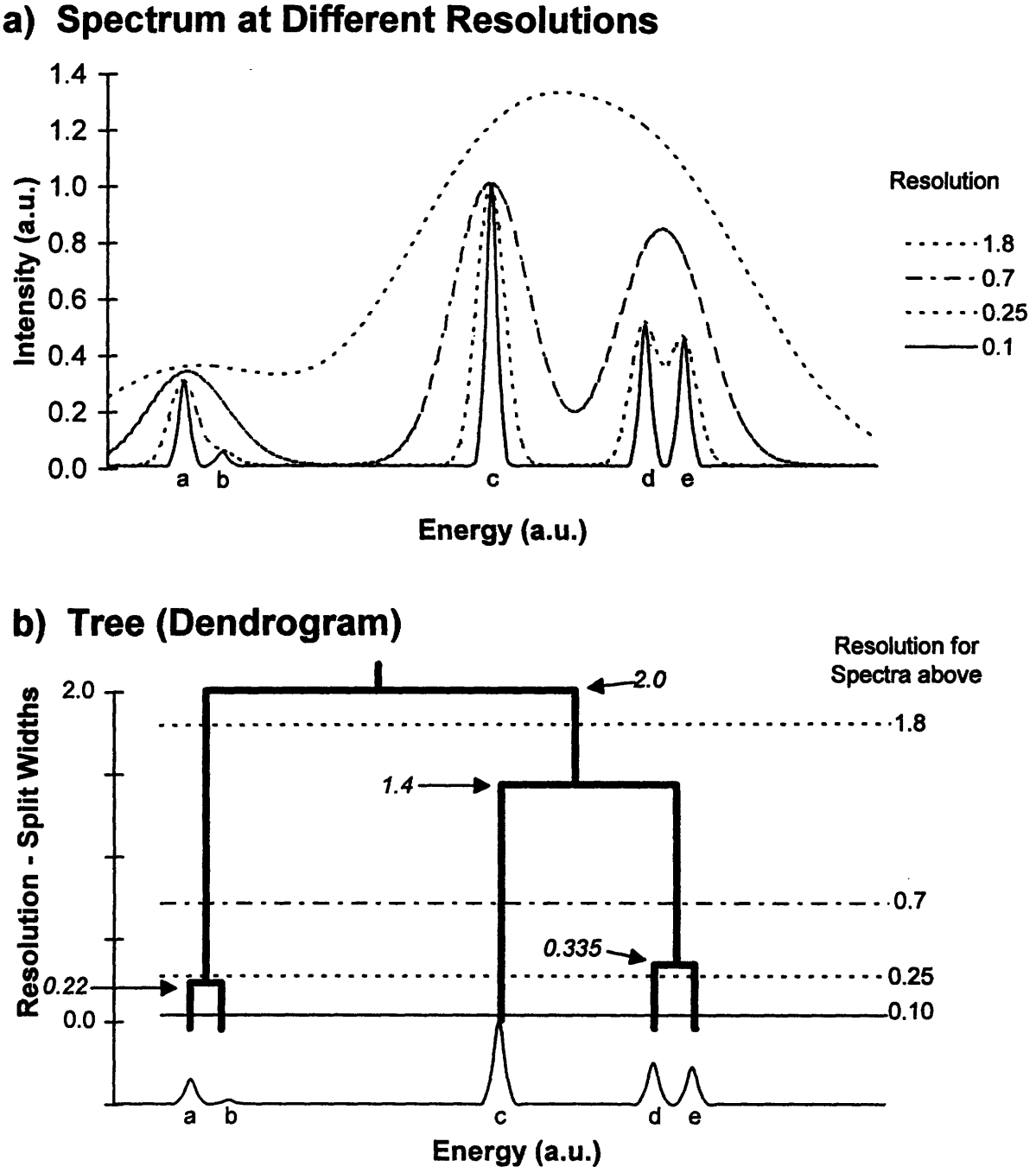

Figure 7.2: a) The same fictitious spectrum as Figure 7.1 but now shown at four different resolutions. b) The tree (dendrogram) generated from the spectrum in a). The split widths are highlighted with arrows. For reference the four different resolutions of the spectrum from a) are shown by vertical lines.

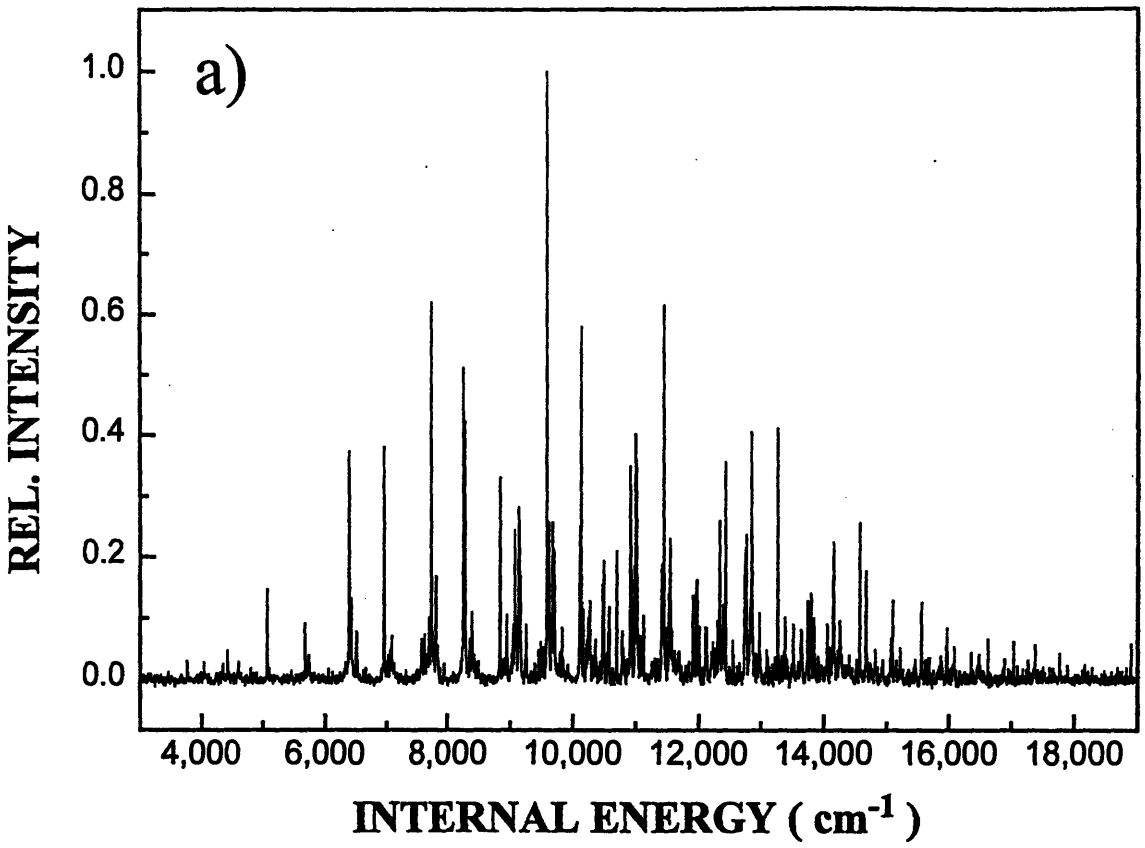

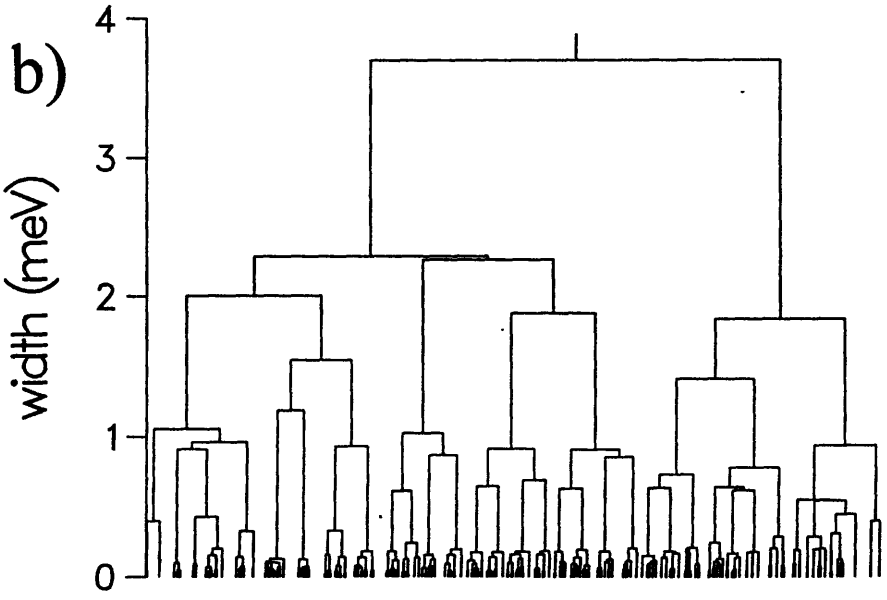

Figure 7.3: a) The Origin Band DF spectrum and b) its tree.

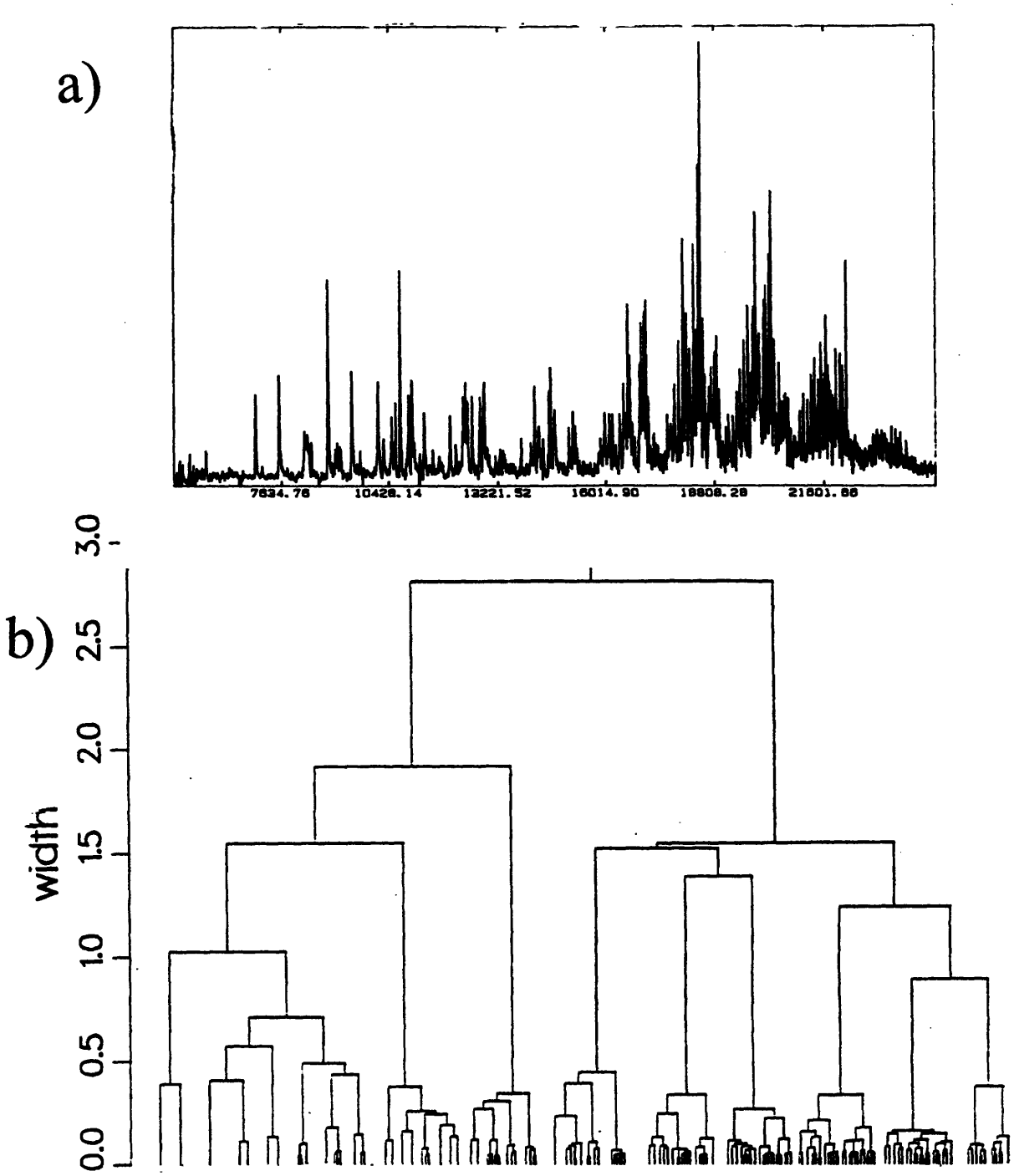

Figure 7.4: a) The $2\nu_3'$ DF spectrum [6] and b) its tree.

For some of the classification measures a *distance matrix* is generated which is a mathematical representation of the tree. If the rows and columns are labeled by the number of each peak, then each entry is the distance between the two peaks defined as the closest node that connects the two peaks. For example the distance between peak "a" and "b" is the 0.22 node height, while the distance between peak "a" and "c" is the top of the tree, the 2.0 node height. The distance matrix for the tree in Figure 7.2b is

$$\mathcal{D} = \begin{pmatrix} 0.0 & 0.22 & 2.0 & 2.0 & 2.0 \\ 0.22 & 0.0 & 2.0 & 2.0 & 2.0 \\ 2.0 & 2.0 & 0.0 & 1.4 & 1.4 \\ 2.0 & 2.0 & 1.4 & 0.0 & 0.335 \\ 2.0 & 2.0 & 1.4 & 0.335 & 0.0 \end{pmatrix}. \tag{7.1}$$

7.2.2 Hierarchical Measures

Three of the hierarchical analysis measures will be described briefly here.

7.2.3 Split Widths

Simply ordering the split widths from longest to shortest allows the observation of the commonalty of node heights. The tree and a plot of the ordered split widths for the Origin Band DF spectrum are shown in Figure 7.5. Large vertical drops denote separations in timescales and plateaus denote globality of timescales.

If the dynamics changes across a spectrum, then the separation in timescales will be averaged out since different parts of the spectrum might contain different timescales. One advantage of a tree is that the hierarchical measures can also be run on restricted parts of the tree. For example, the central part of the Origin Band tree (corresponding to 10,000-16,000 cm^{-1}) has a much stronger separation of timescales than the high energy end of the tree/spectrum (16,000-19,000 cm^{-1}), see Figure 7.6.

One problem with the split widths alone is that they do not contain any information about the branching of the tree. For example, in Figure 7.7 the top node only splits off one peak and may therefore not be as important as the other nodes, so measures that also take into account the branching pattern would be useful.

7.2.4 Geometrical Measures

Geometrical measures tell the importance of a node in determining the structure of the tree. Geometrical measures often describe the dimensionality of the tree.

The distance matrix, $\mathcal{D}$, described previously has some rather interesting mathematical properties. A metric space [7] is a set $\mathcal{M}$ of elements $x, y, \ldots$ such that with each pair of elements there is an associated real number $m(x, y)$ with the following properties:

- $m(x, y) \geq 0; m(x, y) = 0$ if and only if $x = y$
- $m(x, y) = m(y, x)$
- for any three element $x, y, z \in \mathcal{M}$, the triangle inequality holds: $\mathcal{M}(x, z) \leq \mathcal{M}(x, y) + \mathcal{M}(y, z)$.

Euclidean n-dimensional space, $\mathbb{R}^n$, is an example of a metric space with m defined as the Euclidean distance. The tree distance matrix, $\mathcal{D}$, is ultrametric — that is the elements of the matrix

$$\mathcal{D}(i, k) \leq \max[\mathcal{D}(i, j), \mathcal{D}(j, k)] \tag{7.2}$$

which is a stronger condition than the triangle inequality, and therefore, implies that a tree constructed from a spectrum containing n lines, has $n - 1$ nodes and occupies $n - 1$ dimensions. For such a set of points it is common to determine if the matrix, $\mathcal{D}$, fits in a dimension smaller than $n - 1$.

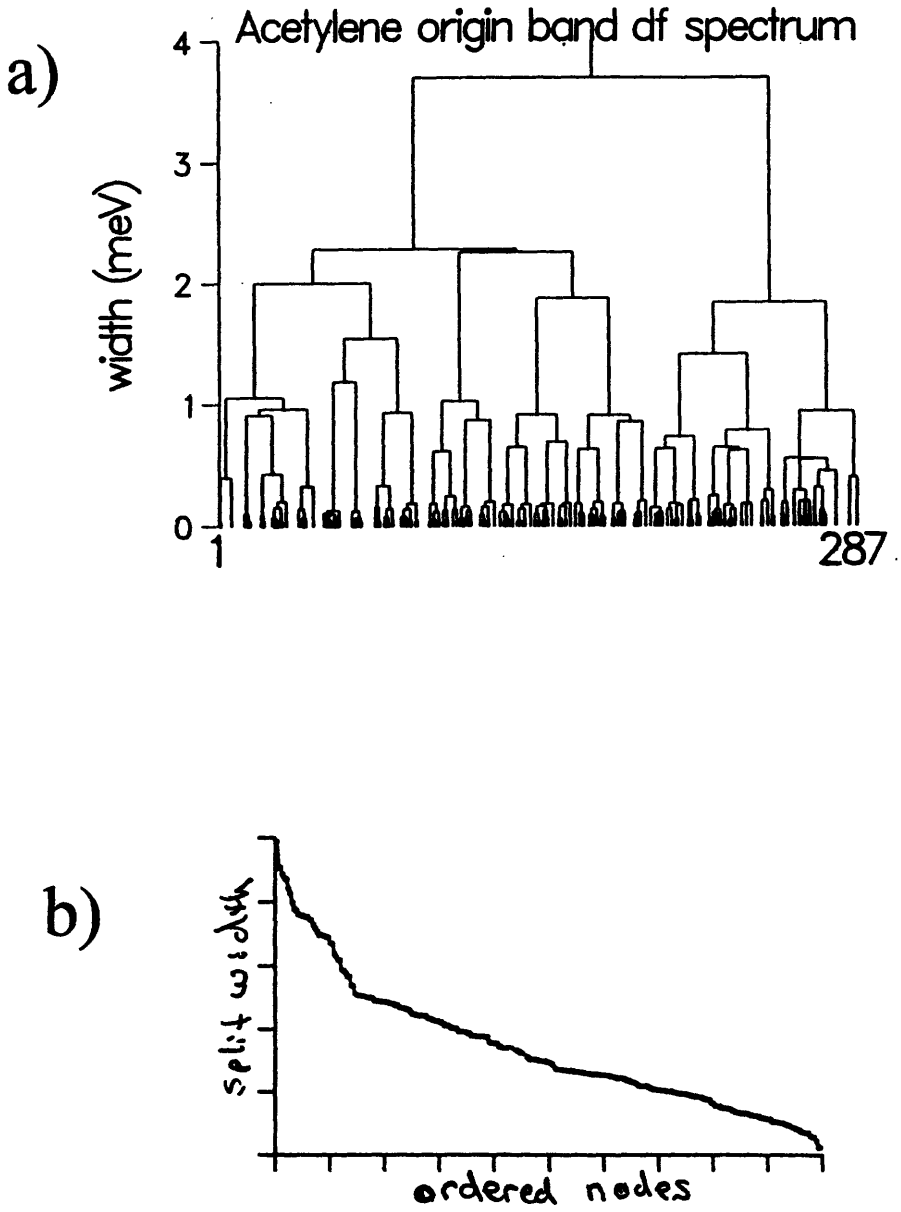

Figure 7.5: a) The Origin Band DF spectrum tree b) the ordered split widths.

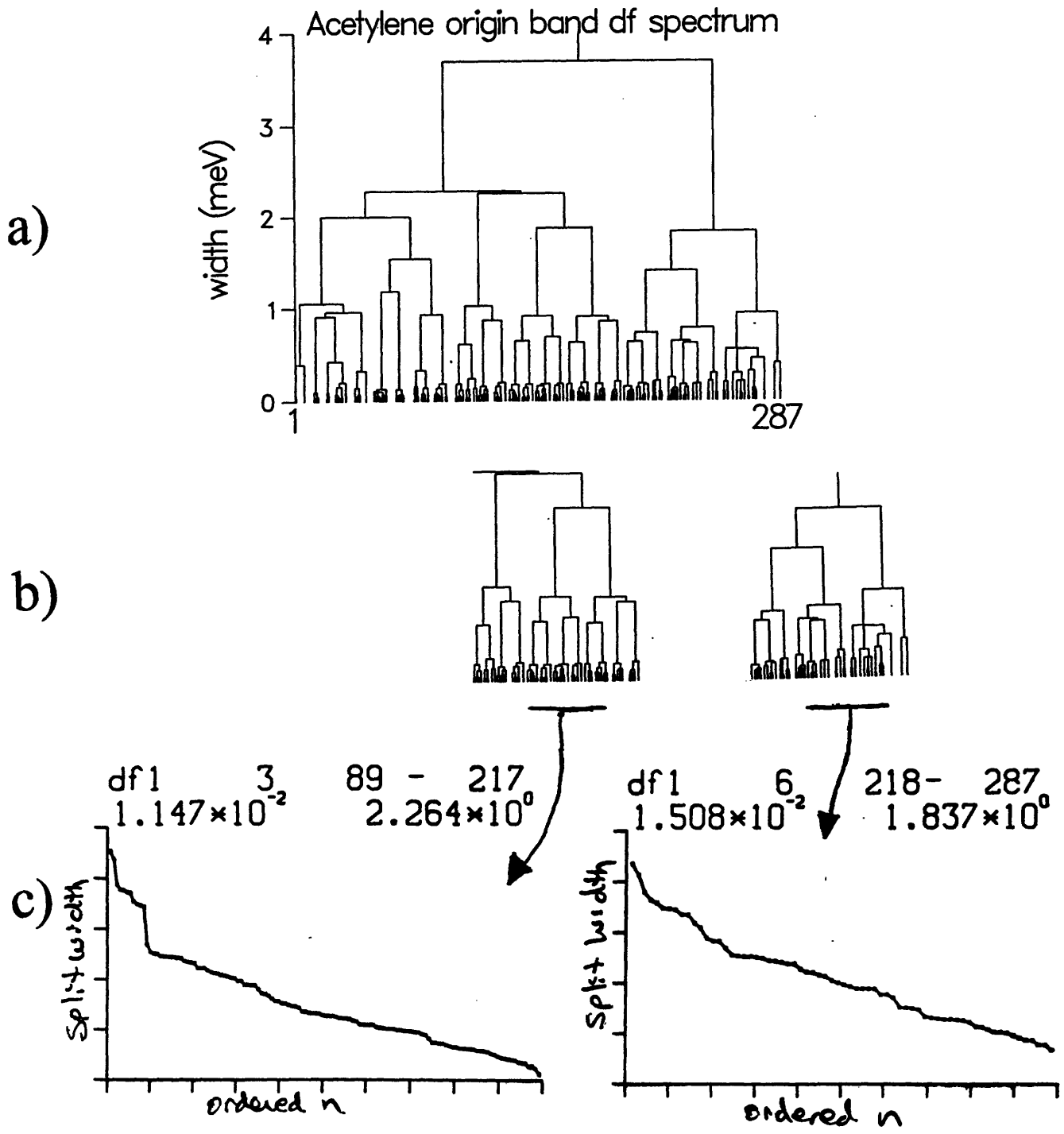

Figure 7.6: a) The Origin Band tree b) the two subtrees representing the 10,000-16,000 cm^{-1} and 16,000-19,000 cm^{-1} regions, respectively and c) their ordered split widths.

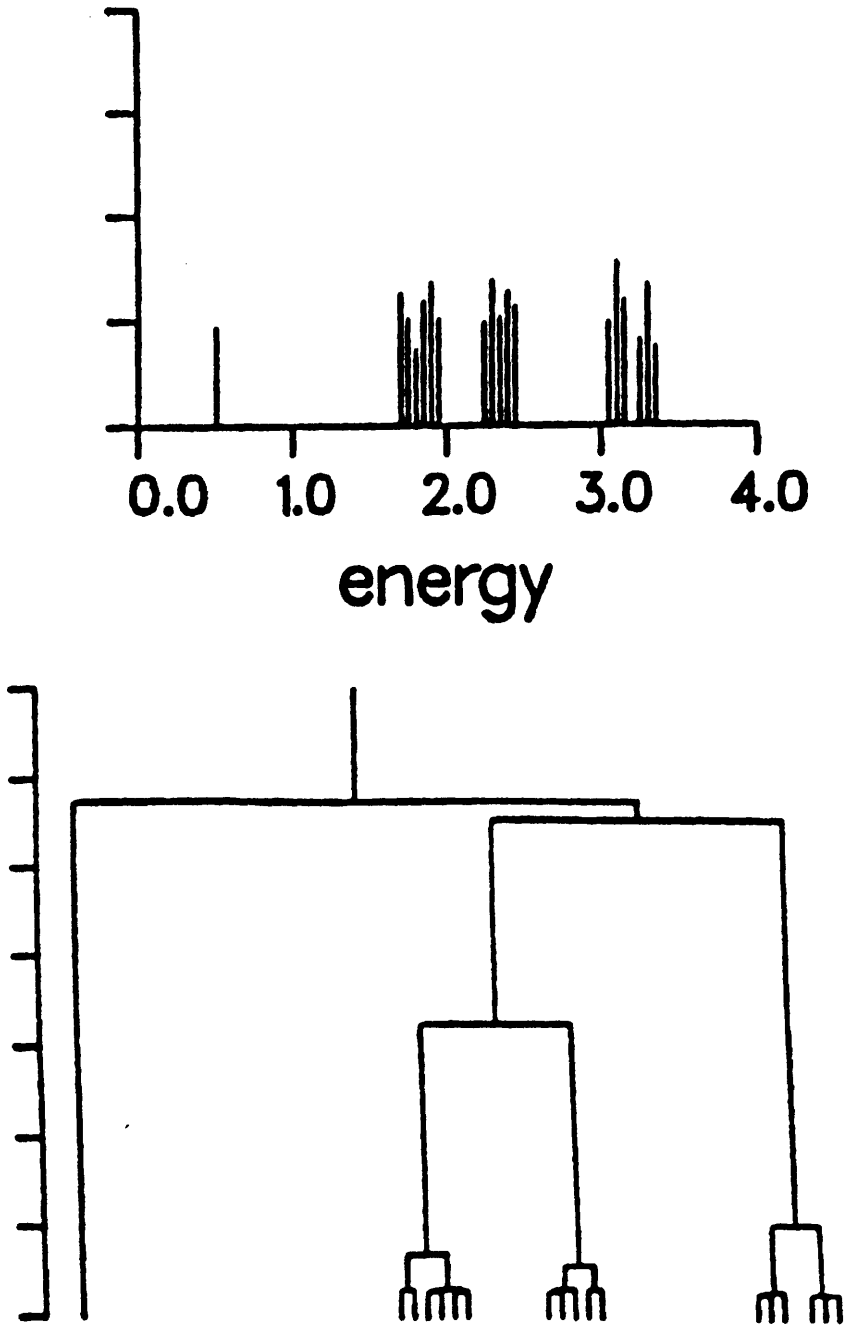

Figure 7.7: A fictitious spectrum and its tree.

This question of dimensionality is exactly equivalent to determining how well a two dimensional set of points fits to a one dimensional line. This question of dimensionality can be extended to any number of dimensions. In general, a transformation is determined which "best fits" the points to a topological entity in a lower dimensional space. Linear transformations are common in many fields and may be most familiar to the reader as Principal Coordinate Analysis (PCA), Singular Value Decomposition or Classical Scaling.

In practice, there is no reason why non-linear transformations could not also be used. Non-linear transformations would be equivalent to quantifying the fit of the two dimensional set of points to a curve as opposed to a straight line. Non-linear transformations are often called Multidimensional Scaling or Non-Linear Mapping.

The measure discussed here and in Davis's work [1] is due to Critchley and is a linear geometrical representation. Critchley's measure is computationally much more efficient than PCA, $\mathcal{O}(N)$ versus $\mathcal{O}(N^3)$, respectively. Critchley's measure also gives a variance for each node of the tree (not done directly in PCA). The variance tells the importance of the node to the structure of the tree, *e.g.* these four nodes gives 99% of the information contained in the tree.

As for the split widths, large drops and plateaus in the Critchley's measure tell about the difference and globality of timescales as well as how many timescales are needed to determine the information content of the tree. The values of the Critchley's measure for the Origin Band subtrees are shown in Figure 7.8. The 10,000-16,000 cm^{-1} region again shows more and sharper timescale separations than the 16,000-19,000 cm^{-1} region. The vertical lines in Figure 7.8c represent the percentage information content. The vertical lines represent 50, 75 and 90%, respectively, of the information content in the tree is represented by the nodes with a Critchley's measure above these respective lines. The vertical lines are lower, and therefore encompass more nodes, for the higher energy region. This is equivalent to saying that the structure of the tree is not as simple in the higher energy region; there are fewer "similar in magnitude" and "global in extent" timescales.

7.2.5 Cluster Analysis

Cluster analysis (sum of squares measure) tries to quantify groupings. "Groups" can be described with respect to their separation from each other and also their internal similarity. In other words, cluster analysis measures the "isolation between groups" versus the "scatter within a group". Cluster analysis is computationally expensive, so constraints are often used. The tree structure itself provides natural constraints.

The criterion used in Mike Davis's work [1] is the "sum of squares criterion" which generates his VRC measure. The reader is referred to that reference for further explanation of the VRC cluster measure. Favorable groupings are found after a large jump in the VRC measure followed by a slow rise. The VRC measure for the Origin Band subtrees are shown in Figure 7.9. The 10,000-16,000 cm^{-1} region again shows more favorable groupings than the 16,000-19,000 cm^{-1} region whose groups are not as well defined.

7.2.6 Analysis of the DF Spectrum

Further analysis using hierarchical methods on the DF spectrum and on the effective Hamiltonian described previously will be presented in forthcoming papers.

7.2.7 Effect of the DD Stretch in the IVR of the DF Spectrum

In an attempt to study the timescales inherent in the effective Hamiltonian and to be able to locate their signatures in the DF spectrum, hierarchical analysis was performed on simulated DF spectra prepared from the effective Hamiltonian with various couplings turned on and off or altered in value. It was found that if the Darling-Dennison (DD) Stretch coupling strength was decreased by an order of magnitude relative to its nominal value, then the resulting DF spectrum exhibited 25% less fractionation, measured as the number of peaks within 1/1000th of the intensity of the strongest peak. This is surprising and important for two reasons. First, only roughly two thirds of the polyads in the DF spectrum have sufficient quanta in the stretches for the DD stretch to be active in their polyad, and, second, this DD stretch resonance is at least two coupling tiers away from the bright state in these experiments.

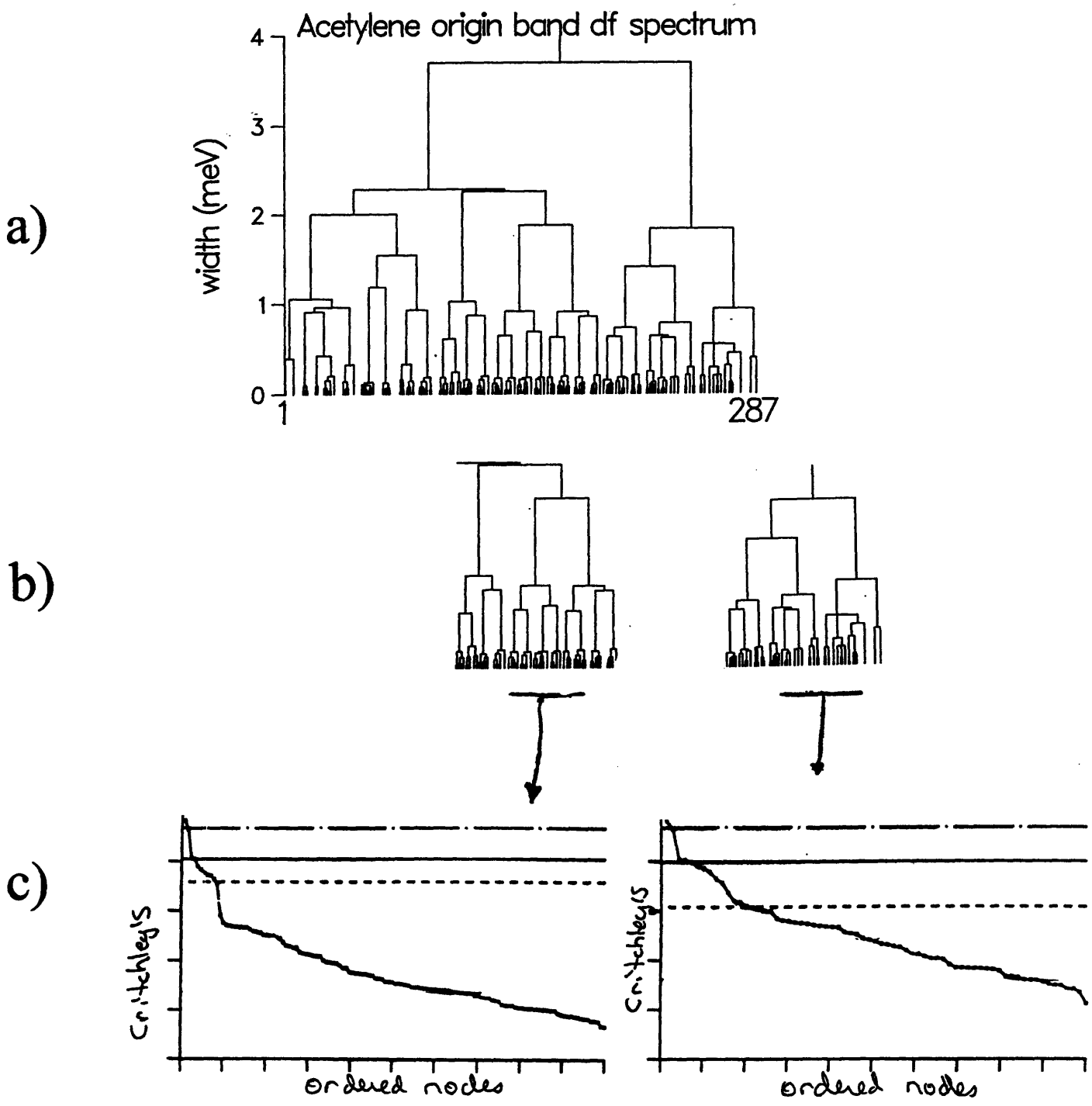

Figure 7.8: a) The Origin Band tree b) the two subtrees representing the 10,000-16,000 cm^{-1} region and the 16,000-19,000 cm^{-1} region, respectively and c) their Critchley's measure. The vertical lines represent 50, 75 and 90%, respectively, of the information content in the tree is represented by the nodes with a Critchley's measure above these lines.

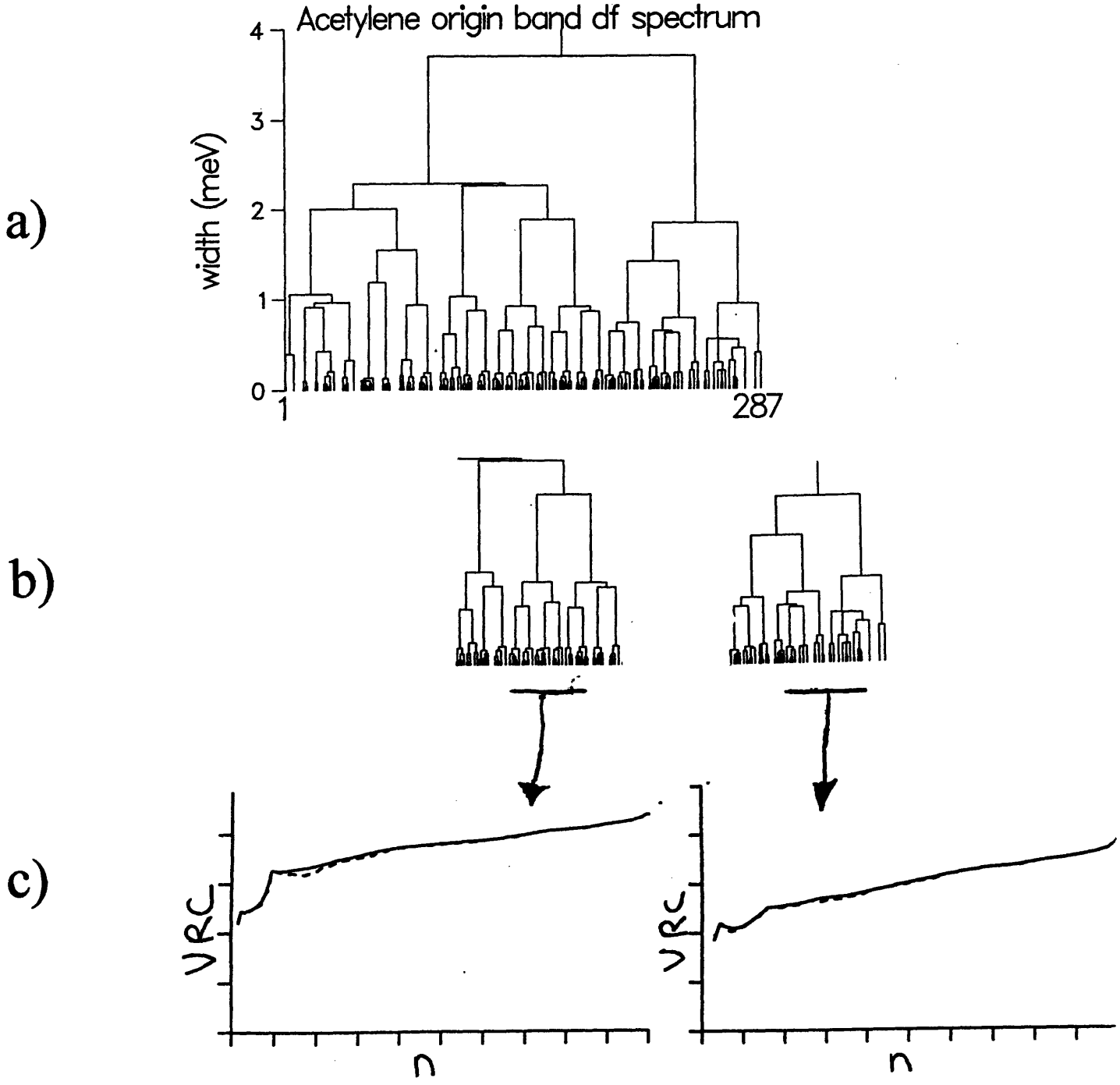

Figure 7.9: a) The Origin Band tree b) the two subtrees representing the 10,000-16,000 cm^{-1} region and the 16,000-19,000 cm^{-1} region, respectively and c) their VRC measure.

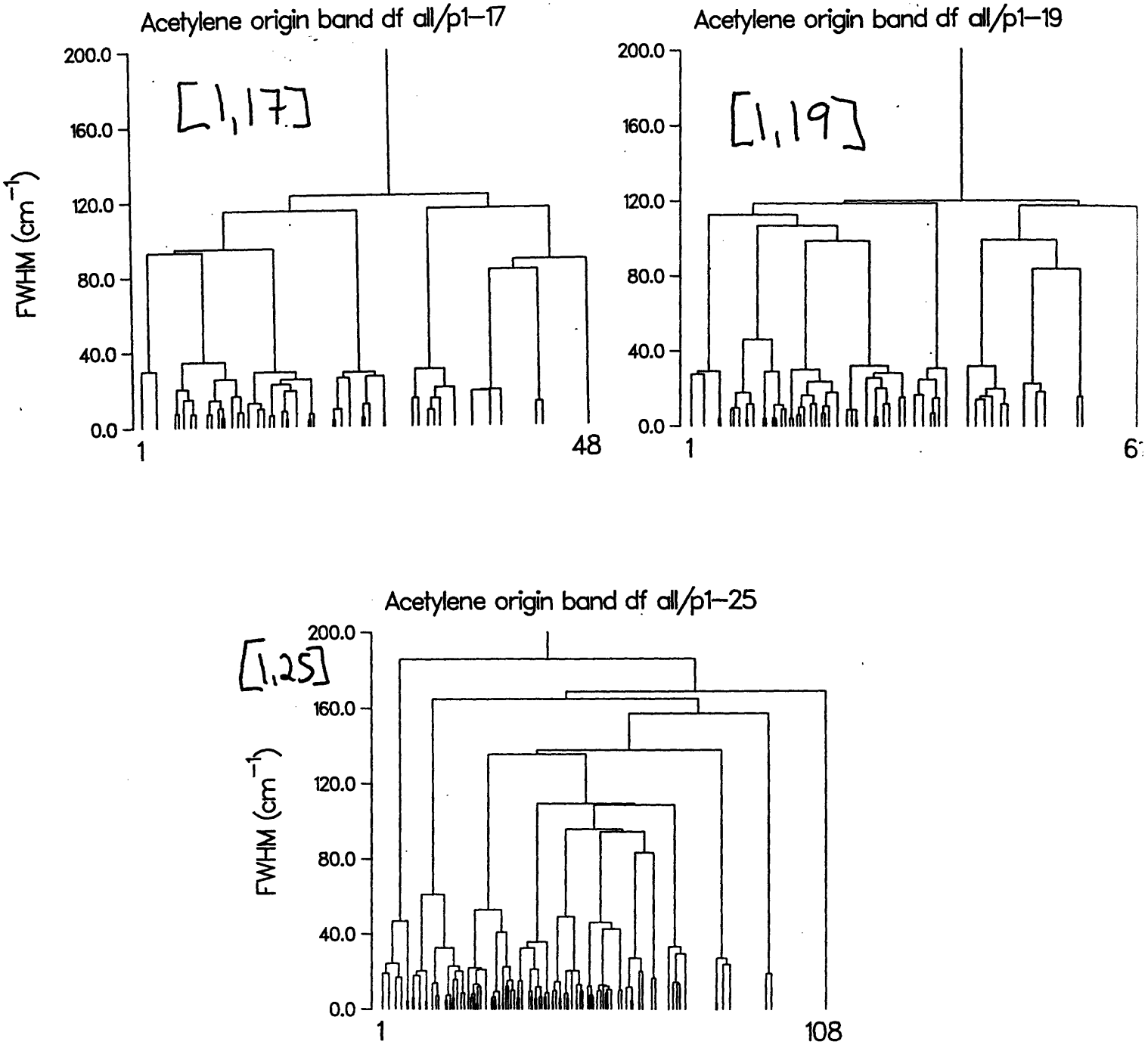

Figure 7.10: The trees for the [1, 17], [1, 19] and [1, 25] polyads.

It would be intriguing to find out *how* this far off resonance coupling affects the simulated DF spectra and if the corresponding time signatures are also present in the real experimental DF spectrum. Preliminary analysis on the [1, 17], [1, 19] and [1, 25] polyads show a distinct grouping of timescales which corresponds to a resolution roughly of 80-120 cm^{-1} in the [1, 17] and [1, 19] polyads, see Figure 7.10, but that this timescale is washed out in the [1, 25] polyad. Preliminary analysis suggest that the distinct timescales are a result of sequential energy flow up within a single DD Bend Stack (See Chapters 5 and 6), while in the [1, 25] polyad, the energy flow pathway seems to include branching out to other stacks. The analysis is still being conducted and will be presented in forthcoming papers.

References

[1] M. J. Davis. *J.Chem.Phys.* **98**(4), 2614 (1993).

[2] T. A. Brody, J. Flores, J. French, P. Mello, A. Pandey, S. S. M. Wong. *Rev.Mod.Phys.* **53**(3), 385 (1981).

[3] B. Eckhardt. *Phys.Rep.* **163**(4), 206 (1988).

[4] M. V. Berry, M. Tabor. *Proc.Roy.Soc.A* **356**, 375 (1977).

[5] "*Fractionation*, or *fragmentation*, is defined to mean the complicated spectrum resulting from IVR. As opposed to *congestion*, a spectrum that looks complicated but NOT resulting from IVR." - Jon Hougen - Talk MH01, The Ohio State University International Symposium on Molecular Spectroscopy, June 14, 1993.

[6] K. Yamanouchi, N. Ikeda, S. Tsuchiya, D. M. Jonas, J. K. Lundberg, G. W. Adamson, R. W. Field. *J.Chem.Phys.* **95**(9), 6330 (1991).

[7] I. N. Bronshtein, K. A. Semendyayev. *Handbook of Mathematics.* Van Nostrand Reinhold Company, Inc., New York, NY (1971).